Universidade de São Paulo
Instituto de Física

Efeitos cinemáticos e a quebra de isotropia estatística das flutuações da radiação cósmica de fundo

Esteban Ricardo Chalbaud Mogollón

Orientador(a): Prof. Dr. Edivaldo Moura Santos

Dissertação de mestrado apresentada ao Instituto de Física da Universidade de São Paulo, como requisito parcial para a obtenção do título de Mestre em Ciências.

Banca Examinadora:
Prof. Dr. Edivaldo Moura Santos - Orientador (IF-USP)
Prof. Dr. Miguel Boavista Quartin - (UFRJ)
Profa. Dra. Mariana Penna Lima Vitenti - (UnB)

São Paulo
2021

FICHA CATALOGRÁFICA
Preparada pelo Serviço de Biblioteca e Informação
do Instituto de Física da Universidade de São Paulo

Chalbaud Mogollón, Esteban Ricardo

Efeitos cinemáticos e a quebra de isotropia estatística das flutuações da radiação cósmica de fundo. São Paulo, 2021.

Dissertação (Mestrado) – Universidade de São Paulo, Instituto de Física, Depto. de Física Experimental

Orientador: Prof. Dr. Edivaldo Moura Santos

Área de Concentração: Física

Unitermos: 1. Radiação cósmica de fundo; 2. Observações cosmológicas; 3. Parâmetros cosmológicos.

USP/IF/SBI-032/2021

University of São Paulo
Physics Institute

Kinematic effects and the break of statistical isotropy of the cosmic microwave background fluctuations

Esteban Ricardo Chalbaud Mogollón

Supervisor: Prof. Dr. Edivaldo Moura Santos

Dissertation submitted to the Physics Institute of the University of São Paulo in partial fulfillment of the requirements for the Master degree of Science.

Examining Committee:
Prof. Dr. Edivaldo Moura Santos - Supervisor (USP)
Prof. Dr. Miguel Boavista Quartin - (UFRJ)
Prof. Dr. Mariana Penna Lima Vitenti - (UnB)

São Paulo
2021

"Eppur si muove"

To my mother Leticia

Acknowledgments

I want to express my gratitude to Professor Edivaldo Moura Santos and Dra. Camila Novaes. Their continuous support during this work was vital, especially for his patience, motivation, enthusiasm, and immense knowledge. I am immensely grateful to Professor Edivaldo for teaching me all the needed skills for this project, allowing me to access all the necessary tools for this work, and train my computer skills. I am incredibly thankful for all the learned skills and his exceptional patience, especially while learning to use C/C++ and during the writing process of this dissertation.

Moreover, I would like to express my immense gratitude to Dra. Camila Novaes, whom I consider the co-supervisor of this work. Her support and motivation were essential for completing this work especially during the beginning of the COVID-19 pandemic. I am incredibly thankful to her for introducing me to the Python programming language, allowing me to improve the quality of shown plots.

Additionally, It is essential to acknowledge all the Professors at the IF-USP institute for their passion in lectures. I want to thank Prof Raul Abramo, Prof Renata Zukanovich, Prof Toledo Piza, Prof Zwinglio, Prof Marcos Lima, and Prof Gabriel Landi for the courses and all the taught material. On the other hand, it was a pleasure to share these years at USP with Prof Ivone, Nikolas, Argel, Keiser, Miguel and Johnnier during the development of this work at the *Laboratório do Acelerador Linear*. It is also for me a great pleasure to have participated in discussions with Caroline, Natali, Martín and Professor Raul Abramo during their weekly *Cosmo Meetings* at the *Departamento de Física-Matemática* over the past months.

Finally, I would like to express my gratitude to my friends in Brazil and in the US for their companion: Ana Paula, Ailton, Gabriela, Ed, Jorge and my family in Venezuela, Leticia, Eduardo, and Angerdrin for their invaluable companion and patience during the development of this work. It is also impossible to forget the support from Prof Alejandra Melfo, Prof Nelson Pantoja, both my former professors in Venezuela during my Bachelor's degree at ULA, for their support before and after traveling to Brazil. Additionally, I would like to express my gratitude to the ICTP staff especially to Prof Goran Senjanović, and Prof Paolo Creminelli, for all their support while traveling to Brazil.

This work was possible by the funding support from Conselho Nacional de Desenvolvimento Científico e Tecnológico (CNPq) through the grant: (Edital MCT/CNPq: 166493/2018-0). Additionally, I would like to express my gratitude for the computational resources provided by the *Superintendência de Tecnologia da Informação* at the *Universidade de São Paulo* (USP).

Abstract

In this work, we study the impact of a non-comoving observer measuring the anisotropies of the Cosmic Microwave Background (CMB). We recover the cross-correlation signal appearing in neighboring multipoles, as a consequence of the statistical isotropy violation, caused by the observer's movement. It is also presented the impact of this effect over the temperature and polarization power spectra. We tested the impact of the statistical isotropy violation on cosmological parameters using three different likelihood estimators, which combine temperature and polarization measurements. These estimators were used to restrict a sub-set of cosmological parameters of the ΛCDM model (more precisely, $\Omega_b h^2, \Omega_c h^2, 100\Theta_{MC}, \tau, \ln(10^{10}A_s), n_s$) obtaining constraints on the parameters using CMB anisotropy measurements compatible with a *Planck*-like satellite. No significant systematic effects were found in this subset of ΛCDM parameters induced by the kinematic effects of an observer with peculiar velocity $\boldsymbol{\beta} = 1.23 \times 10^{-3}$, at least using full-sky CMB maps, in both temperature and polarization. Finally, we built a maximum likelihood estimator based on the combined effects of Doppler modulation and relativistic aberration. This estimator was applied to determine the peculiar velocity $\boldsymbol{\beta}$ using full-sky CMB synthetic maps as input data, as well as Bayesian analysis techniques using Markov chains for reconstructing the posterior probability distributions. During the consistency tests performed, we did not detect any significant bias in the estimator. On the other hand, its precision on the magnitude of peculiar velocity was estimated to be 84 km s $^{-1}$ and an angular resolution of $11.5°$, comparable, therefore, to those obtained, via the quadratic estimator, by the *Planck* collaboration of 78 km s^{-1} and $14°$, respectively.

Keywords: Cosmic Microwave Background; cosmological observations; cosmological parameters.

Resumo

Neste trabalho, estudamos o impacto de um observador não-comóvel nas anisotropias da Radiação Cósmica de Fundo (RCF). Recuperamos o sinal de correlação cruzada aparecendo em multipolos vizinhos como consequência da violação da isotropia estatística originada pelo movimento do observador. É apresentado o impacto desse efeito, ao nível do espectro de potência das anisotropias tanto para a temperatura como a polarização. Testamos o impacto da violação de isotropia estatística em parâmetros cosmológicos, usando três estimadores diferentes, que combinam tanto medidas de temperatura como de polarização. Estes estimadores foram usados para restringir um conjunto de parâmetros cosmológicos do modelo ΛCDM (mais precisamente, $\Omega_b h^2$, $\Omega_c h^2$, $100\Theta_{MC}$,τ, $\ln(10^{10}A_s)$, n_s) obtendo vínculos nestes parâmetros quando são usadas medições das anisotropias na RCF compatíveis com um satélite do tipo *Planck*. Não foram encontrados efeitos sistemáticos significativos nos parâmetros cosmológicos do modelo ΛCDM, induzidos pelos efeitos cinemáticos de um observador com velocidade peculiar $\boldsymbol{\beta} = 1.23 \times 10^{-3}$, pelo menos usando mapas sintéticos ao ceú inteiro, tanto de temperatura como de polarização. Finalmente, construímos um estimador de máxima verosimilhança baseado nos efeitos combinados de modulação Doppler e aberração relativística. Tal estimador foi aplicado na determinação da velocidade peculiar $\boldsymbol{\beta}$ usando mapas sintéticos como dados de entrada, bem como técnicas de análise Bayesiana utilizando cadeias de Markov para a reconstrução das distribuições de probabilidade a posteriori. Nos testes de consistência realizados, não detectamos a presença de um viés significativo no estimador. Por outro lado, sua precisão foi estimada em 84 km s^{-1} na magnitude da velocidade peculiar e uma resolução angular de $11.5°$, comparáveis, portanto, àquelas obtidas via estimador quadrático pela colaboração *Planck*, de 78 km s^{-1} e $14°$, respectivamente.

Palavras-chave: Radiação cósmica de fundo, observações cosmológicas, parâmetros cosmológicos.

Contents

List of Figures

List of Tables

1 | Introduction

Since the work of Arno Penzias and Robert Woodrow Wilson in 1964 [1], the Cosmic Microwave Background (CMB) has provided invaluable data for testing the foundations of cosmology. According to the standard cosmological model (known as ΛCDM), the CMB is the radiation released after the decoupling of photons from electrons and protons in late radiation dominance era [2–4]. Assuming General Relativity as the correct theory of gravitation at cosmological scales, in combination with the standard model of particle physics, it is possible to consistently derive a radiation field of photons propagating to lower redshift or late times. This radiation field, as the *COBE* satellite showed with astonishingly accuracy, has a black body spectrum with a temperature of 2.7260 ± 0.0013 K [5]. This measurement is currently considered one of the strongest evidence supporting the Big Bang theory of the origin of the universe.

According to the ΛCDM model, the CMB is expected to contain fluctuations with respect to the smooth black body temperature measured by *COBE* [2, 6]. The existence of these anisotropies gives strong support to the ΛCDM model, the perturbations are extremely useful in constraining the parameters of the model in combination with other data sets [7]. Indeed, these fluctuations in black body temperature were confirmed by the *COBE* satellite in addition to its temperature, being denoted as the monopole of the CMB [8]. The first dipolar moment of the anisotropies is known as the kinematic dipole of the CMB, that by assuming only kinematic motion of the observer, a boost velocity is obtained from this dipole. *COBE* estimated this peculiar velocity of the observer with respect to the CMB, obtaining a value of: 369.0 ± 2.5 km s^{-1} towards the direction $(\ell_{gal}, b_{gal}) = (264^\circ.31 \pm 0^\circ.04_{\text{stat}} \pm 0^\circ.16_{\text{sist}}, +48^\circ.05 \pm 0^\circ.02_{\text{stat}} \pm 0^\circ.09_{\text{sist}})$. [9].

The fluctuations in the radiation temperature were confirmed later in the 2000s by the *WMAP* satellite. With improved resolution, *WMAP* probed angular scales as small as 0.3°, much better than the 7° reached by *COBE*. In addition to the dipole, several other predicted effects expected from the ΛCDM model were confirmed by the probe due to the improved resolution of the satellite. Among the most important effects, one can mention the Sachs-Wolfe effect, due to the evolution of the gravitational potentials along the photon's path all the way from the last scattering surface to us, and the detection of the acoustic peaks in the anisotropies spectrum, explained from the dynamics of photons, electrons, protons and dark matter before the recombination (i.e. baryon acoustic oscillations). In addition to accessing smaller scales in the anisotropies, this satellite was able to confirm that CMB photons were polarized, adding further valuable data supporting the ΛCDM model. Recently, the resolution of the CMB probes improved by the launch of *Planck* satellite, a probe that was able to produce the clearest maps of the CMB anisotropies with the angular resolution of $5'$ [10] accessing the smallest CMB scales to date. Figure (1.1) shows this improvement in the detection of the CMB anisotropies from *COBE* to the *WMAP* to the *Planck* satellite.

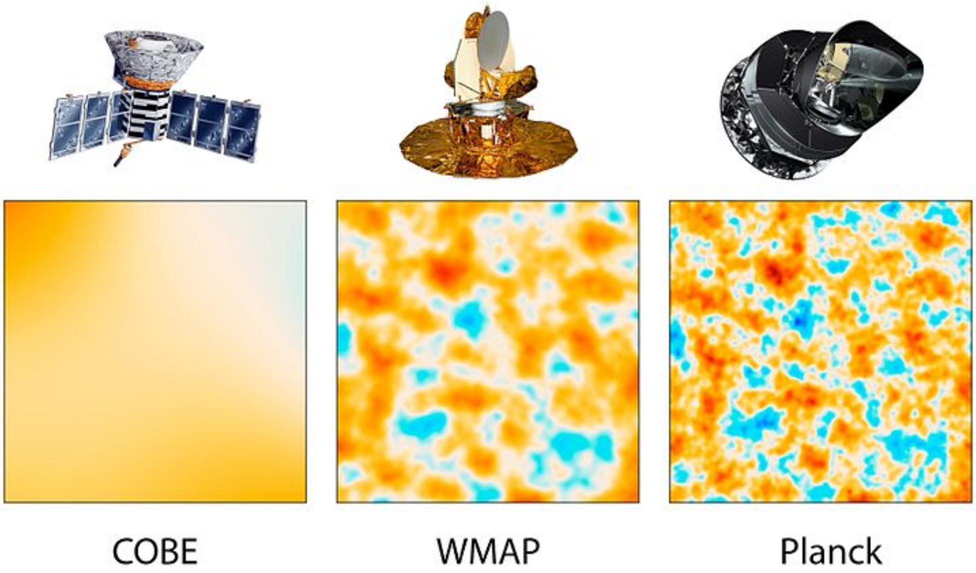

Figure 1.1: Improvement in angular resolution for observing the CMB anisotropies by *COBE*, *WMAP* and *Planck* satellites observing a 10° degrees square of the CMB anisotropies(Extracted from: NASA/JPL-Caltech/ESA).

The improvements in resolution allowed the *Planck* collaboration to measure the solar system peculiar velocity by using a bigger multipolar region than from *COBE* measurement, due to the availability of high resolution maps. By using temperature maps the collaboration reported a value of $(384\ \mathrm{km\ s^{-1}}\ \pm\ 78\ \mathrm{km\ s^{-1}}\ (\mathrm{stat.})\ \pm\ 115\ \mathrm{km\ s^{-1}}\ (\mathrm{syst.}))$ towards direction $(l, b) = (264^{\circ}, 48^{\circ})$. This is currently the best measurement using small scale effects (i.e. relativistic aberration to be discussed in chapter 3) [11].

By using high resolution maps, the data showed a few sources of statistical isotropy breaking in the sky, the most significant being the one interpreted as the peculiar motion of the observer with respect to the CMB [12]. It was argued in [13] and in [11], that this velocity can be measured by using the resulting cross-correlation between nearby multipoles $(\ell, \ell + 1)$ of the CMB temperature in harmonic space. In addition to that, it was shown in [14] that boost effects can actually modify the power spectrum of the anisotropies in the absence of a mask, introducing second order effects in peculiar velocity (i.e. $\mathcal{O}(\boldsymbol{\beta}^2)$). As a consequence, the resultant bias in this spectrum, widely used for testing ΛCDM, could in principle impact further analysis in other cosmological observables.

In this work, we focus on the understanding and disentanglement of kinematic (i.e. due to the observer's relative motion) and primordial CMB anisotropies using Monte Carlo simulations. Our goal is to understand the possible impact of kinematic effects on cosmological parameter estimations and to develop an unbiased method to determine the solar system velocity in the CMB rest frame based on their imprints (aberration and modulation) in the CMB temperature.

This thesis is organized as follows:

In chapter 2, we show a few properties of the ΛCDM model like its energy density content, geometry and thermal history. Later, we present the Boltzmann equation governing the evolution of photons, and the underlying equations from which CMB temperature anisotropies are derived. In this chapter polarization anisotropies are also reviewed, concentrating in the correlation functions and their parity restrictions. At the end of this chapter the dependence on cosmological parameters of the CMB power spectra is presented to the reader showing how sensitive is the temperature power spectrum under changes in a set of cosmological parameters.

In chapter 3, we define the frames relevant for boosting the anisotropies, quantifying the impact on the primordial fluctuations by having pixelized CMB maps boosted with a given velocity $\boldsymbol{\beta}$. The signatures of both Doppler modulation and aberration effects were explored in this chapter by computing the theoretical cross-correlation function $\langle a_{\ell m} a^*_{\ell+1 m}\rangle$ and comparing the results with the corresponding correlation from synthetic CMB maps containing boost effects. At the end of this chapter we show the impact of a moving observer in temperature and polarization CMB anisotropies power spectra (i.e. $C_\ell^{TT}, C_\ell^{TE}, C_\ell^{EE}$) showing the sensitivity of these quantities under an applied boost.

In chapter 4, by using MCMC methods, we make a set of tests showing that the systematic shifts induced onto cosmological parameters extracted via the usual CMB power spectra (C_ℓ^{TT}, C_ℓ^{EE} and C_ℓ^{TE}) when kinematic effects are present are subdominant with respect to the statistical uncertainties for a *Planck*-like satellite resolution and boost velocities $\beta \sim 10^{-3}$.

In chapter 5 we present an extension of the method described in [15], which was originally developed for detecting signals of statistical isotropy breaking of dipolar type through modulaton-like terms in the CMB covariance matrix. Our extension allowed for the estimator to incorporate also relativistic aberration effects which, in turn, were used to determine the velocity of the solar system. Both the accuracy and the precision of the estimator were carefully studied, showing that it is unbiased and that its precision is comparable to the current quadratic estimator employed by *Planck* in its aberration dominated measurement of the solar system barycenter velocity.

Finally, in chapter 6 a summary of the results is shown in addition to future perspective for extensions of the current work.

2 | Foundations

According to our current knowledge of the evolution of the universe, the cosmos is filled with a radiation field, known as the CMB, whose maximum spectral intensity is nowadays in the microwave region. The perturbative form of Einstein's equations of General Relativity applied to our universe predicts that this radiation field should present anisotropies, whose statistical properties are uniform across the sky, that is, we say that it is statistically isotropic. In the following, we focus on introducing the reader to the main features of the standard cosmological model relevant in the context of the CMB. We revisit in a nutshell the ΛCDM model and its thermal history as starting point for obtaining the properties of the CMB, we show Boltzmann equations used to derive the anisotropies detected, both in the intensity and in the polarization, along the last three decades by the *COBE*, *WMAP* and *Planck* satellites, and the dependence of the power spectrum of these anisotropies with a minimum set of parameters of the ΛCDM model.

2.1 The ΛCDM model

By analogy with the standard model of particle physics, cosmology has its own standard model, known as ΛCDM or concordance model. It is currently the best description of the Universe compatible with most of the observational data. In the following, we present the most relevant features of the model, that consistently lead into a decoupling of photons from electrons and protons at redshift $z \sim 1100$, detected as black body radiation by *COBE*, *WMAP* and *Planck* satellites.

2.1.1 Energy content

The ΛCDM model specifies a few physical sources of the energy density budget of the cosmos. In the model, fluids are distinguished by their equation of state (given by the pressure to energy density ratio), in the form of pressure-less matter, radiation, and a pure cosmological constant. The equations of state w associated to each of these components and the way their energy density ρ evolve with the scale factor of the universe a is shown in table (2.1). Since in Einstein's equations of General Relativity, spatial curvature plays a role in the evolution of the universe [16], it is possible to associate an effective equation of state to this component which is also shown in table (2.1).

Component	$\rho(a)$	ω
Matter	$\rho_0 a^{-3}$	0
Radiation	$\rho_0 a^{-4}$	$\frac{1}{3}$
Dark energy	ρ_0	-1
Curvature	$\rho_0 a^{-2}$	$-\frac{1}{3}$

Table 2.1: Energy density $\rho(a)$, and the equation of state for the fluid components as well as for the effective energy density associated to curvature, ρ_0 denotes the energy density today. (Adapted from [16]).

Additionally, the model distinguishes between the normal baryonic matter (leptons and barions described by the Standard Model of particles) and the non-interacting cold dark matter, both having the same energy density evolution with the scale factor. The relative percentage between baryonic and dark matter have a relation of 1 to 5, approximately [17, 18]. The true nature of dark matter present in the ΛCDM model, however, is yet to be understood. The energy budget contemplated in the model can be summarized as follows:

1) Baryonic matter: it represents around 5% of the total energy density in the model, containing all the baryons and leptons of the standard model of particle physics.

2) Dark Matter: it represents roughly 25% of the total energy density, the true nature of these particles is still unknown due mainly to the lack of statistically significant signals by direct detection experiments. However, indirect evidence nowadays comes from: rotational curves of galaxies [19], the level of fluctuations observed in the 3D matter power spectrum [20], the offset identified between the amount of mass estimated through X-ray and optical observation and that reconstructed via gravitational lensing in the bullet cluster [21], the mass-luminosity ratio in clusters [22], the fact that dark matter is an important ingredient of the model to correctly describe the CMB anisotropies [23, 24] .

3) Dark Energy: this ΛCDM energy density is not well-understood yet, it represents nearly 70% of the total energy budget in the Universe. According to the model, this form of energy density is constant in time. It is believed that it drives the current accelerated phase of the Universe as inferred from type Ia supernovae (SNIa) luminosity distance measurements. SNIa is a special type of star explosion whose intrinsic luminosity is well understood, so that apparent magnitude measurements can be used to infer the supernova distance [25].

4) Radiation: in the concordance model, relativistic species (matter and radiation) contribute with less than 1% in the total energy density today. It gathers all relativistic degrees of freedom. Today one of the known contributions comes from photons, with

a number density of roughly 411 photons cm^{-3}.

5) Neutrinos: Neutrinos are also taken into account inside the ΛCDM model as relativistic species, except at low redshift z, their total mass and the number of effective species are observable quantities constrained from data [26].

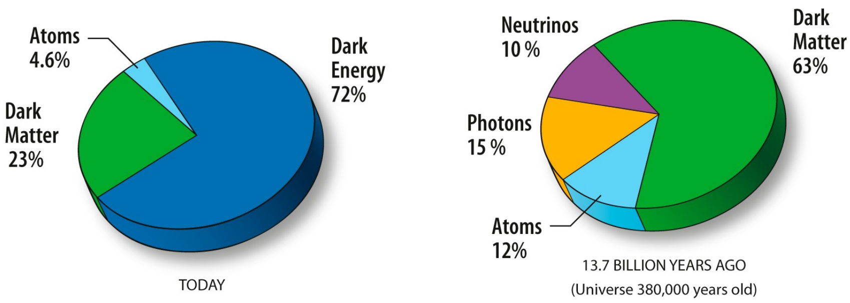

Figure 2.1: Energy density pie chart for the ΛCMD model according to *WMAP* data-set, with today energy densities (left) and during the decoupling (right). (Extracted from: https://map.gsfc.nasa.gov/media/080998/index.html).

2.1.2 Thermal history

According to the ΛCDM model, the very early universe experienced a period of time when particle species were in thermal equilibrium with each other, maintained by the scattering of particles [27,28]. This thermal bath cools down as the Universe expands, while the interaction rate of a given species, i.e. Γ, diminishes. It turns out that, when the temperature of the Universe reaches a sufficiently low value, this interaction rate falls below a certain threshold, provided by the Hubble rate H when $\Gamma < H$, and after that the particle stops interacting and decouples from the thermal bath.

For most of the particles, after decoupling from the thermal bath its contribution is transferred from radiation energy density to the matter-energy density.

The radiation density of all relativistic species obeys the Stefan-Boltzmann law:

$$\rho_r = \frac{\pi^2}{30} g(T) T^4, \tag{2.1}$$

where $g(T)$ is the total number of relativistic degrees of freedom at temperature T contributing to the fluid. Since bosons contribute differently from fermions to the effective number of degrees of freedom at a given temperature T, one has:

$$g(T) = \sum_{bosons} g_b(T) + \frac{7}{8} \sum_{fermions} g_f(T), \tag{2.2}$$

where $g_b(T)$ counts the number of bosonic degrees of freedom in the thermal bath and $g_f(T)$ counts the number of fermionic degrees of freedom present in the same thermal bath at temperature T. Notice that fermions contribute less than bosons. Besides, matter and radiation evolve differently with scale factor:

$$\rho_m = \rho_0 a^{-3} \quad , \quad \rho_r = \rho_0 a^{-4}, \tag{2.3}$$

and, therefore, there is a point in the evolution of the Universe when both quantities are comparable, this period in the cosmological evolution is known as the matter-radiation equivalence era. For the ΛCDM model, using present values of matter and radiation energy densities [7], the scale factor at this period of time is given by:

$$a_{eq} = \frac{\Omega_r}{\Omega_m} \approx 3 \times 10^{-4}, \tag{2.4}$$

happening shortly before the decoupling of photons [29].

Depending on the strength of the interaction, particles will decouple sooner or later from the thermal bath. Therefore, the thermal history for a ΛCDM universe will be strongly influenced by its underlying particle interaction model. As figure (2.2) shows, assuming the standard model of particle physics, the relativistic degrees of freedom from the thermal bath taken into account inside the $g(T)$ function decreases with temperature.

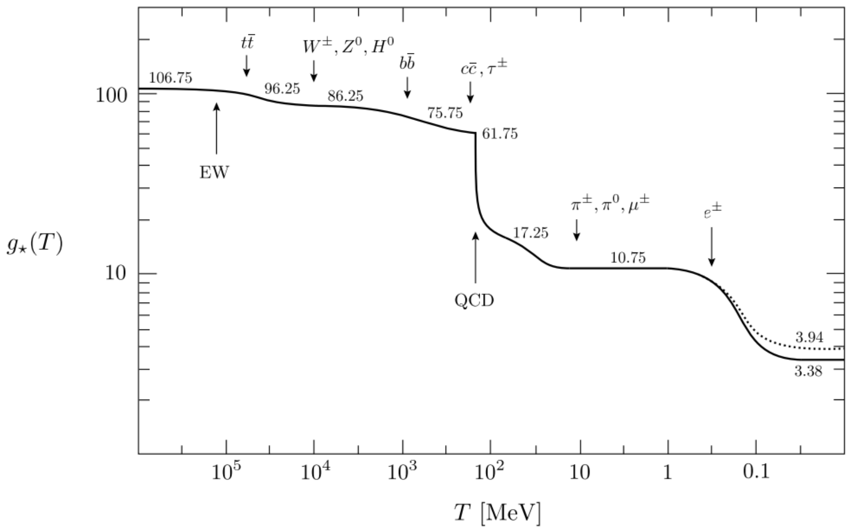

Figure 2.2: Effective number of degrees of freedom contributing as radiation in the thermal bath assuming the standard model for interaction. The plot shows the typical energy scale for electroweak symmetry breaking and the QCD phase transition. At the end of the plot the photon decoupling is shown. Dotted line denotes the number of degrees of freedom contributing to entropy. (Extracted from [27]).

Notice that as the Universe cools down, some particles are no longer relativistic. In the Standard Model of particle physics, weakly interacting particles and their mediator bosons decouple first, later QCD phase transition occurs and baryons are created. Finally, electromagnetically interacting particles do the same, leaving photons free to propagate. As an example, a typical reaction involving electron-positron annihilation:

$$e^- + e^+ \leftrightarrow \gamma + \gamma, \tag{2.5}$$

stops being a reversible process, that normally keeps both particles in equilibrium, when temperature cools down below the electron mass:

$$T << m_e \rightarrow T << 0.51 \ \text{MeV}. \tag{2.6}$$

The thermal history of the Universe is relevant to predict the relic densities due to Big Bang nucleosynthesis. The resulting abundances for Helium, for example, and heavier elements is a reflection of the thermal history followed by the Universe immediately after the Big Bang. As a summary, table (2.2) and figure (2.3), both summarize thermal history of the Universe, including the photon decoupling happening at $z \approx 1100$.

Event	Time	Redshift z	Temperature
Singularity	0 s	∞	∞
Inflation	$\geq 10^{-34}$ s	-	-
Baryogensis	≤ 20 ps	$> 10^{15}$	> 100 GeV
Electro-weak phase transition	20 ps	10^{15}	100 GeV
QCD phase transition	20μs	10^{12}	150 MeV
Neutrino decoupling	1 s	6×10^9	1 MeV
Nucleosynthesis	3 min	4×10^8	100 keV
Matter-radiation equality	60 kyr	3400	0.75 eV
Photon decoupling	380 kyr	1100	0.26 eV
Reionization	$100 - 400$ Myr	$10 - 30$	$2.6 - 7.0$ meV
Dark energy matter equality	9 Gyr	0.4	0.33 meV
Present	13.8 Gyr	0	0.24 meV

Table 2.2: Summary of the most relevant dynamical events before and after the photon decoupling, the temperature scale assuming the Standard Model of particle physics. (Extracted and adapted from [27]).

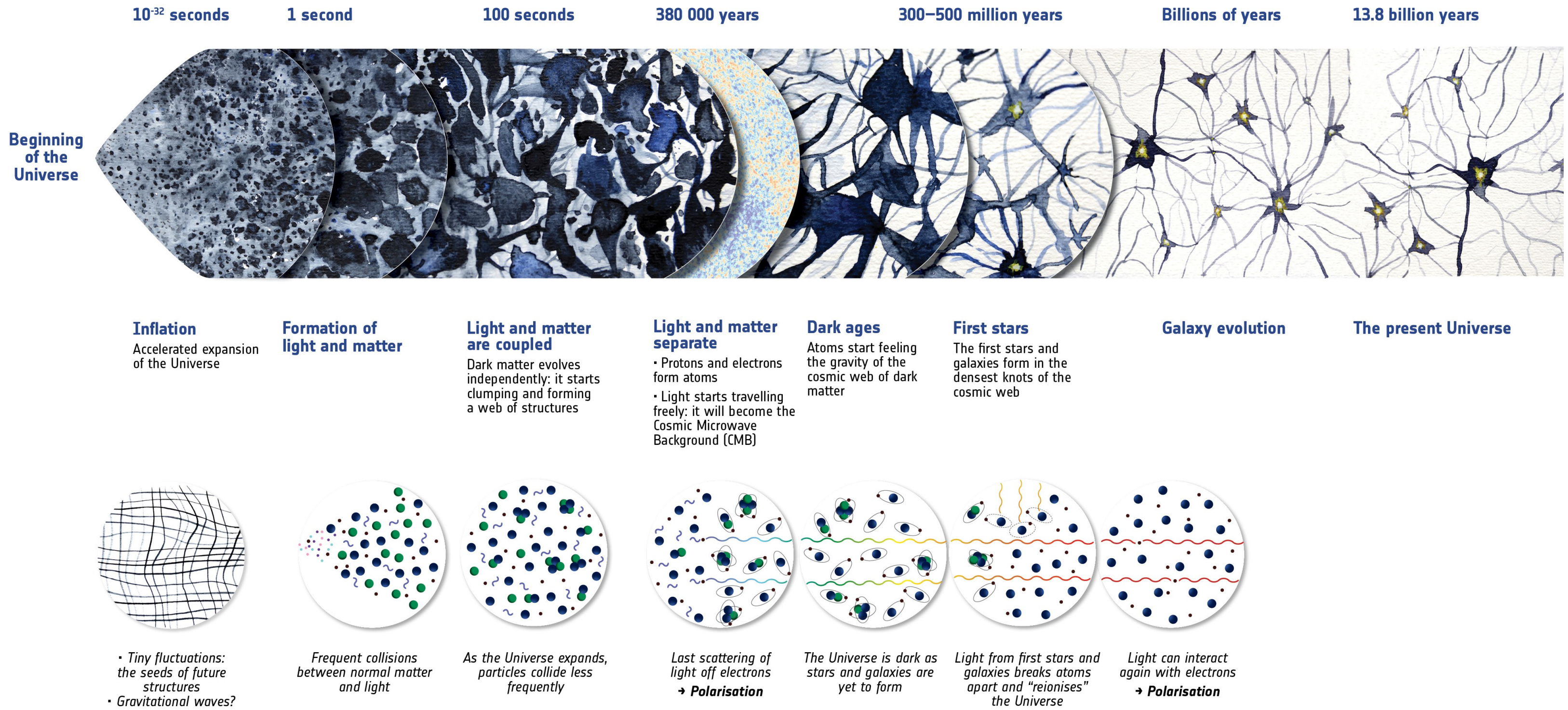

Figure 2.3: Schematic evolution of the Universe and its associated time scale. The diagram shows a pictorical evolution of the observable Universe from the quantum fluctuations associated with inflation to the present epoch. (Extracted from: https://www.cosmos.esa.int/web/planck/picture-gallery)

2.2 Anisotropies

Over the years, several surveys have demonstrated that cosmic microwave background radiation is nearly isotropic, with fluctuations five orders of magnitudes below the black body radiation temperature accurately measured by *COBE* [30]. The same probe showed that a typical magnitude for temperature fluctuations of the CMB is about 10^{-5}K, measuring them at large scales. The probe performed the first measurements of the CMB anisotropies [8] beyond the monopole, measuring dipolar and quadrupolar moments [31]. Several years later, *WMAP* was able to map the anisotropies with increased resolution, measuring the CMB angular power spectrum with signal-to-noise exceeding unity for multipoles $\ell \leq 1060$[1]. Lastly, the *Planck* satellite showed the clearest view of temperature anisotropies accessing multipoles $\ell \leq 2508$[2]. These data sets together have been used to improve the constraints on cosmological parameters [34], as well as their combination with other data sets, such as the measured distribution of galaxies [35] and supernovae data [36]. In fact, current data support the idea of fluctuations in the early universe that evolved into clumps of matter at very different size scales. In the following pages we summarize the most important aspects from perturbation theory needed to derive the CMB anisotropies.

2.2.1 Gravitational perturbations

The most general perturbation approach that can be used implies a gauge invariant scalar, vector, tensor decomposition (SVT) [4, 27, 28]. To linearize Einstein's field equations, a given set of fields is introduced in the Friedmann-Lemaitre-Robertson-Walker (FLRW) metric [16]. Writing this metric in conformal coordinates, one has:

$$ds^2 = a^2(\eta)[-(1+2\phi)d\eta^2 + 2A_i dx^i d\eta + ((1-2\psi)\delta_{ij} + h_{ij})dx^i dx^j], \tag{2.7}$$

where ϕ, A_i, h_{ij}, are the scalar, vector and tensor perturbations, respectively. However, some fields are spurious and can be eliminated through an appropriate choice of gauge. An example of choice of gauge is the Newtonian one [4, 27] which allows to write the perturbed line element as:

$$ds^2 = a^2(\eta)[-(1+2\Phi)d\eta^2 + (1-2\Psi)dx^2], \tag{2.8}$$

where a is the scale factor, Ψ is the spatial metric perturbation, and Φ is the Newtonian potential (commonly seen in the weak gravity regime). By analogy with the metric perturbations in equation (2.8), an SVT decomposition can be introduced in the stress-energy tensor $T_{\mu\nu}$. Separating components, the perturbed stress-energy tensor [4, 29] is written as:

$$\delta T^0{}_0 = -\delta\rho, \qquad \delta T^0{}_i = (\bar{\rho} + \bar{P})v_i, \qquad \delta T^i{}_j = -\delta P \delta^i{}_j - \Pi^i{}_j, \tag{2.9}$$

[1]The upper limit on ℓ corresponds to that of reference [32]
[2]The upper limit on ℓ corresponds to that of reference [33]

where fluctuations over pressure and energy density are labeled as $\delta\rho$ and δP respectively, v_i is the bulk velocity of the fluid and $\Pi^i{}_j$ the stress-anisotropy tensor. Usually perturbations are set in such a way that stress anisotropies are null[3]. Using the perturbed metric in the Newtonian gauge, together with the perturbed stress-energy tensor, evolution equations for Ψ and Φ are derived [4]:

$$\nabla^2\Psi - 3\mathcal{H}(\Psi' + \mathcal{H}\Phi) = -4\pi G a^2 \delta\rho, \tag{2.10}$$

$$\partial_i(\Psi' + \mathcal{H}\Phi) = 4\pi G a^2(\bar{\rho} + \bar{P})v_i, \tag{2.11}$$

$$\Psi'' + 2\mathcal{H}(2\Psi + \Phi)' + (2\mathcal{H}' + \mathcal{H}^2)\Phi + \frac{1}{2}\nabla^2(\Psi - \Phi) = 4\pi G a^2 \delta P, \tag{2.12}$$

$$-\frac{1}{2}\partial_i\partial_j(\Phi - \Psi) = 4\pi G a^2 \Pi^i{}_j, \tag{2.13}$$

This set of coupled differential equations establish the dynamics in the primordial universe.

2.2.2 Boltzmann equations for photons

For a complete derivation of the anisotropies in the CMB, we need also to take into account the evolution of their probability density distribution. Since photons are propagating in a time evolving gravitational potential, it is expected that photon paths are modified by this gravitational potential. In the context of linear perturbation theory, the temperature of the CMB can be written as follows:

$$\Theta(\boldsymbol{x}, \boldsymbol{p}, \eta) = \Theta_0 + \Theta(\boldsymbol{x}, |\boldsymbol{p}|, \eta), \tag{2.14}$$

where Θ_0 is the black body temperature, and $\Theta(\boldsymbol{x}, |\boldsymbol{p}|, \eta)$ are the anisotropies in the photon radiation distribution.

Another feature from the Boltzmann equation comes from CMB photons interacting with electrons after the recombination epoch. These scatterings are another source of distortion for the Boltzmann distribution being important in the context of CMB polarization. The process is driven by the Thomsom scattering amplitude [4,28]:

$$|\mathcal{M}|^2 = 6\pi\sigma_T m_e^2(1 + \cos^2[\hat{\boldsymbol{p}} \cdot \hat{\boldsymbol{p}}']), \tag{2.15}$$

where σ_T is the Thomson scattering cross section describing the efficiency of the process, $\hat{\boldsymbol{p}}$ is the incident collision momentum, $\hat{\boldsymbol{p}}'$ the momentum of the photon after collision with electrons. In Fourier space, Boltzmann's equation leads into an evolution equation that depends on the temperature perturbations:

$$\dot{\Theta} + ik\mu\Theta = -\dot{\Phi} - ik\mu\Psi - \Gamma\left[\Theta - \Theta_0 - i\mu\boldsymbol{v}_e\right], \tag{2.16}$$

[3] Neutrinos modify this assumption [4].

where μ is the cosine of the angle between $\hat{\boldsymbol{p}}$ and $\hat{\boldsymbol{p}}'$, $\hat{\boldsymbol{v}}_e$ is the velocity of the electrons in the comoving frame, k is the wave-vector used in Fourier transformations, and Γ is the scattering rate of the photons off the electrons.

Accordingly, CMB fluctuations Θ can be fully integrated by specifying the potentials and the baryon fluid velocity: Φ, Ψ, and v_e[4]; however, baryons evolve in the perturbed background, and the gravitational potential is a function that depends on the matter density contrast generated by gravitational potential. As a consequence, a few more equations are needed to fully describe the dynamics of the CMB photons. These equations can be derived from the Boltzmann equations for other components evolving with the CMB obtaining a system of coupled differential equations [4]. The relevant equations for computing the CMB anisotropies are given by:

$$\dot{\Theta} + ik\mu\Theta = -\dot{\Phi} - ik\mu\Psi - \dot{\tau}[\Theta_0 - \Theta + \mu v_b + \frac{1}{2}\mathcal{P}_2(\mu)(\Theta_2 + \Theta_{P_2} + \Theta_{P_0})], \tag{2.17}$$

$$\dot{\delta} + ikv = -3\dot{\Phi}, \tag{2.18}$$

$$\dot{v} + \frac{\dot{a}}{a}v = -ik\Psi, \tag{2.19}$$

$$\dot{\delta}_b + ikv_b = -3\dot{\Phi}, \tag{2.20}$$

$$\dot{v}_b + \frac{\dot{a}}{a}v_b = -ik\Psi + \frac{\dot{\tau}}{R}[v_b + 3i\Theta_1], \tag{2.21}$$

$$\dot{\mathcal{N}} + ik\mu\mathcal{N} = -\dot{\Phi} - ik\mu\Psi, \tag{2.22}$$

$$\Theta_P + ik\mu\Theta_P = -\dot{\tau}[-\Theta_P + \frac{1}{2}(1 - \mathcal{P}_2(\mu))(\Theta_2 + \Theta_{P_2} + \Theta_{P_0})], \tag{2.23}$$

where δ and δ_b are density contrast for matter and baryons, and Θ_1 is the dipole of the CMB; v and v_b are the bulk velocities of the fluids in the stress-energy tensor, equation (2.9), for matter and baryons respectively; $\mathcal{N}$ is the neutrino energy density perturbation, and τ is the optical depth. Equation (2.23) is the dynamical equation for strength of the polarization field Θ_P [4].

The set of equations (2.17)- (2.22) are used to evolve the dynamics of the universe for: matter density perturbation, CMB anisotropies, gravitational potentials, and neutrinos simultaneously. It is worth to mention that several codes perform this task, for example, `CLASS` [37] and `CAMB` [38]. In the next chapters, `CAMB` is used to evolve anisotropies and calculate the CMB 2-point correlation function, or the angular power spectrum C_ℓ, from the cosmological parameters.

[4] v_e is equal to v_b (the velocity of baryons in the fluid)

2.3 The CMB power spectra

As it was discussed in the last section, temperature and polarization anisotropies are described by equations (2.17)-(2.23). By writing the CMB anisotropies in Fourier space, Θ can be expanded by using Legendre polynomials $P_\ell(\mu)$ [29]:

$$\Theta(\hat{\boldsymbol{k}}, \mu) = \sum_{\ell=0}^{\infty} (2\ell+1)(-i)^\ell \Theta_\ell(\hat{\boldsymbol{k}}) P_\ell(\mu), \tag{2.24}$$

where $\Theta_\ell(\hat{\boldsymbol{k}})$ coefficients are given by:

$$\Theta_\ell(\hat{\boldsymbol{k}}) = \frac{i^\ell}{2} \int_{-1}^{1} d\mu \Theta(\hat{\boldsymbol{k}}, \mu) P_\ell(\mu), \tag{2.25}$$

notice that using this decomposition one can write:

$$\langle \Theta_\ell(\hat{\boldsymbol{k}}) \Theta^*_{\ell'}(\hat{\boldsymbol{k}}') \rangle = \Theta_\ell(|\hat{\boldsymbol{k}}|)(2\pi)^3 \delta^{(3)}(\hat{\boldsymbol{k}} - \hat{\boldsymbol{k}}')\delta_{\ell\ell'}, \tag{2.26}$$

and this specific property translates into statistical isotropic and homogeneous anisotropies in the CMB temperature. By applying an inverse Fourier transform over the modes for $\Theta(\hat{\boldsymbol{k}}, \mu)$, the real space anisotropies are recovered [29]. From this equation we can calculate the cross-correlation of the temperature fluctuation $\frac{\Delta T}{T}$:

$$\left\langle \frac{\Delta T}{T}(\hat{\boldsymbol{n}}) \frac{\Delta T}{T}(\hat{\boldsymbol{n}}') \right\rangle = \frac{1}{2\pi^2} \sum_\ell \left(\int dk k^2 \Theta_\ell(\hat{\boldsymbol{k}}) \right) (2\ell+1) P_\ell(\mu), \tag{2.27}$$

where the angular temperature power spectrum C_ℓ^{TT} is derived[5]:

$$C_\ell^{TT} = \frac{2}{\pi} \int dk k^2 \Theta_\ell(\hat{\boldsymbol{k}}). \tag{2.28}$$

If recombination can be considered as instantaneous, we can see that temperature fluctuations in the CMB are dominated by three main contributions [4]:

$$\frac{\Delta T}{T} \approx \Psi + \Theta_0 + 2\int_0^{\eta_0} d\eta (\dot{\Phi} + \dot{\Psi}) - \boldsymbol{n} \cdot (\boldsymbol{v}_0 - \boldsymbol{v}_e), \tag{2.29}$$

containing the Sachs-Wolfe (SW) effect due to the additional redshift that photons experience when climbing gravitational potentials; the integrated Sachs-Wolfe effect (ISW), which considers all the contributions from time-varying gravitational potential along the line of sight; and the Doppler effect originated from the baryon-photon fluid.

[5]Where the relation $\left\langle \frac{\Delta T}{T}(\hat{\boldsymbol{n}}) \frac{\Delta T}{T}(\hat{\boldsymbol{n}}') \right\rangle = \frac{1}{4\pi} \sum_\ell (2\ell+1) C_\ell P(\hat{\boldsymbol{n}} \cdot \hat{\boldsymbol{n}}')$ has been used.

Each of these terms contributes to the total measured spectrum in all scales, as can be seen in figure (2.4).

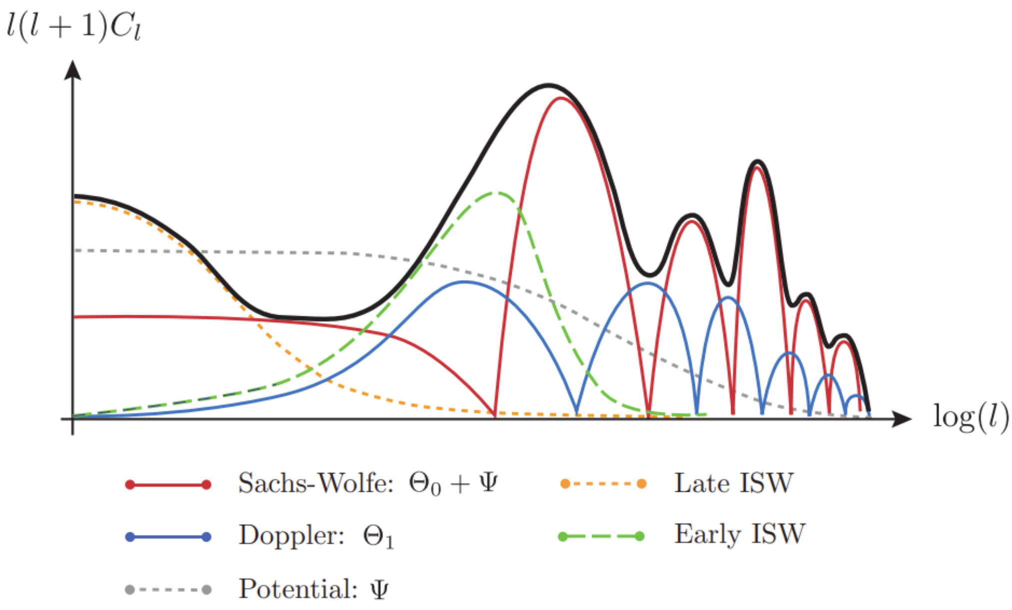

Figure 2.4: Main contributions for the temperature power spectra for the Sachs-Wolfe effect (SW: red), Integrated Sachs-Wolfe effect (ISW: green and orange), and Doppler effect: (blue). The pure gravitational contribution is also showed (gray). (Extracted from [39]).

2.3.1 Polarization Anisotropies

In addition to scalar perturbations characterized by Ψ and Φ increasing evidence in CMB supports the existence of polarized anisotropies [40–42]. These tensor perturbations leave characteristic imprints in the CMB anisotropies, that are used as independent data in addition to the temperature anisotropies with a similar formalism used to derive the temperature power spectrum [43]. In principle any electromagnetic signal can be described by a Stokes vector, containing the intensity and the polarization of the signal. Starting from the polarization tensor [44], we have:

$$\mathcal{P}(\hat{\boldsymbol{n}}) = I(\hat{\boldsymbol{n}})\boldsymbol{I} + U(\hat{\boldsymbol{n}})\boldsymbol{\sigma_x} + V(\hat{\boldsymbol{n}})\boldsymbol{\sigma_y} + Q(\hat{\boldsymbol{n}})\boldsymbol{\sigma_z}, \tag{2.30}$$

where $I(\hat{\boldsymbol{n}})$, $Q(\hat{\boldsymbol{n}})$, $U(\hat{\boldsymbol{n}})$, $V(\hat{\boldsymbol{n}})$, are the Stokes parameters for the signal in $\mathcal{P}(\hat{\boldsymbol{n}})$, the representation basis of $\mathcal{P}(\hat{\boldsymbol{n}})$ is the Pauli basis: $(\boldsymbol{I}, \boldsymbol{\sigma_i})$, where $\boldsymbol{\sigma_i}$, are the Pauli matrices [44, 45].

Stokes parameters describe the electromagnetic wave: I corresponds to the total intensity, Q is the vertical polarization in a reference frame fixed by the observer, and U the horizontal polarization relative to the same reference frame used for U[6], and V denotes the circular polarization. Photon polarization states are generated from anisotropic differences in the temperature of the baryon-photon fluid, creating an additional source of anisotropies in the CMB from Thomson scattering, the effect is accounted in a polarization dependent term in Thomson scattering differential cross-section [4,6]:

$$\frac{d\sigma}{d\Omega} \propto |\hat{\boldsymbol{\epsilon}}_{\mathrm{i}} \cdot \hat{\boldsymbol{\epsilon}}_{\mathrm{f}}|^2, \tag{2.31}$$

where $\hat{\boldsymbol{\epsilon}}_{\mathrm{i}}$ is the polarization of the incoming photon, and $\hat{\boldsymbol{\epsilon}}_{\mathrm{f}}$ the polarization of the outgoing photon, the most efficient scattering correspond to an incoming polarization parallel to the outgoing one [6].

From the linear perturbation theory one expects that CMB photons are roughly 10% polarized [29]. Figure (2.5) shows an example of the CMB map, after proper cleaning of the foreground sources, containing non-null Stokes parameters associated to polarization (i.e. $\boldsymbol{Q}(\hat{\boldsymbol{n}})$ and $\boldsymbol{U}(\hat{\boldsymbol{n}})$).

[6]We adopt the frame used in `HEALPix` projection maps (see Appendix A)

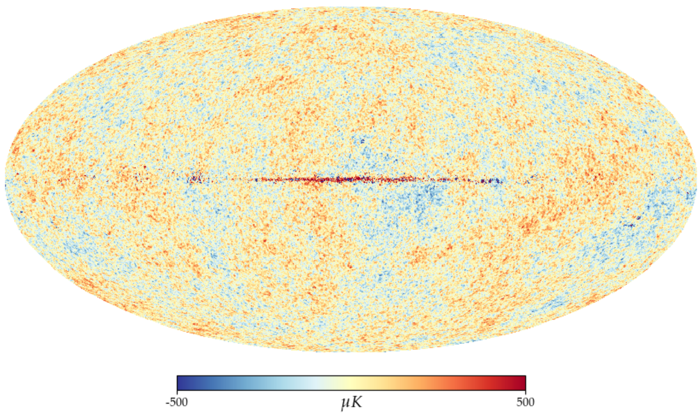

(a) Stokes parameter: I

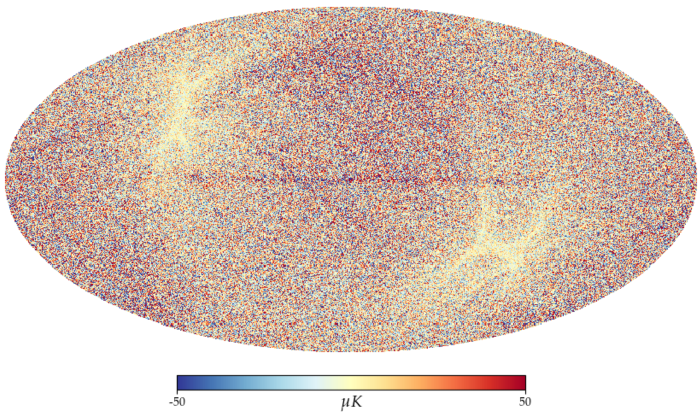

(b) Stokes parameter: Q

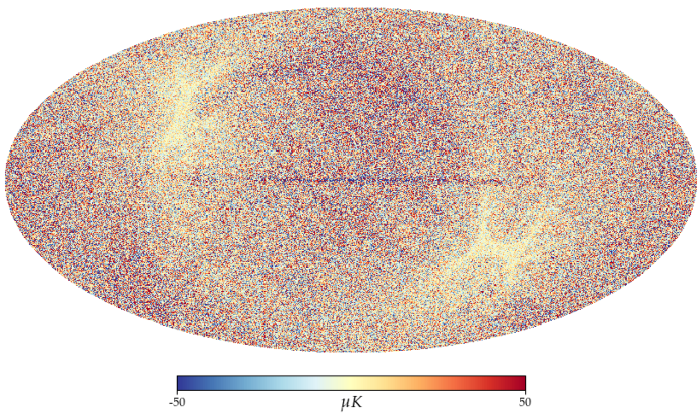

(c) Stokes parameter: U

Figure 2.5: High resolution sky map `Commander` in Galactic coordinates showing anisotropies in all of the Stokes parameters. Notice that the scale for Intensity map is dominant (a) being 10 times bigger than for polarization maps (b) and (c). The maps also show remaining polarized galaxy emission at the center of each plot. (Reproduced from: https://pla.esac.esa.int)

Another feature from polarization is that, as for the temperature, it is possible to define a power spectrum from the Stoke's parameters (see [29] for a detailed derivation). In order to define their power spectra, careful attention is needed in order to take into account the fact that Q and U are not rotational invariant quantities. In contrast with the intensity they depend on the observer's frame, and a specific combination of Q and U is needed to calculate the spectra. This decomposition on $a_{\ell m}$ coefficients leads into the E-mode and B-mode polarization coefficients [29, 45]. The Stokes parameter combination $Q \pm iU$ transforms as follows :

$$(Q \pm iU)'(\hat{\boldsymbol{n}}) = e^{\mp 2i\phi}(Q \pm iU)(\hat{\boldsymbol{n}}), \tag{2.32}$$

where ϕ is the phase observed in polarization after a rotation. This transformation property is used to project the polarization parameters in a different spherical harmonic basis [43, 45, 46]. This projection is given by:

$$(Q(\hat{\boldsymbol{n}}) + iU(\hat{\boldsymbol{n}})) = \sum_{l=0}^{\infty} \sum_{m=-\ell}^{\ell} a_{2,\ell m}\ {}_2Y_\ell^m(\hat{\boldsymbol{n}}) \quad , \tag{2.33}$$

$$(Q(\hat{\boldsymbol{n}}) - iU(\hat{\boldsymbol{n}})) = \sum_{l=0}^{\infty} \sum_{m=-\ell}^{\ell} a_{-2,\ell m}\ {}_{-2}Y_\ell^m(\hat{\boldsymbol{n}}) \quad , \tag{2.34}$$

where the functions ${}_{\pm 2}Y_\ell^m(\hat{\boldsymbol{n}})$ are the spin-weighted spherical harmonics[7], from where we define the electric, $a^E_{\ell m}$, and magnetic coefficients $a^B_{\ell m}$ [29]:

$$a^E_{\ell m} = -(a_{2,\ell m} + a_{-2,\ell m})/2 \qquad , a^B_{\ell m} = -(a_{2,\ell m} - a_{-2,\ell m})/2i. \tag{2.35}$$

Using these coefficients the following set of spectra can be formed:

$$\langle a^{*E}_{\ell m} a^E_{\ell m'}\rangle = \delta_{\ell\ell'}\delta_{mm'}\mathcal{C}^{EE}_\ell, \quad \langle a^{*B}_{\ell m} a^B_{\ell m'}\rangle = \delta_{\ell\ell'}\delta_{mm'}\mathcal{C}^{BB}_\ell, \quad \langle a^{*T}_{\ell m} a^T_{\ell m'}\rangle = \delta_{\ell\ell'}\delta_{mm'}\mathcal{C}^{TT}_\ell, \tag{2.36}$$

$$\langle a^{*B}_{\ell m} a^E_{\ell m'}\rangle = \delta_{\ell\ell'}\delta_{mm'}\mathcal{C}^{BE}_\ell, \quad \langle a^{*T}_{\ell m} a^E_{\ell m'}\rangle = \delta_{\ell\ell'}\delta_{mm'}\mathcal{C}^{TE}_\ell, \quad \langle a^{*T}_{\ell m} a^B_{\ell m'}\rangle = \delta_{\ell\ell'}\delta_{mm'}\mathcal{C}^{BT}_\ell \tag{2.37}$$

where C^{TT}_ℓ is the temperature power spectrum, C^{EE}_ℓ the electric power spectrum, C^{BB}_ℓ the magnetic power spectrum, C^{BE}_ℓ the magnetic to electric power spectrum, C^{TE}_ℓ the temperature to electric power spectrum, and $\mathcal{C}^{TE}_\ell$ the temperature to magnetic power spectrum. By symmetry considerations $\mathcal{C}^{BE}_\ell$ and $\mathcal{C}^{BT}_\ell$ are zero [43]. Figure (2.6) shows the 5 non-zero power spectra, notice that due to the low polarization fraction in the CMB anisotropies, near 10%, temperature spectrum has the dominant signal.

[7]See Appendix in [43] for discussion of properties of spin-weighted spherical harmonics.

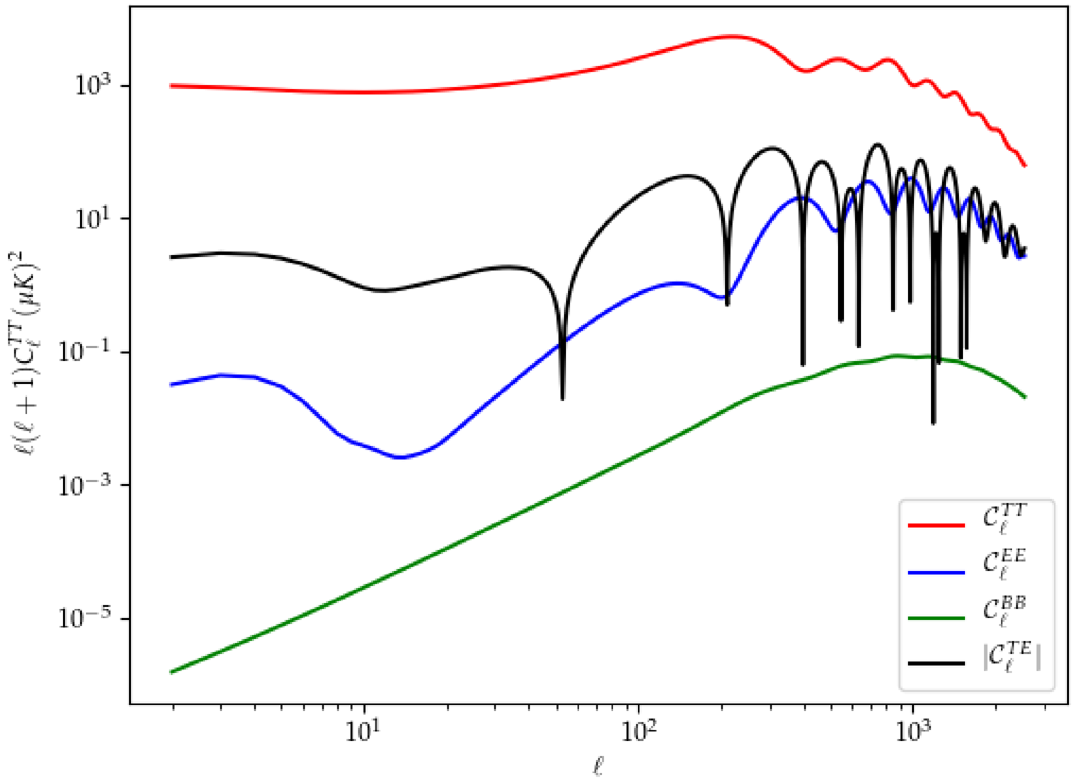

Figure 2.6: Power spectra from `CAMB` code. The hierarchy in the power ordering gives a bigger signal for temperature $\mathcal{C}_\ell^{TT}$ and its correlation function with modulus of the polarization component $\mathcal{C}_\ell^{TE}$. Polarization spectra (i.e. $\mathcal{C}_\ell^{EE}$ and $\mathcal{C}_\ell^{BB}$) are always subdominant in comparison with the temperature in all the scales.

2.3.2 Cosmological parameters dependence

The ΛCDM model as the standard model of cosmology has a set of relevant parameters. Although, there are several competing theories from where ΛCDM model is a limit case, the model is still phenomenologically successful. In the following we consider the minimal set of relevant constants that fully parameterize a given universe, this set of cosmological parameters is used by *Planck* collaboration as the minimal set of parameters that best fits the measured CMB anisotropies [7, 33], known as the base ΛCDM model. They are summarized in table (2.3). Two types of parameters are shown: those used as input for solving the perturbation equations (upper part of the table) and those derived from the obtained solution.

Parameter	Name	Fiducial value
$\Omega_b h^2$	Physical baryon energy density	0.02237
$\Omega_c h^2$	Physical cold dark matter energy density	0.1200
$100\Theta_{MC}$	Acoustic horizon scale	1.04092
τ	Optical depth due to reionization	0.0544
$\ln(10^{10}A_s)$	Primordial scalar amplitude	3.044
n_s	Spectral scalar index	0.9649
Ω_k	Curvature energy density fraction	0.0
H_0	Hubble constant	67.36 km s^{-1}Mpc^{-1}
Ω_m	Matter energy density fraction	0.3153
σ_8	Galaxy clustering at $8\mathrm{h}^{-1}\mathrm{Mpc}$	0.8111

Table 2.3: Summary of the base-ΛCDM + Ω_k parameters and their used values in `CAMB`. Fiducial values are the ones reported in the best fit *Planck* collaboration analysis from the `TT+TE+EE+lowE+lensing` likelihood combination [7]. Curvature energy density Ω_k is added, and assumed zero by construction. Derived parameters are in the lower half of the table.

Figures (2.7) and (2.8) show the dependence of the temperature power spectrum with the parameters of the base ΛCDM model.

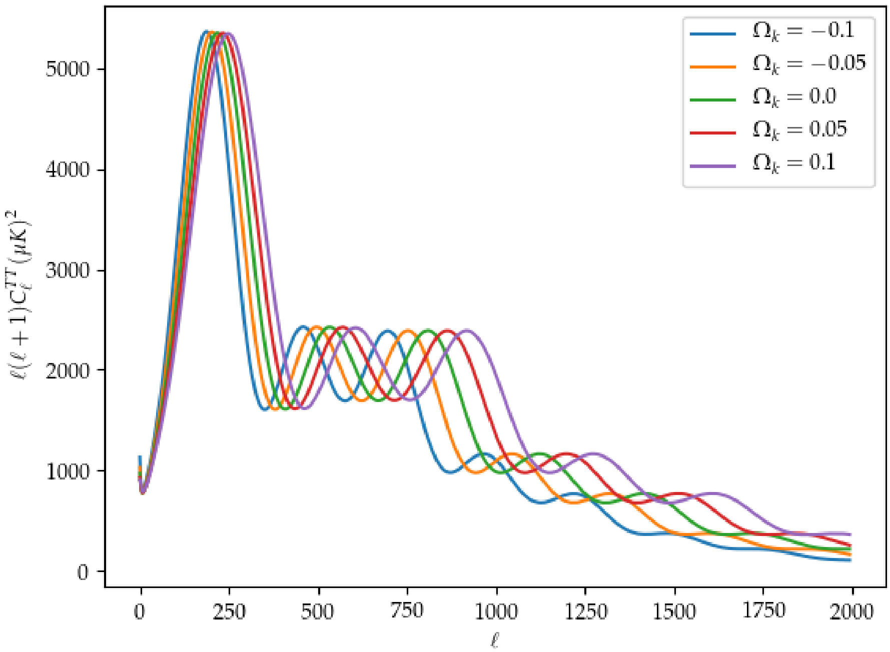

Figure 2.7: Variation of curvature energy density fraction Ω_k showing the shift expected in acoustic peaks in the CMB temperature power spectrum.

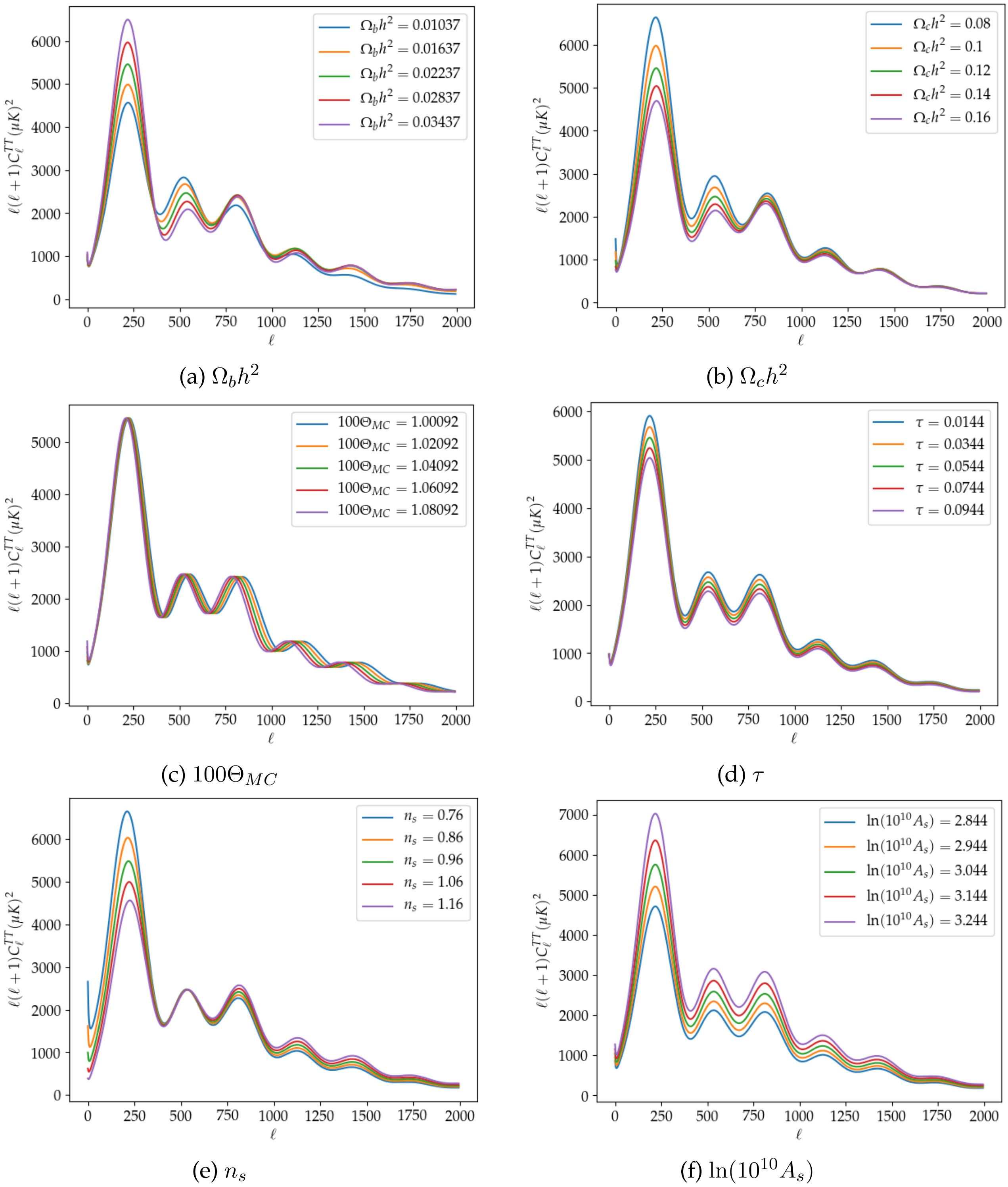

(a) $\Omega_b h^2$ (b) $\Omega_c h^2$

(c) $100\Theta_{MC}$ (d) τ

(e) n_s (f) $\ln(10^{10}A_s)$

Figure 2.8: Temperature power spectrum variation by evolving Boltzmann equations with slightly modifications in fiduciary cosmological parameters values in table (2.3). The set of cosmological parameters ($\Omega_b h^2$, $\Omega_c h^2$, Θ_{MC} ,τ, $\ln(10^{10}A_s)$,n_s) varied here are those refereed as a sampled parameters in the context of chapter 4.

2.4 Summary

We have presented in this chapter an introduction to the CMB anisotropies by revisiting the thermal history predicted by the ΛCDM model. From Boltzmann equations, we summarized the calculation of the anisotropies, within the linear perturbation theory, used by codes as `CAMB`. We have shown the formalism needed to derive the dynamics of the photons for both temperature and polarization. We show the relevance properties needed from polarization data to be used in other chapters.

We finished this chapter, by showing the dependence on the cosmological parameters of the CMB temperature power spectrum. We computed the Boltzmann equations for CMB temperature spectrum by varying the best-fit base-ΛCDM cosmological parameters (i.e a subset of cosmological parameters, in addition to the curvature energy density, studied by *Planck* collaboration [33] in a six-dimensional parameter space given by: ($\Omega_b h^2$, $\Omega_c h^2$, Θ_{MC} ,τ, $\ln(10^{10} A_s)$,n_s)) to show how sensitive the temperature power spectrum is under variations of these parameters. We used this subset of cosmological parameters as a reference in chapter 4 for cosmological parameters estimation.

3 | Modeling kinematic effects

The first evidence that our solar system is not at rest comes from Jacobus Kapteyn in 1904, showing that the solar system is moving with respect to the nearby stars [47]. Later, as astrophysicists were able to probe larger scales in the universe, increased evidence suggested that even the Milky Way was moving with respect to nearby galaxies (i.e. the blue-shift measurement from the Andromeda galaxy or the detected movement towards Virgo super-cluster by using redshift measurements from nearby galaxies [48, 49]). These work proved that observers on Earth (and even in the local group) are not comoving observers and, consequently, they are not able to measure statistically isotropic CMB anisotropies. With satellites measuring the anisotropies (i.e. *COBE*, *WMAP* and *Planck*), kinematic effects started to appear in data showing the signatures expected from the Doppler dipole (detected first in full sky mode by *COBE*, then by *WMAP* and *Planck*), and Doppler modulation and relativistic aberration (both detected by *Planck*). It is argued in [50], that this relative motion of the solar system appears to be important in the context of supernovae data as a potential source of systematic effects. In this chapter, we focus on defining the theoretical background behind relativist effects in the CMB. The relevant frames used to interpret the CMB dipole due to the solar system peculiar velocity is presented. We discuss the appearance of a non-vanishing cross-correlation, in nearby multipoles, by relativistic Doppler modulation and aberration effects. The use of this correlation in determining the relative velocity of the solar system with respect to the CMB comoving frame is shown. Lastly, we show the changes in the CMB power spectra due to kinematic effects associated to observers moving at different velocities with respect to the CMB frame.

3.1 Frames

In this chapter, we adopt the interpretation given by *Planck* collaboration in dealing with the solar dipole in the CMB. This interpretation is that the power observed in the dipole is coming mostly from the Doppler boost of the monopole [11] due to the peculiar velocity of the solar system with respect to the CMB, neglecting intrinsic contributions from the ΛCDM model. By assuming this interpretation we identify three relevant frames, used by the collaboration and in this work, for measuring the solar system peculiar velocity $\boldsymbol{\beta}$, these are:

- CMB comoving frame: It is the frame defined as the one where the CMB anisotropies are statistically isotropic [4, 29]. Observers in this frame will not measure any Doppler effect, neither any relativistic aberration effects, except those expected from the gravitational potential described in the linear perturbation theory [4] (i.e. Sachs-Wolfe effect).

- Satellite reference frame: The satellite is placed orbiting (and spinning) around the Lagrange point L2 [10]. It is one of the five equilibrium points in terms of gravitational force of the Sun-Earth system. This point has been used along the time to perform measurements concerning the CMB (i.e. *WMAP* and *Planck*)[1]. The relative motion of the satellite with respect to the Sun generates an additional dipolar contribution to the CMB called the orbit dipole that is subdominant with respect to the solar dipole [12, 52]. The orbit dipole has a velocity of $\beta_{\mathrm{orb}} = 1.0 \times 10^{-4}$, one order of magnitude less than the solar dipole $\beta_{\mathrm{dip}} = 1.23 \times 10^{-3}$ [53].

- Solar system barycenter frame: It is the frame centered at the barycenter of the solar system. This frame is defined by the International Earth Rotation Service (IERS) using measurements of distant extragalactic radio sources [54].

Figure (3.1) illustrates the relative position of the *Planck* satellite, at the Lagrange point L2 in motion with respect to the sun, in addition to the spinning of the satellite in its reference frame used to scan the sky. The observational point is located at 1.5×10^6 km beyond the Earth's orbit.

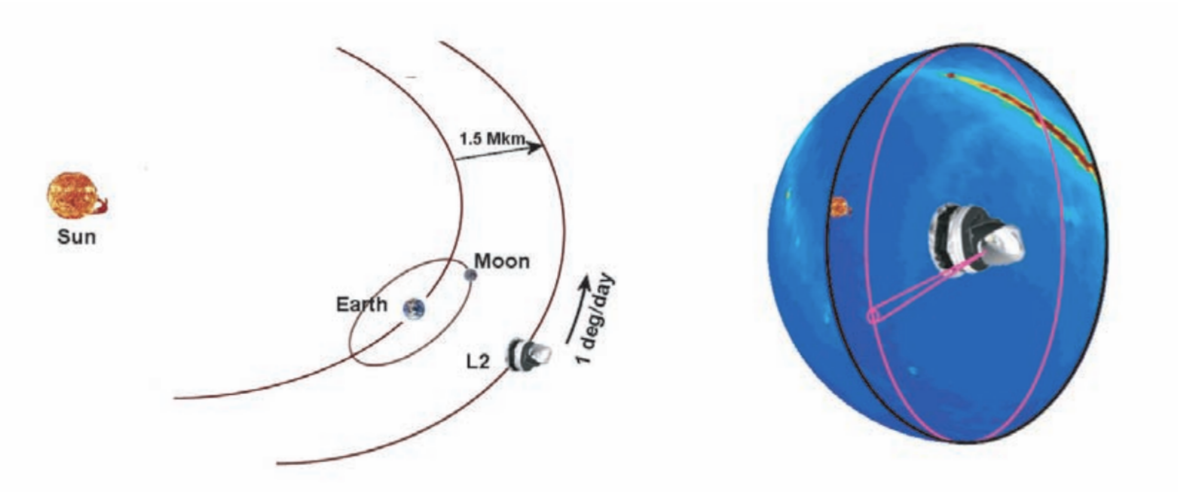

Figure 3.1: Relative position of the *Planck* satellite in the L2 point in the solar system (left) and an illustration of scanning strategy employed by the satellite (right). The spacecraft relative orientation is transformed into Equatorial (J2000) coordinates on Earth, and later in galactic coordinates centered at the sun. (Extracted from [10])

In all the analyses performed here, we have, therefore, neglected a possible intrinsic (i.e. cosmological) dipole. Further information concerning the impact of the intrinsic dipole contribution can be found in [55].

[1] *COBE* satellite was not placed in the L2 point but rather in a Sun-synchronous orbit [51].

3.2 Kinematic effects

We start modeling kinematic effects in the CMB anisotropies by showing the transformation rule connecting measurements from the observer in a moving frame with respect to the CMB comoving frame. The transformation rule is driven by Lorentz transformations over the Planck distribution for photons [11,14]. For the temperature of the photons, we have:

$$T(\hat{\boldsymbol{n}}) = \frac{T'(\hat{\boldsymbol{n}}')}{\gamma(1-\hat{\boldsymbol{n}}\cdot\boldsymbol{\beta})}, \tag{3.1}$$

where $T(\hat{\boldsymbol{n}})$ is the observed temperature in the moving frame, $T'(\hat{\boldsymbol{n}}')$ is the CMB temperature measured by a comoving observer, $\boldsymbol{\beta} = \boldsymbol{v}/c$ is the velocity of the observer in units of the speed of light, $\hat{\boldsymbol{n}}$ is the photon direction in the sky measured by the observer in the moving frame, and $\hat{\boldsymbol{n}}'$ is the direction in the sky measured by a comoving observer. Additionally, the shift in direction is given by [11,14]:

$$\hat{\boldsymbol{n}} = \frac{\hat{\boldsymbol{n}}' + [(\gamma-1)\hat{\boldsymbol{n}}'\cdot\hat{\boldsymbol{\beta}} + \gamma\beta]\hat{\boldsymbol{\beta}}}{\gamma(1+\hat{\boldsymbol{n}}'\cdot\boldsymbol{\beta})}, \tag{3.2}$$

where γ is the usual relativistic factor given by:

$$\gamma = \frac{1}{\sqrt{1-\beta^2}}. \tag{3.3}$$

The notation used in equations (3.1) and (3.2) has been chosen to be consistent with the one used in [11]. As it is stated in [31], and according to the independent measurements of the peculiar velocity of the solar system [49], the Doppler shift in photon's temperature in equation (3.1) can be linearized. The expansion leads to a separation of the kinematic effects affecting the anisotropies, showing the contributions to the observed temperature $T(\hat{\boldsymbol{n}})$ in the moving frame:

$$\begin{aligned} T(\hat{\boldsymbol{n}}) = \underbrace{T_0}_{\text{Monopole}} &+ \underbrace{T_0(\boldsymbol{\beta}\cdot\hat{\boldsymbol{n}})}_{\text{Doppler Dipole}} + \underbrace{\delta T'(\hat{\boldsymbol{n}})}_{\text{Anisotropies}} + \\ &\underbrace{\delta T'(\hat{\boldsymbol{n}})(\boldsymbol{\beta}\cdot\hat{\boldsymbol{n}})}_{\text{Doppler modulation}} - \underbrace{\boldsymbol{\nabla} T'(\hat{\boldsymbol{n}})\cdot\boldsymbol{\nabla}(\boldsymbol{\beta}\cdot\hat{\boldsymbol{n}})}_{\text{Relativistic aberration}} + \underbrace{\mathcal{O}(\beta^2)}_{\text{Higher order corrections}} , \end{aligned} \tag{3.4}$$

which is a Taylor expansion in $\boldsymbol{\beta}$ for equation (3.1), from where equation (3.2) has been linearized in what it is called the weak lensing approximation for relativistic aberration effects (see section 3.2.2) [11,13,56].

Notice that in the perturbative expansion used to derive equation (3.4), the monopole contribution corresponds to the black body radiation temperature. One can also see the dipole due to the Doppler shift of the photon's frequency, as well as terms associated to Doppler modulation and relativistic aberration on the photon direction. Figure (3.2) shows two sky maps measured by different observers: one in a comoving frame and another that moves with a certain velocity with respect to the CMB. The relative motion between the observer and the CMB generates a dipole anisotropy in the direction of the motion (second term in equation (3.4)) superimposed to the monopole. According to equation (3.4), additional kinematic effects are present in all angular scales (modulation and aberration), but are not visible in the plot at the top of figure (3.2), because they are much smaller in amplitude in comparison to the monopole and dipole terms.

In figures (3.2), (3.3), and (3.4), in order to model the impact of the boost on the anisotropies, we have used `HEALPix` C++ libraries to change the temperature and/or the direction of the photons according to equations (3.1) and (3.2).

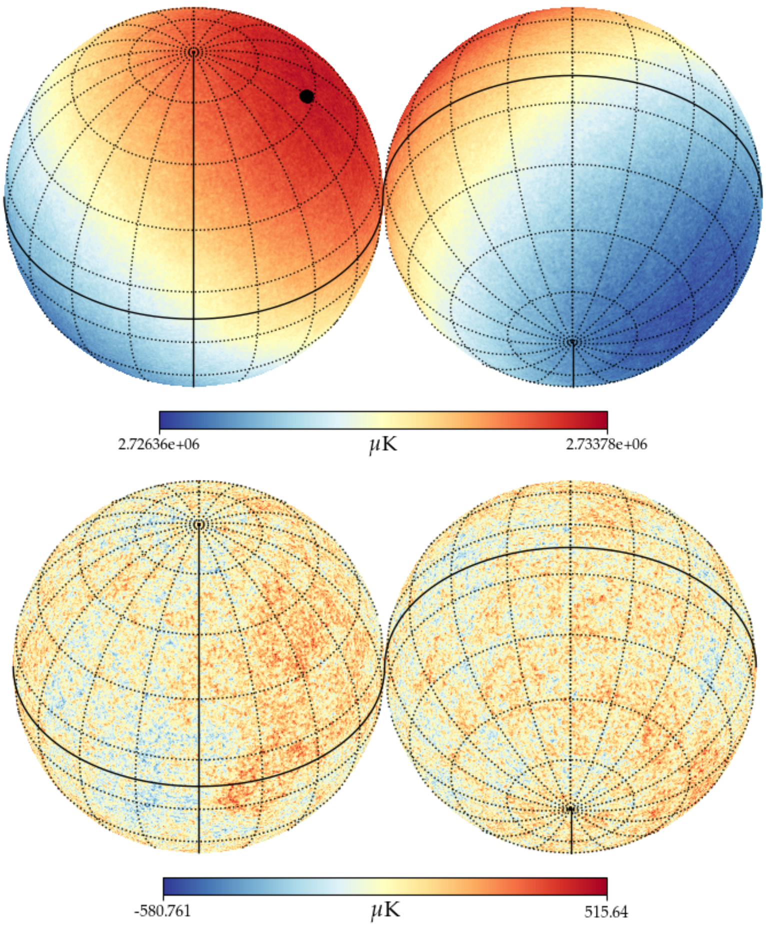

Figure 3.2: CMB sky maps measured by two observers: CMB detected by an observer moving with a velocity of $369\ \mathrm{km\ s^{-1}}$ towards (l,b) = $(264°, 48°)$ (top), against the same CMB anisotropies measured by a comoving observer (bottom). Notice a dipole appearing in large scales as a consequence of the Doppler effect in the direction of motion of the observer.

3.2.1 Relativistic Doppler modulation

According to [11], the Doppler modulation effect is expected to affect all the CMB anisotropies multipoles. The main effect associated to Doppler modulation is to increase the power of the anisotropies in the direction of movement. Figure (3.3) shows the impact of this effect in full-sky synthetic CMB maps for an applied boost of 90% of the speed of light. Doppler modulation is separated from relativistic aberration, by setting no change in photons direction (i.e $\hat{\boldsymbol{n}} = \hat{\boldsymbol{n}}'$ in equation (3.2)), the same figure shows the temperature map measured by a comoving observer (i.e. $\beta = 0$).

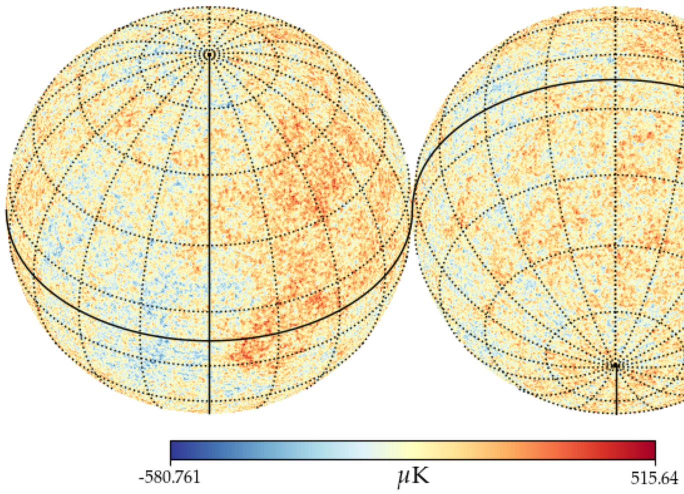

(a) Doppler only ($\beta = 0$)

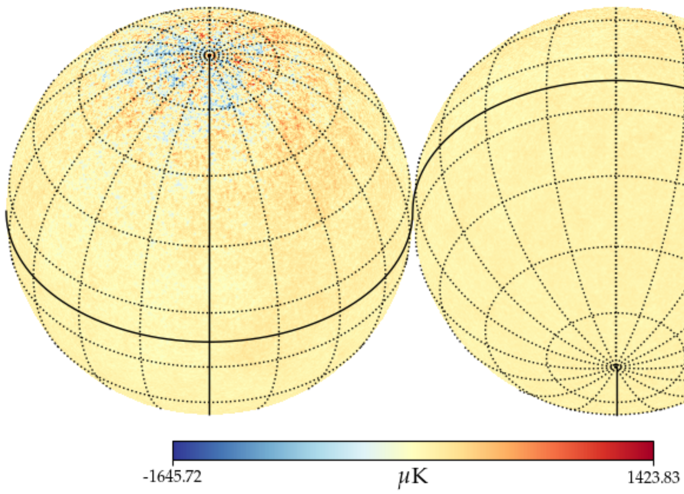

(b) Doppler only ($\beta = 0.9$)

Figure 3.3: CMB anisotropies with Doppler modulation only effects with no boost velocity (top), and an applied boost of 90% of the speed of light (bottom), towards the north pole (l,b) = $(0°, 90°)$ (bottom left). Notice that anisotropies are fixed in position with strong modulation appearing towards the direction of motion of the observer.

According to [13,14], the Doppler modulation is expected to modify the polarization parameters (i.e. $Q(\hat{\boldsymbol{n}})$ and $U(\hat{\boldsymbol{n}})$). In appendix B, you can find a more detailed discussion, based on reference [14], of the transformation properties of all three Stokes parameters I, Q and U relevant for cosmology.

3.2.2 Relativistic aberration

As stated in the previous section, Taylor expansion of equation (3.1) requires an additional assumption on the relative angular shift in the relativistic aberration formula (see equation (3.2)). This approximation states that it is possible to model the aberration deflection angles through an effective weak-lensing-like potential [11,57]. By using this approximation we can write equation (3.2) as follows:

$$\hat{\boldsymbol{n}} = \hat{\boldsymbol{n}}' + \boldsymbol{\nabla}\phi, \tag{3.5}$$

with ϕ as the "lensing potential" for boost effects, which to first order in $\boldsymbol{\beta}$ can be written as:

$$\phi = -\hat{\boldsymbol{n}} \cdot \boldsymbol{\beta}. \tag{3.6}$$

The approximation is justified by the typical deflection angle due to relativistic effects. According to [11], this angle is around $\approx 3'$ comparable with the gravitational lensing effects from the large scale structure from CMB data [57]. Therefore, according to equation (3.6), the effective potential to be used here, when transformed to harmonic space, only has a dipole component.

Notice that this treatment of relativistic aberration is considered a first order approximation and in principle the full aberration potential could have several harmonic multipoles (as the standard large scale weak lensing potential derived from the CMB). However, the approximation fully captures the relativistic aberration effects as it is mentioned in [11,13,58]. As we will present in figure (3.7), relativistic aberration dominates the small scales in the CMB by inducing correlation between mutipoles $\ell, \ell+1$ for angular scales $\ell \geq 400$ (the typical scale expected for weak lensing effects [29]). Its most significant footprint in the anisotropies is inducing a deflection in the direction of the photons and an enhancement of the anisotropies towards the direction of motion of the observer [11]. Figure (3.4) illustrates the effect induced in pixelized CMB anisotropies by having relativistic aberration effects for the case of an applied boost velocity of $\beta = 0.9$, when only equation (3.2) is applied to pixelized CMB maps.

By using the same effective lensing potential, one can model to first order in $\boldsymbol{\beta}$, at least part of the aberration effects that appear into the polarization parameters Q and U. Due to the nature of the polarization parameters, this constitutes an approximation due to the fact the polarization basis is also changing under the boost, however as it is shown in [59], for the large scale gravitational weak lensing, these effects can be neglected at first order.

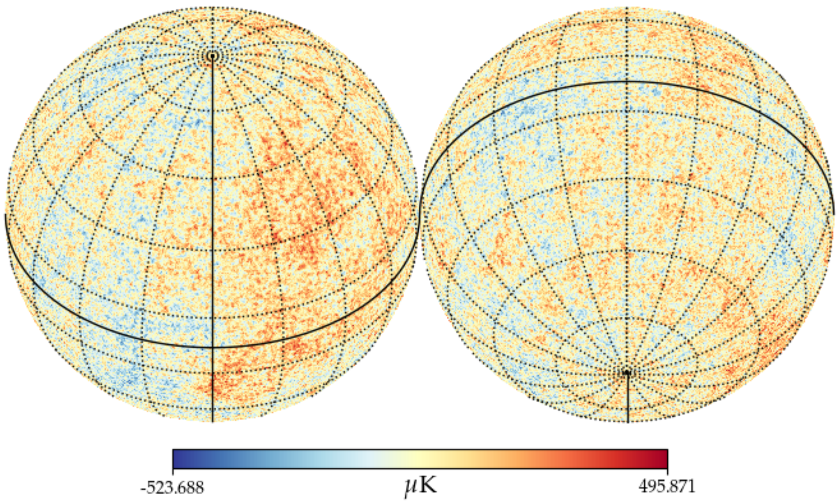

(a) Aberration only ($\beta = 0$)

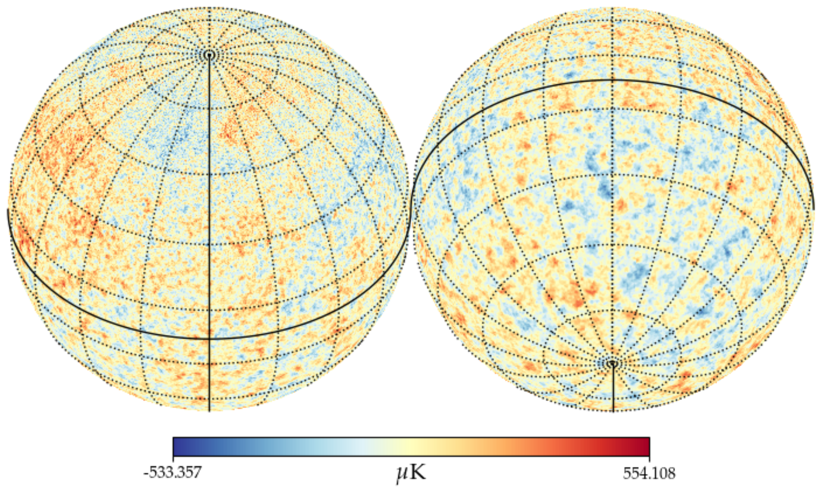

(b) Aberration only ($\beta = 0.9$)

Figure 3.4: CMB anisotropies with aberration only effects with no boost velocity (top), and an applied boost of 90% of the speed of light (bottom), towards the north pole (l,b) = $(0^\circ, 90^\circ)$ (bottom left). Under a Lorentz boost the relative position of the anisotropies changes due to relativistic aberration effects towards the velocity direction (bottom).

3.2.3 The boost cross-correlation function

As it is discussed in [11, 58], boost effects (Doppler modulation and relativistic aberration) induce an effective cross-correlation in nearby multipoles (i.e. ℓ and $\ell + 1$). Within the weak lensing approximation, the cross-correlation can be calculated exactly [14]. This theoretical cross-correlation function is linearly dependent on $\boldsymbol{\beta}$, applied for $\boldsymbol{\beta} << 1$. As [13] shows, this cross-correlation can be used to determine the boost velocity sourcing the correlation for a CMB experiment like *Planck*.

In this section, we show several features of the boost cross-correlation function when Doppler modulation and relativistic aberration are treated separately. Figure (3.5) shows the first-neighbor cross-correlation function for a pure Doppler modulation associated to a boost $\beta = 1.23 \times 10^{-3}$ along the $\hat{z}$ direction and applied directly over a pixelized map (`HEALPix` nside=1024).

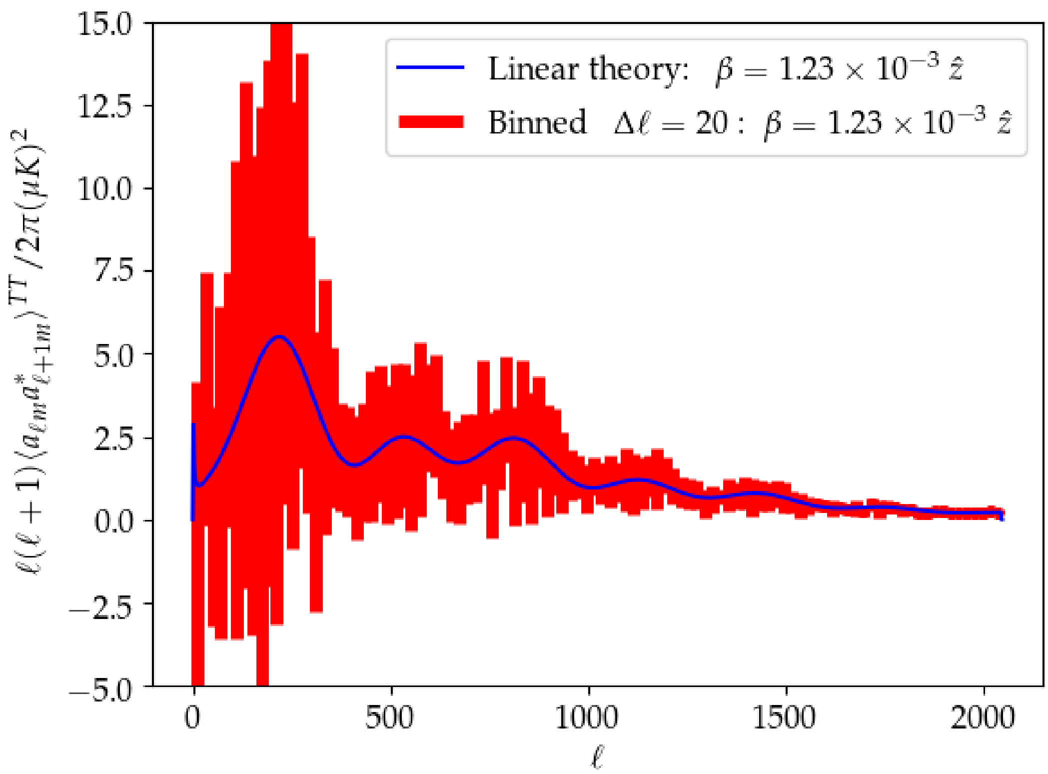

Figure 3.5: Extracted cross-correlation function for an ensemble of 1000 randomly generated full-sky CMB temperature maps containing Doppler modulation only effects with $\beta = 1.23 \times 10^{-3}$ applied in $\hat{z}$ direction (red), against the theoretical prediction from equation (D.37) within the weak lensing approximation (blue). The extracted correlation has been binned with a multipole band of $\Delta\ell = 20$ for visualization purposes.

The red bins shows the cross-correlation obtained directly from the map, after decomposing it into spherical harmonics using `HEALPix` routines. The blue curve is the theoretical model based on the first order calculation of the effect presented in Appendix D. To mitigate the effect of cosmic variance, for each multipole ℓ, the red bins represents an average over 1000 sky map realizations as well as over the $2\ell + 1$ harmonic coefficient $a_{\ell m}$ available, each bin contains an average of the recovered power for a bandwidth of $\Delta\ell = 20$. As can be seen from the plot, Doppler modulation is dominant at large scales (small ℓ's).

On the other hand, it is known that relativistic aberration is a dominant small scale effect [11], with enhanced cross-correlation in the region of higher ℓs. Similar to the case of Doppler modulation, we considered relativistic aberration effect separately, by calculating the shift in the direction of photons following equation (3.2) for a set of 1000 synthetic full-sky CMB maps. Figure (3.6) shows the average over this sample of synthetic full-sky CMB maps for the cross-correlation function $\langle a_{\ell m} a^*_{\ell+1m}\rangle$.

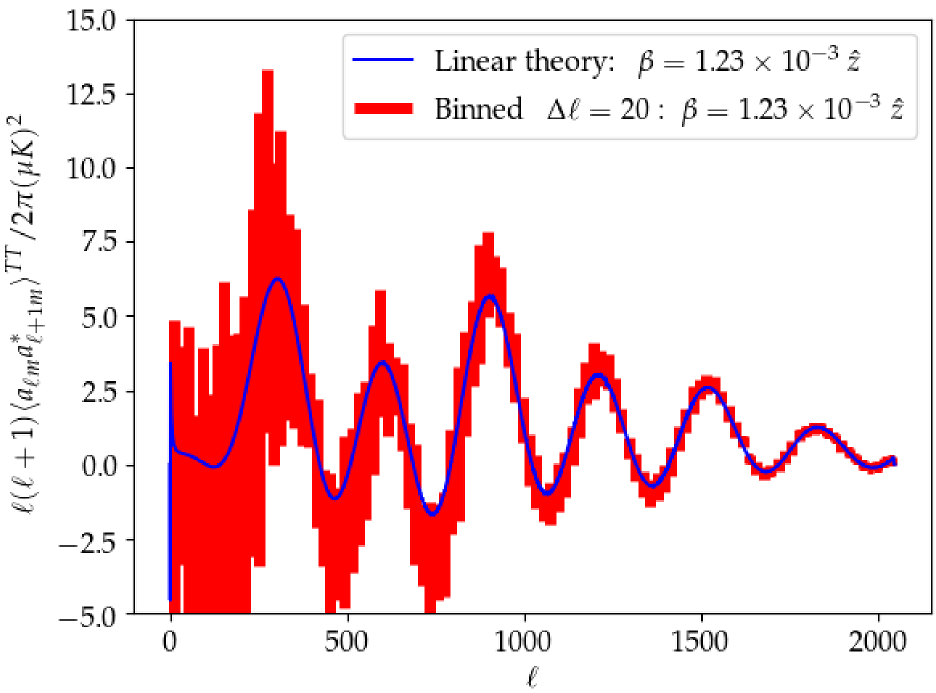

Figure 3.6: Extracted cross-correlation function for an ensemble of 1000 randomly generated full-sky CMB temperature maps containing relativistic aberration only effects with $\beta = 1.23 \times 10^{-3}$ applied in $\hat{z}$ direction (red), against the theoretical prediction derived in Appendix D (see equation D.37) within the weak lensing approximation (blue). The extracted correlation has been binned with a multipole band of $\Delta\ell = 20$ for visualization purposes.

From figure (3.6), we conclude that first neighbor cross-correlation due to relativistic aberration is the dominant boost effect at small scales and it is well described by the weak lensing approximation.

By employing equation (3.4), we show in Appendix D that the expected cross-correlation function, at first order in β, is the sum of the combined Doppler modulation and relativistic aberration correlations. Figure (3.7) shows this calculated combined cross-correlation, again for the averaged over an ensemble of 1000 synthetic full-sky CMB temperature maps generated through the boost of statistically isotropic maps using equation (3.1). By combining both effects, we see that the cross-correlation is dominated by relativistic aberration.

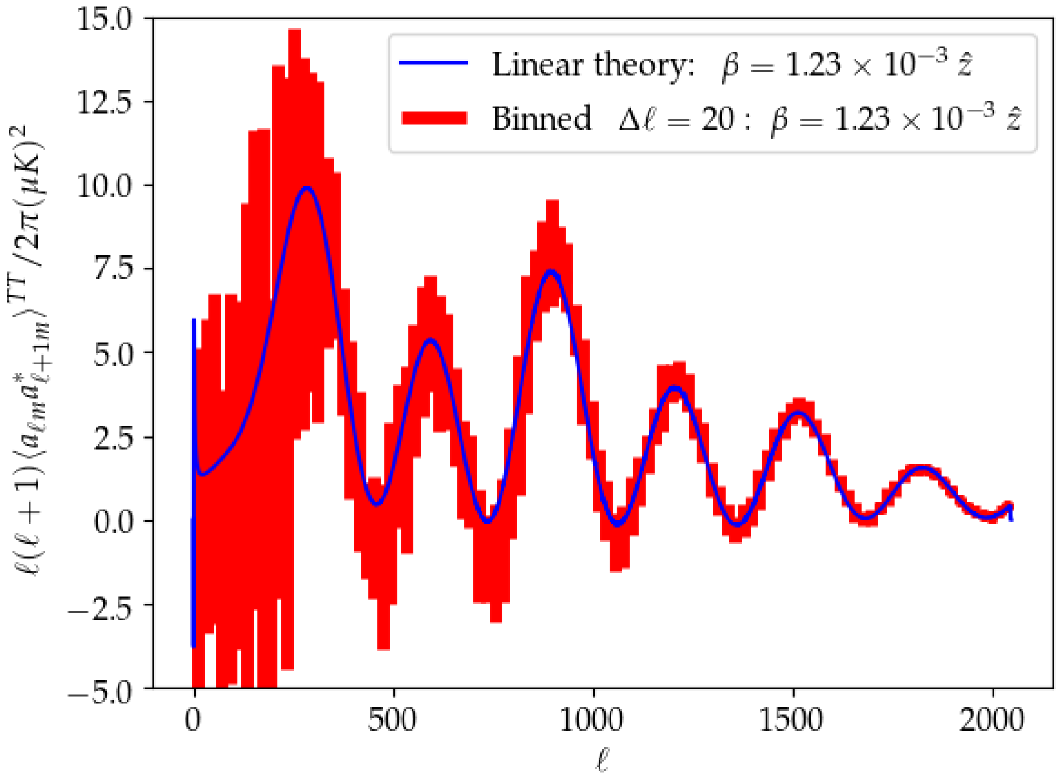

Figure 3.7: Extracted cross-correlation function for an ensemble of 1000 randomly generated full-sky CMB temperature maps containing Doppler modulation and relativistic aberration effects with $\beta = 1.23 \times 10^{-3}$ applied in $\hat{z}$ direction (red), against the theoretical prediction from equation (D.37) within the weak lensing approximation (blue). The extracted correlation has been binned with a multipole band of $\Delta\ell = 20$ for visualization purposes.

In [11] and [14], arguments were shown that the weak lensing approximation would only be valid in the region $\beta\ell \lesssim 1$. We see from figure (3.7), however, that for a boost velocity $\beta = 1.23 \times 10^{-3}$ and $\ell_{max} = 2048$ (i.e. $\beta\ell \lesssim 2.5$), the weak lensing is still a good approximation to model the first neighbor cross-correlation. For the considered case, the calculated cross-correlation function extracted from full-sky synthetic CMB maps using a boost velocity $\beta\hat{\boldsymbol{z}}$, shows little to no impact in the small scale regime (i.e. $\ell_{\max} \geq 1000$) due to second order effects in $\boldsymbol{\beta}$. Additionally, The recent determination of the solar system velocity by the *Planck* collaboration using aberration effects modeled through a weak lensing approximation and $\ell_{max} = 2000$ [11] gives us confidence to use this approximation in chapter 5 to extract β using a maximum likelihood estimator.

3.3 Determination of $\boldsymbol{\beta}$ for *Planck*

As it was discussed in previous sections, the first neighbors cross-correlation induce by boost is the most relevant characteristic of relativistic effects. In [11], the cross-correlation function was shown to be useful to estimate the solar system peculiar velocity. As it is shown by [14], polarization parameters (i.e. $\boldsymbol{Q}(\hat{\boldsymbol{n}})$ and $\boldsymbol{U}(\hat{\boldsymbol{n}})$) are also correlated by relativistic effects, and within the resolution of polarization experiments, these data could be useful for constraining $\boldsymbol{\beta}$ as well. According to [58], this is possible by using current resolution of polarization data from the *Planck* satellite in addition to intensity maps. Figure (3.8) shows the expected signal to noise ratio from an experiment with the resolution of the *Planck* satellite, for both temperature and crossed temperature to polarization data with a partial sky coverage of 85%.

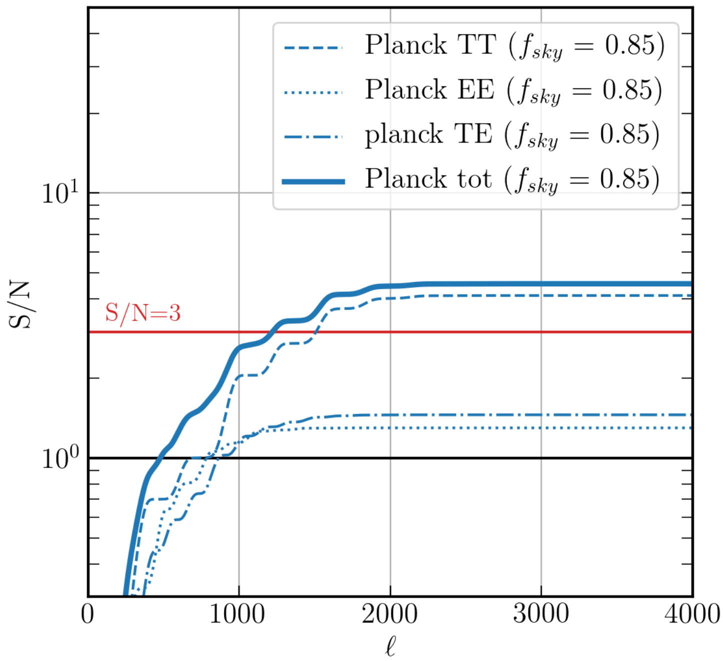

Figure 3.8: Signal to noise ratio for determining $\boldsymbol{\beta}$ as a function of the maximum multipoles for temperature C_ℓ^{TT} and temperature to polarization spectra C_ℓ^{TE}. The result is valid for a telescope with the resolution of the *Planck* satellite.(Extracted from [58]).

Such a determination of $\boldsymbol{\beta}$ was indeed achieved by the *Planck* collaboration in [11] using cross-correlation functions for Intensity maps (I) only. The multipole region used in that work considered an interval $500 \leq \ell \leq 2000$.

3.4 Impact on the CMB power spectra

In this analysis, we have extracted the CMB power spectra for an ensemble of 1000 independently generated full-sky CMB maps with relativistic effects given by equations (3.1, B.6 and B.7). We have chosen three velocities ($\boldsymbol{v} = (0, 369, 3690)\ \mathrm{km\ s^{-1}}$) applied directly over pixelized maps. Figure (3.9) shows the ensemble average of the intensity power spectrum for each of the 3 boost velocities considered (top), as well as the difference of $\beta \neq 0$ cases with respect to the $\beta = 0$ case.

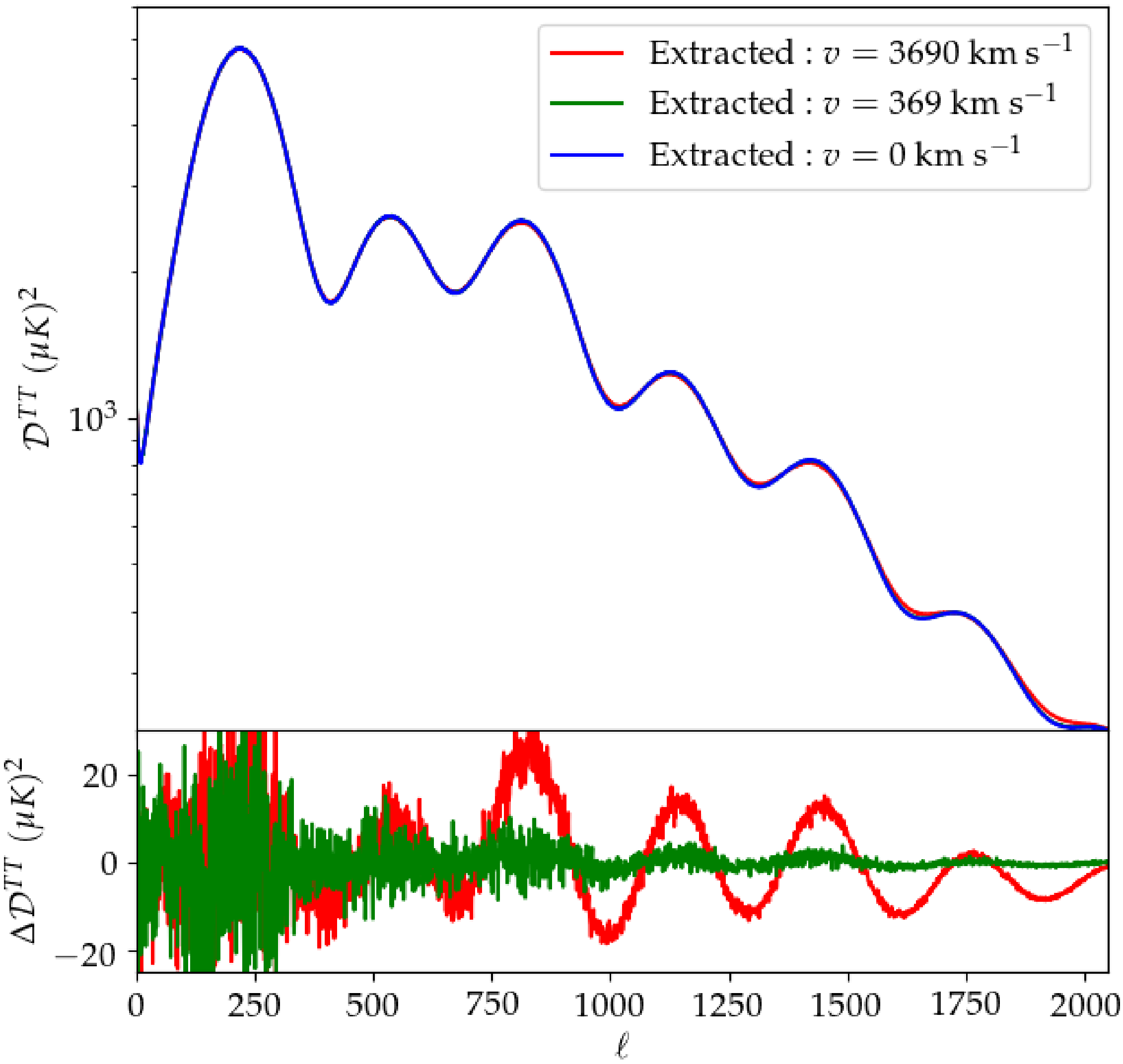

Figure 3.9: Ensemble average of the temperature power spectrum $D_\ell^{TT} = \ell(\ell+1)C_\ell^{TT}$ for each velocity: $\boldsymbol{v} = 0\ \mathrm{km\ s^{-1}}$ (blue), $\boldsymbol{v} = 369\ \mathrm{km\ s^{-1}}$ (green) and $\boldsymbol{v} = 3690\ \mathrm{km\ s^{-1}}$ (red) (top part of the plot). Difference of $\beta \neq 0$ cases with respect to the $\beta = 0$ case (bottom).

An ensemble of 2000 independently generated polarization maps (1000 maps for $\boldsymbol{Q}(\hat{\boldsymbol{n}})$ parameters and 1000 maps for $\boldsymbol{U}(\hat{\boldsymbol{n}})$ parameters) were used to extract the polarization E-modes shown in chapter 2. Figure (3.10) shows the resultant averaged power spectrum C_ℓ^{TE} for each velocity.

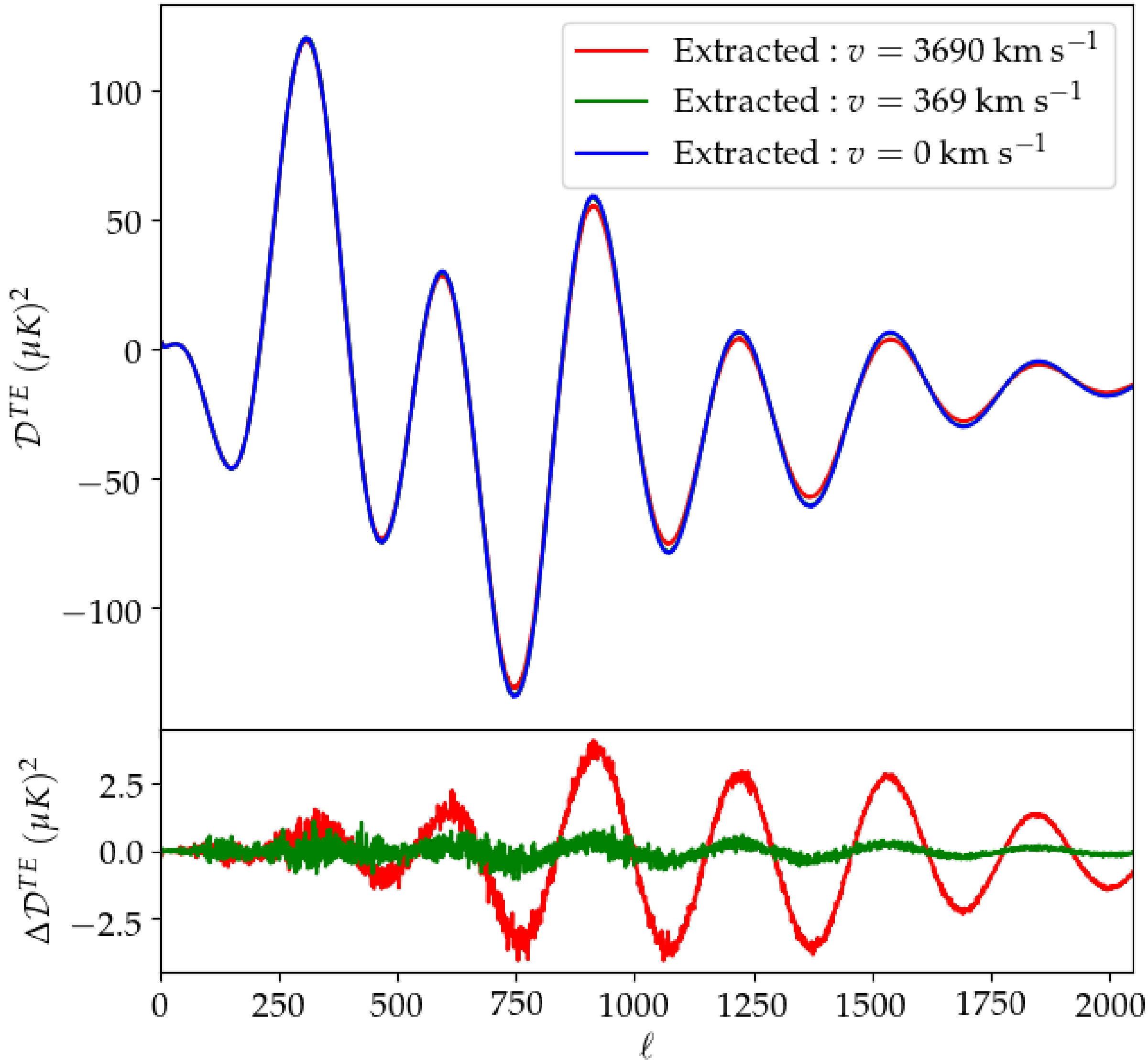

Figure 3.10: Ensemble average of the temperature to polarization power spectrum $D_\ell^{TE} = \ell(\ell+1)C_\ell^{TE}$ for each velocity : $\boldsymbol{v} = 0$ km s^{-1} (blue), $\boldsymbol{v} = 369$ km s^{-1} (green) and $\boldsymbol{v} = 3690$ km s^{-1} (red) (top part of the plot). Difference of $\beta \neq 0$ cases with respect to the $\beta = 0$ case (bottom).

Finally, the C_ℓ^{EE} power spectrum was extracted from the two ensemble of CMB polarization maps (i.e. $\boldsymbol{Q}(\hat{\boldsymbol{n}})$ and $\boldsymbol{U}(\hat{\boldsymbol{n}})$). Figure (3.11) shows the resultant power spectrum for C_ℓ^{EE} for each velocity.

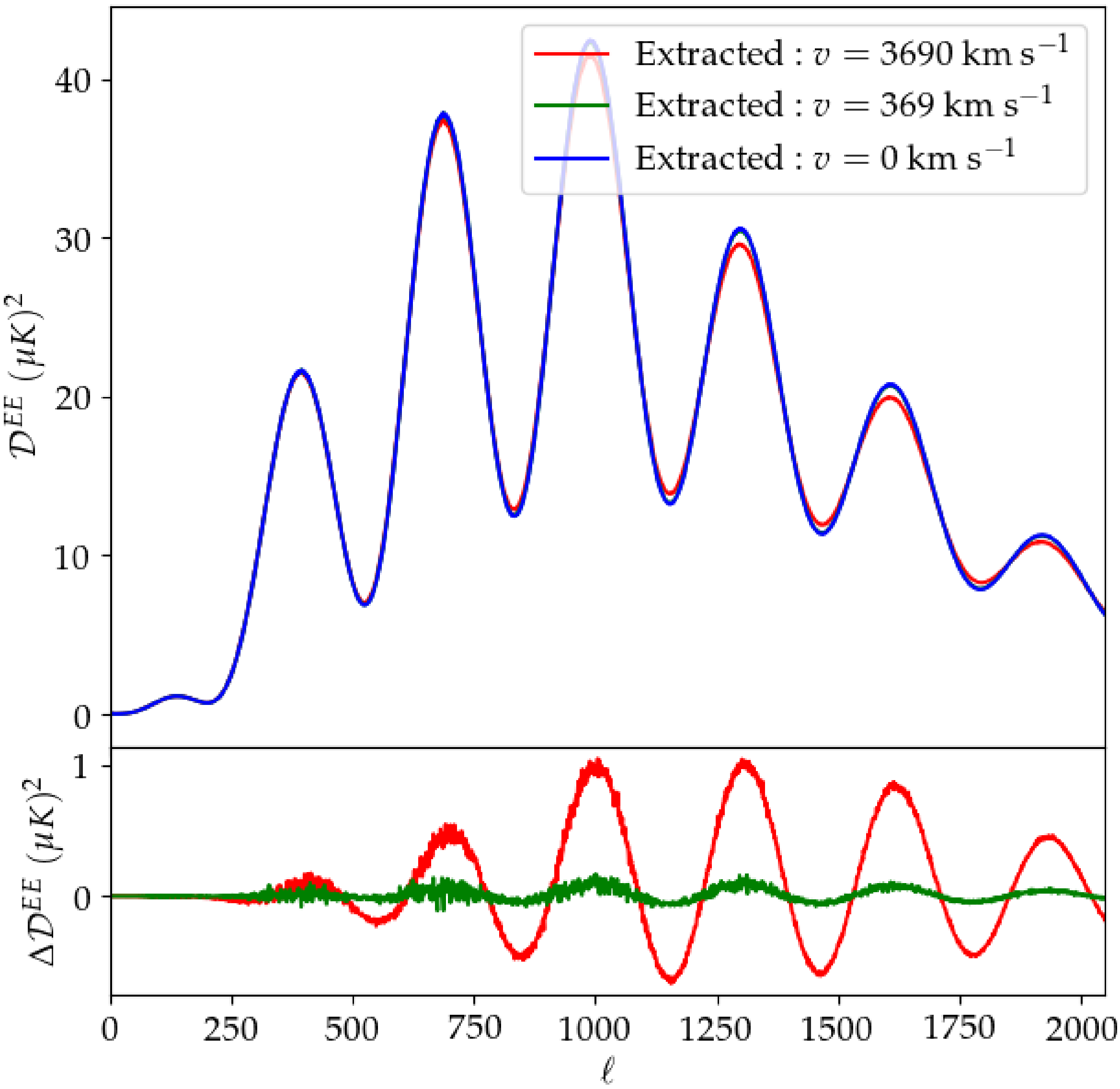

Figure 3.11: Ensemble average of the polarization power spectrum $D_\ell^{EE} = \ell(\ell+1)C_\ell^{EE}$ for each velocity : $\boldsymbol{v} = 0$ km s^{-1} (blue), $\boldsymbol{v} = 369$ km s^{-1} (green) and $\boldsymbol{v} = 3690$ km s^{-1} (red) (top part of the plot). Difference of $\beta \neq 0$ cases with respect to the $\beta = 0$ case (bottom).

3.5 Summary

We have discussed in this chapter the appearance of a cross-correlation function in nearby multipoles $\langle a_{\ell m} a^*_{\ell+1 m}\rangle$. The cross-correlation signal has been extracted using synthetic temperature CMB maps containing Doppler modulation and relativistic aberration effects. For a boost velocity $\beta = 1.23 \times 10^{-3}$, the cross-correlation extracted directly from an ensemble of pixelized maps was shown to be well described by a first order expansion on β together with the weak lensing approximation.

Additionally, we have shown that relativistic effects are present in the CMB power spectra for both temperature and polarization. The simulations showed that the change of frame for a boost $\beta = 1.23\times 10^{-3}$, small perturbations are introduced into the 3 power spectra (C^{TT}, C^{EE} and C^{TE}) with respect to the statistically isotropic case (see figures (3.9), (3.10) and (3.11)). In this analysis we have considered the most idealized situation where relativistic effects were treated alone without any consideration of the observer resolution limitations in measuring the anisotropies.

4 | Impact of boost effects on cosmological parameters

In the previous chapter, we have presented the anisotropies in the CMB temperature associated to the velocity of the observer in the CMB rest frame. Except for the Doppler dipole, these non-primordial anisotropies are difficult to distinguish at the map level, being only evident for higher boosting velocities, but they are, however, still imprinted in the power spectra extracted from sky maps. At first order, the observer motion through the CMB modifies the anisotropies by coupling adjacent multipoles in all scales, breaking the statistical isotropy seen by a comoving observer. Therefore, it is important to check if cosmological parameters estimation based on the hypothesis of statistical isotropy is robust enough when boosting effects are present in the input CMB sky maps. In this chapter, we show that the systematic uncertainty introduced in the determination of cosmological parameters when boost anisotropies are not accounted for is sub-dominant when compared to the statistical one, for solar system velocities $\boldsymbol{\beta} = \boldsymbol{v}_{\odot}/c \simeq 10^{-3}$ in full-sky coverage [60]. In order to do that, we have built an ad-hoc likelihood for the CMB temperature and polarization consistent with the resolution of a satellite like *Planck*. ΛCDM has been taken as the base cosmological model and its parameters were estimated through sampling of the posterior probability distribution using an MCMC (Monte Carlo Markov Chain) sampler.

4.1 Markov Chain Monte Carlo

An MCMC is a Monte Carlo method based in Markov Chains, in order to sample from a given probability distribution, usually applied for integration or calculation of expectation values, by generating points following defined probability distributions. As a traditional example, in order to calculate the expectation value $E[g]$ of a quantity $g(x)$ when x is a random variable, we evaluate:

$$E[g] = \int g(x)p(x)dx, \tag{4.1}$$

where $p(x)$ is the probability distribution function of x. The method works by generating a finite number of points following the $p(x)$ distribution [61]. The expectation value is obtained by evaluating the function in those points:

$$E(g(x)) \approx \frac{1}{N}\sum_{i=1}^{N} g(x_i), \tag{4.2}$$

where x_i are the points generated from $p(x)$. Depending on the particular form of the pdf $p(x)$, the sampling process, especially in the multi-dimensional case, can be difficult as well as inefficient. For those cases, MCMC algorithms are based on sets of points X_t belonging to a Markov Chain whose equilibrium distribution is the desired pdf $p(x)$. In a Markov chain, the probability for transition $X_t \rightarrow X_{t+1}$ can only depend on the previous state of the chain. Such a lack of long-term memory is called the Markov property [61,62]:

$$P_{(X_t \in X|X_0,X_1,\cdots,X_{t-1})} = P_{(X_t \in X|X_{t-1})}, \tag{4.3}$$

notice that as the X_t are generated, the conditional probabilities satisfy:

$$P_{(X_t \in X)} = P_{(X_t \in X|X_{t-1})} \cdots P_{(X_2 \in X|X_1)} P_{(X_1 \in X|X_0)}. \tag{4.4}$$

Indeed, probabilities evolve in time after n iterations of the Markov chain, parameterized by the "time" t of a given update. After a sufficiently large number of steps, the probability distribution should reach an asymptotic form. The existence of this asymptotic distribution can be proved [63] and is crucial for the method to work as a sampling algorithm associated to a given $p(x)$. In order for the equilibrium state to be reached, criteria for accepting or rejecting samples along the chain need to be adopted, like those associated to the Metropolis-Hastings algorithm. It was first used as a method to investigate properties of the equation of state for interacting molecules in spherically symmetric potentials [64] and later generalized by Hasting in 1970 [65].

4.2 Planck's Likelihoods

In principle, cosmological parameters can be estimated by using CMB multipoles in combination with other data sets. The *Planck* Collaboration has developed several codes that organize the measured data facilitating cosmological calculations using these data products. The preprocessed likelihoods use temperature measurements together with polarization maps, separating the power spectra into different regions for different cosmological studies. These likelihoods have the useful characteristic of being easily implemented through the `CosmoMC` code [66]. A detailed discussion of these likelihoods can be found in: [33,67].

In general, there are two groups of likelihoods depending on the interval of multipoles being considered, $\ell = 30$ being the multipole value for separating the large and small scales in CMB sky maps. In the following, we briefly summarize the likelihoods used in the 2018 release [7,33].

- Likelihoods for low multipoles $\ell \leq 29$:
  - `Commander`: This likelihood is based on the CMB sky map[1] called `Commander` that uses a specific component separation technique for map projection and foreground subtraction [68,69].

[1]Several sky maps have been produced by *Planck* collaboration for cosmological studies [7,68,69]

  - `LowTEB`: This is a pixel-based likelihood for the temperature and polarization maps. `Commander` is used as temperature map, whereas for polarization, the 70 GHz map is used and a marginalization over the 30 GHz and 353 GHz maps is performed and taken as tracers for synchrotron and dust emission, respectively [33,69].
  - `LowE`: This likelihood uses polarization multipoles in the range $2 \leq \ell \leq 29$ from the `SimAll` likelihood [70]. It uses the high frequency maps at 100 GHz and 143 GHz, for constraining the optical depth parameter τ, polarization maps at 30 and 353 GHz are used for foreground emission subtraction. [70].

- Likelihoods for high multipoles $\ell \geq 30$:

  - `TT-Plik`: This likelihood uses a combination of CMB sky maps at 100, 143, and 217 GHz, together with the other component separation map called `SMICA` at 353 GHz, and templates of the nuisance parameters associated with galactic dust emission [33,69].
  - `TE-Plik`: It uses combined temperature and polarizations maps between $2 \leq \ell \leq 1996$ multipoles, and averages over the extracted power spectra from CMB maps in the frequencies: 100, 143, 217 GHz [33,69].
  - `EE-Plik`: It uses only polarization maps in the same multipole range and frequency maps as in the `TE-Plik` likelihood.
  - `TT-TE-EE-Plik`: This is a combined likelihood that uses: `TT-Plik`, `TE-Plik`, `EE-Plik` together to sample the parameter space [33,69]. Figure (4.4) shows the best fit for a ΛCDM model based on this likelihood in combination with `LowE` and `lensing`.
  - `TT-PlikLite` and `EE-PlikLite` : These likelihoods are the marginalized version of the `TT-Plik` and `EE-Plik` likelihoods. The marginalization is performed over the nuisance parameters associated with foreground contamination from the galactic plane [68,69].

- Other multipole ranges: $4 \leq \ell \leq 400$:

  - `Lensing`: This likelihood uses lensing signatures in the CMB, deflection in photons path due to inhomogeneities in the universe, by reconstructing the lensing potential from foreground-cleaned `SMICA` maps. The likelihood is used as a consistency check with previous measurements for: σ_8, Ω_m, H_0, obtained from direct measurements of the Hubble constant or galaxy shear surveys [7,67].

Barion Acoustic Oscilations (BAO) provide important constraints on some cosmological parameters. CosmoMC allows for this piece of information to be included in the likelihood, using a combination of data from the 6dF [71] and Sloan Digital Sky

Survey [72] galaxy surveys. Figure (4.1) shows the constraints at 68% and 95% confidence level for the base ΛCDM using some of the mentioned likelihoods.

It is worth mentioning that, even though they are not shown in the plot of figure (4.1), there are extra parameters that are sampled along the MCMC chain. However, we only concentrate in the same parameter space used in [67] to show the reproductibility of their results by using *Planck*'s likelihoods in `CosmoMC`. Table (4.1) shows the best fit values for this set of cosmological parameters by combining four different likelihoods. These results are consistent with those reported in [67] including lensing.

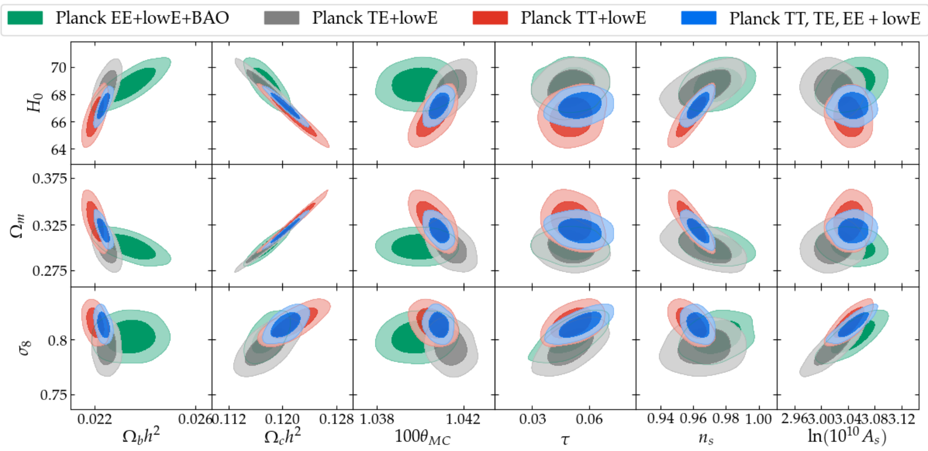

Figure 4.1: Base-ΛCDM parameters at 68% and 95% confidence level. Posterior distributions were calculated using `GetDist` [73] for 4×10^5 samples (Reproduced from [70]).

Parameter	`EE-Plik+lowE+BAO`	`TT-Plik+lowE`	`TE-Plik+lowE`	`TT+TE+EE-Plik+lowE`
$\Omega_b h^2$	0.02343 ± 0.00064	0.02203 ± 0.00022	0.02248 ± 0.00025	0.02236 ± 0.00015
$\Omega_c h^2$	0.1177 ± 0.0014	0.1218 ± 0.0022	0.1177 ± 0.0020	0.1205 ± 0.0014
$100\theta_{MC}$	1.03990 ± 0.00080	1.04060 ± 0.00048	1.04141 ± 0.00049	1.04086 ± 0.00030
τ	$0.0510^{+0.0085}_{-0.0074}$	0.0512 ± 0.0071	0.0501 ± 0.0082	0.0553 ± 0.0074
$\ln(10^{10} A_s)$	3.048 ± 0.022	3.042 ± 0.015	3.018 ± 0.020	3.048 ± 0.015
n_s	0.9748 ± 0.0095	0.9587 ± 0.0058	0.967 ± 0.011	0.9630 ± 0.0044
H_0	68.69 ± 0.83	66.35 ± 0.95	68.44 ± 0.89	67.15 ± 0.62
Ω_m	0.3007 ± 0.0088	0.328 ± 0.014	0.301 ± 0.012	$0.3184^{+0.0082}_{-0.0091}$
σ_8	0.802 ± 0.010	0.8151 ± 0.0089	0.793 ± 0.011	0.8135 ± 0.0074

Table 4.1: Summary of our results for the best fit base ΛCDM parameters by using *Planck* Collaboration likelihoods in `CosmoMC` sampler. Sampled parameters are shown in the upper half of the table in addition to derived parameters in the lower half of the table.

4.3 Ad-hoc likelihood implementation

In this section, we focus on the construction of a likelihood for cosmological parameters inference that is supposed to emulate the properties of some of *Planck*'s likelihoods after marginalization over all nuisance parameters. More precisely, the likelihood will use harmonic space information on the CMB intensity (i.e. TT) and E-mode polarization autocorrelation (i.e. EE), as well as Temperature-E mode cross-correlation (i.e. TE), as input data. The final likelihood should be regarded as the result of marginalization over all *Planck*'s nuisance parameters that are taken into account in the construction of likelihoods as `Plik-Lite`, for example. Such an effective likelihood will later be used for quantifying the systematic uncertainty on cosmological parameters associated to the presence of statistically anisotropic signals in the input sky maps due to boost effects.

4.3.1 The likelihood model

The effective likelihood to be used in the determination of ΛCDM cosmological parameters is given by:

$$-2\ln(\mathcal{L}(\hat{\boldsymbol{D}}|\boldsymbol{D}^{Th})) = (\boldsymbol{D}-\hat{\boldsymbol{D}})^T\boldsymbol{\Sigma}^{-1}(\boldsymbol{D}-\hat{\boldsymbol{D}}), \tag{4.5}$$

where $\boldsymbol{D}$ is a vector containing the theoretical weighted CMB power spectra:

$$D_\ell^{XY} = \ell(\ell+1)C_\ell^{XY}/2\pi, \tag{4.6}$$

computed from `CAMB`, and $\hat{\boldsymbol{D}}$ is the extracted power spectrum from a given sky map realization, $\boldsymbol{\Sigma}$ is the covariance matrix of the model that for this implementation has the form:

$$\boldsymbol{\Sigma} = \mathrm{Diag}(\sigma^2_{\ell_{\min}}, \sigma^2_{\ell_{\min+1}} \cdots, \sigma^2_{\ell_{\max}-1}, \sigma^2_{\ell_{\max}}), \tag{4.7}$$

where σ_ℓ represents the statistical uncertainty in the value of $\hat{D}_\ell$ for *Planck*'s best fit power spectrum for the 2018 data release. The uncertainties are dominated by noise at small scales and by cosmic variance at large scales. They are asymmetric in the low ℓ region ($\ell \lesssim 10$), as can be seen in figure (4.4), following a χ^2 distribution with low number of degrees of freedom. We have symmetrized them when calculating the likelihood (4.5).

Next, we have implemented this custom made likelihood into the CosmoMC code in order to obtain Bayesian estimates for ΛCDM parameters. As input synthetic datasets, we have used the power spectra of full sky maps (i.e. no mask has been applied) generated both with and without boost effects. The main idea here is to show that in this optimal situation, corresponding to a scenario where one has full sky coverage and foregrounds have been fully subtracted, the systematic shifts introduced into the cosmological parameters due to statistically anisotropic boost effects, are already small compared to the statistical uncertainties (these uncertainties correspond to the error propagation from the diagonal covariance matrix of equation (4.7) into the cosmological parameters). The work flow adopted in this part of the analysis is represented in figure (4.2).

The synthetic power spectra were taken as the average over an ensemble of 1000 independent realizations of the CMB sky. It is worth mentioning that even though the synthetic maps were decomposed into spherical harmonics at full sky mode, likelihood (4.5) retains, at least partially, some information on partial sky coverage encoded into the covariance matrix (4.7), since it was obtained from cut sky maps. In addition to that:

- Priors are set to be flat for all the cosmological parameters sampled in `CosmoMC`.
- Temperature and polarization multipole ranges correspond to the ones implemented inside the `TT,TE,EE+lowE+lensing` likelihood: $2 \leq \ell \leq 2500$ for temperature maps, and $2 \leq \ell \leq 1996$ for polarization maps.

This procedure should provide a direct way to probe potential biases on cosmological parameters induced by boost effects when the likelihood used for cosmological parameters estimation does not take into account modulation and aberration effects. The statistical uncertainty, given by the size of the regions in parameter space at a given confidence level will be our ruler to define whether or not the cosmological parameters are biased.

4.3.2 Comparing with *Planck*'s likelihoods

In this section, we make some comparisons between *Planck*'s and our effective likelihood implementation in terms of cosmological parameters in order to guarantee that out implementation is working properly and is consistent with *Planck*'s published results. Table (4.2) contains a dictionary for each of the likelihoods built by using temperature and polarization power spectra.

Likelihood	Nickname in `CosmoMC`
$\mathcal{L}(C_\ell^{TT})$	`TT`
$\mathcal{L}(C_\ell^{TE})$	`TE`
$\mathcal{L}(C_\ell^{EE})$	`EE`
$\mathcal{L}'(C_\ell^{TT}, C_\ell^{TE}, C_\ell^{EE})$	`TT + TE + EE`

Table 4.2: Dictionary of labels for the likelihood sets implemented in `CosmoMC`, the labels are used to distinguish the different power spectrum combinations.

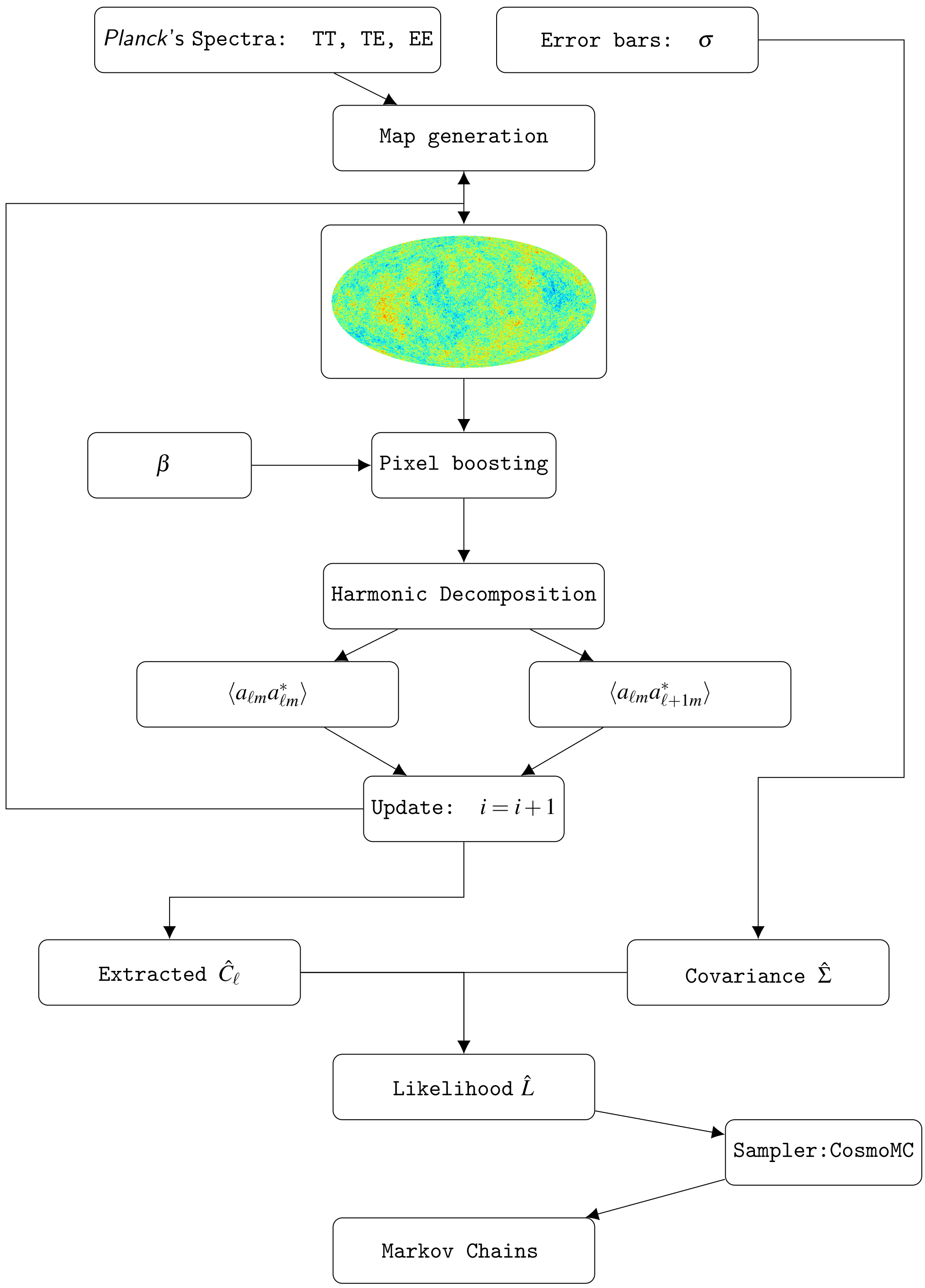

Figure 4.2: Schematic description of the simulation flow: power spectra from *Planck*'s best fit is taken along with the error bars, the spectra are used to generate synthetic maps where a boosting effect (i.e. modulation, Doppler and aberration) are specified with β, this "boosted" map is decomposed into spherical harmonic coefficients to build the correlations functions: $\langle a_{\ell m} a^*_{\ell m} \rangle$, $\langle a_{\ell m} a^*_{\ell+1 m} \rangle$. Iterations in the pipeline to reduce cosmic variance are specified in i.

Figure (4.3) shows the contours at 68% and 95% confidence level for 9 ΛCDM parameters obtained with our effective likelihoods of table (4.2), as well as *Planck* `TT + TE +EE-Plik+lowE` likelihood, the estimated parameters from the posteriors are shown in table (4.3) showing agreement between the likelihoods. One can clearly see the increase in constraining power as the CMB intensity and polarization are combined. One can also see a nice agreement between the contours of the effective likelihood and those coming from the *Planck* implementation.

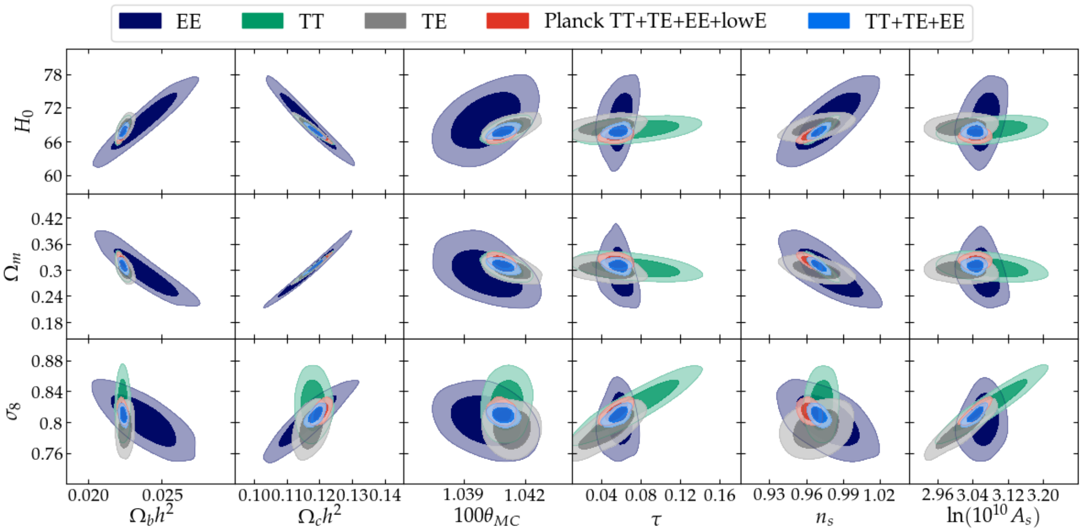

Figure 4.3: Base-ΛCDM parameters at 68% and 95% confidence level showing compatibility in all cosmological parameters for each likelihood combination from Table (4.2). All the likelihood combinations are plotted in addition to `TT+TE+EE-Plik+lowE`.

Parameter	`TT`	`TE`	`EE`	`TT+TE+EE`	`TT+TE+EE-Plik+lowE`
$\Omega_b h^2$	0.02234 ± 0.00022	0.02250 ± 0.00028	0.0238 ± 0.0015	0.02239 ± 0.00015	0.02236 ± 0.00015
$\Omega_c h^2$	0.1181 ± 0.0024	0.1175 ± 0.0024	$0.1164^{+0.0051}_{-0.0061}$	0.1188 ± 0.0014	0.1205 ± 0.0014
$100\theta_{MC}$	1.04110 ± 0.00053	1.04135 ± 0.00061	1.0401 ± 0.0011	1.04094 ± 0.00035	1.04086 ± 0.00030
τ	0.076 ± 0.028	$0.047^{+0.019}_{-0.017}$	$0.0579^{+0.0091}_{-0.0069}$	$0.0571^{+0.0071}_{-0.0051}$	0.0553 ± 0.0074
$\ln(10^{10}A_s)$	3.082 ± 0.053	$3.015^{+0.038}_{-0.034}$	$3.065^{+0.023}_{-0.020}$	$3.046^{+0.014}_{-0.010}$	3.048 ± 0.015
n_s	0.9724 ± 0.0060	0.968 ± 0.012	0.977 ± 0.017	0.9703 ± 0.0040	0.9630 ± 0.0044
H_0	68.1 ± 1.1	68.5 ± 1.1	69.7 ± 3.3	67.80 ± 0.63	67.15 ± 0.62
Ω_m	$0.305^{+0.014}_{-0.015}$	0.300 ± 0.014	$0.293^{+0.029}_{-0.042}$	0.3086 ± 0.0084	$0.3184^{+0.0082}_{-0.0091}$
σ_8	0.823 ± 0.021	0.792 ± 0.016	0.802 ± 0.021	0.8094 ± 0.0065	0.8135 ± 0.0074

Table 4.3: Estimated values for the base-ΛCDM parameters with 1σ errors using the likelihoods in table (4.2) and TT+EE+TE-Plik+lowE from *Planck*. A comparison between the last 2 columns shows a nice agreement between them. Sampled parameters are shown in the upper half of the table in addition to derived parameters in the lower half of the table.

4.4 Impact on the derived cosmology of breaking the statistical isotropy

As shown in the last chapter, in harmonic space, boost effects induce distortions in the spherical harmonics correlations, due to the combined effects of Doppler boost, modulation and aberration. Here we probe the impact of estimating cosmological parameters using a likelihood based on statistical isotropy, when boost effects, like modulation and aberration are present in the input sky maps. Two scenarios will be investigated: (a) the nominal one associated to a boost velocity of magnitude $\boldsymbol{\beta} = 1.23 \times 10^{-3}$, that is, consistent both with the Doppler boost based COBE measurement [8] and the aberration dominated measurement from *Planck* [11]; (b) an extreme scenario where the effects are magnified by applying a factor 10 over the nominal boost velocity. In both cases, the direction of the boost applied over input statistically isotropic synthetic maps (i.e. Monte Carlo) containing the primordial CMB fluctuations is consistent with previous measurements, that is, in galactic coordinates we have:

$$(l_{\text{gal}}, b_{\text{gal}}) = (264^{\circ}, 48^{\circ}). \tag{4.8}$$

In order to probe for potential biases, three sets of power spectra were extracted from the synthetic sky maps: C_ℓ^{TT}, C_ℓ^{TE}, C_ℓ^{EE}. Next, these spectra were used to feed the likelihood shown in equation (4.5) in addition to the error bars from *Planck* collaboration best fit [34]. In our analysis we show the resulting 68% and 95% confidence level 2-dimensional regions for the base-ΛCDM parameter space for each data set extracted from the synthetic maps. Three sets of contours are shown: the statistically isotropic case (i.e. no boost), the nominal case (i.e. $\boldsymbol{\beta} = 1.23 \times 10^{-3}$), and an extreme case (i.e. $\boldsymbol{\beta} = 1.23 \times 10^{-2}$) representing a control sample where we know the bias should be detectable.

In addition to constraining regions, we compute the residuals, for two sets of simulations (i.e. $\boldsymbol{\beta} = 0$ and $\boldsymbol{\beta} = 1.23 \times 10^{-3}$), by using posterior information (i.e. the estimated value and the statistical error derived from the posteriors at 1σ). Therefore, we define the fit residual Δ for each of the 9 parameters of the base-ΛCDM model as :

$$\Delta = \frac{x_{\text{exp}} - x_{\text{true}}}{\sigma_x}, \tag{4.9}$$

where x_{true} is the true value of the parameter as given by `CAMB`, x_{exp} its estimated value and σ_x the corresponding uncertainty. In the absence of biases and assuming Gaussian errors, Δ should follow a normal distribution with zero mean and unit variance.

In addition to the systematic estimation performed by using the residuals, we refer the reader for details of the MCMC chains to Appendix C, where we show the performed statistical tests for separating the burn-in phase from the convergence phase and the auto-correlation length in MCMC samples. The criteria used to establish convergence of the chain is the Gelman-Rubin test [74] to ensure that the posterior distribution is achieving the target probability distribution. In addition to convergence tests, the lag factor for each chain is determined through the auto-correlation function. The lag is the distance between a pair of samples along the chain, so the amount of auto-correlation at a given lag gives us information on how correlated two samples are. Therefore, for statistical analyses, given a pair of samples separated by a given lag whose auto-correlation is at the predefined threshold, one should discard all samples in between.

In the following, we discuss the results obtained from the proposed statistically isotropic likelihood in equation (4.5). Each dataset (`TT`, `EE` and `TE`) is first explored separately, followed by a combined analysis (`TT+EE+TE`).

4.4.1 Temperature

For likelihood sampling inside the `CosmoMC` environment (see Appendix C), we first implemented the temperature likelihood $\mathcal{L}(C_\ell^{TT})$, that uses temperature only power spectrum in its weighted form: $\ell(\ell+1)C_\ell^{TT}/2\pi$. The considered multipole range for building the covariance matrix $\mathbf{\Sigma}$ includes the interval $2 \leq \ell \leq 2508$ from the best-fit *Planck* collaboration power spectrum (See Figure (4.4)).

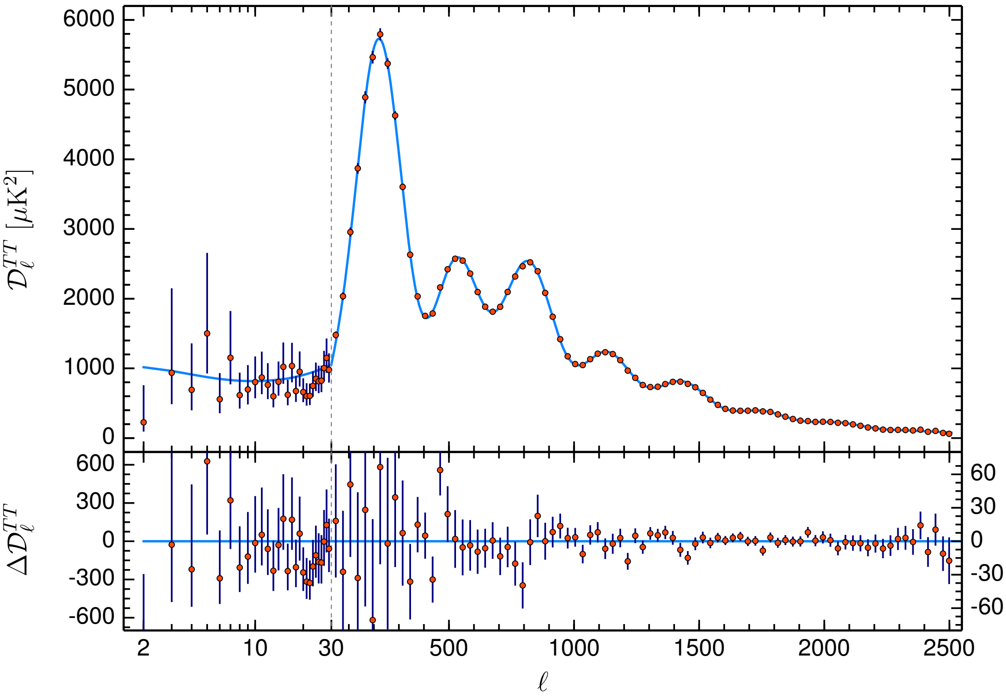

Figure 4.4: *Planck* collaboration best fit power spectrum for the CMB temperature intensity maps using `Plik TT+TE+EE` likelihood (i.e. $\ell(\ell+1)C_\ell^{TT}/2\pi$). The error bars correspond to $\pm 1\sigma$; these error bars contain the statistical error (cosmic variance + noise) inherent to the measurement. (Extracted from: [7]).

After carefully discarding samples within the burn-in phase and correcting the residual auto-correlation of the samples (see Appendix C), base-ΛCDM posterior distributions were obtained by using the effective likelihood method (4.5). Figure (4.5) shows contour regions for the three boost velocities mentioned at the beginning of this section.

From the contours of figure (4.5) the impact of the breaking of statistical isotropy in the input sky maps when $\beta = 1.23 \times 10^{-3}$ for the base-ΛCDM parameters is small compared to the statistical error in the cosmological parameters for a satellite with a resolution on the TT-spectrum similar to *Planck*'s. However, the biases in the $\beta = 0$ and $\beta = 1.23 \times 10^{-3}$ cases are better quantified by using the residuals defined in equation (4.9).

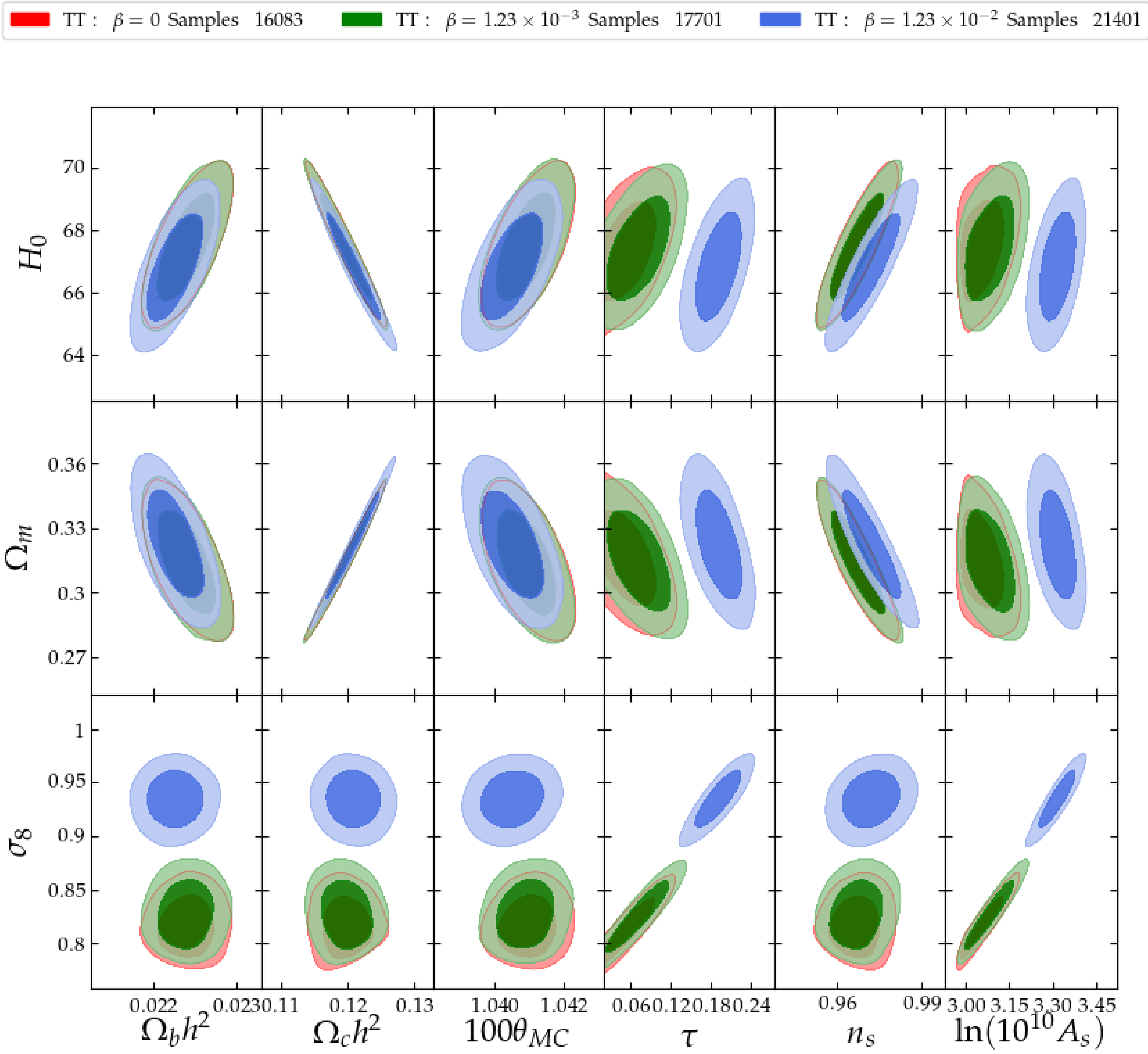

Figure 4.5: Base-ΛCDM parameters at 68% and 95% confidence level from MCMC chains sampled for the likelihood model (4.5) by using the cross-correlation spectrum C_ℓ^{TT}. Null velocity case and the solar dipole one $\boldsymbol{\beta}_{dip}$ are superimposed.

Sampled posteriors are used to estimate the statistical error in measuring the selected ΛCDM parameters. Table (4.4) summarizes the relevant information showing the best fit for each parameter calculated by using the `TT`-only likelihood with its corresponding residual. Additionally, table (4.4) shows these residuals for the $\boldsymbol{\beta} = 0$ and the solar dipole cases. From this table, we notice that for the nominal boost the bias is always sub-dominant with respect to the statistical uncertainty σ ($\Delta < 1$).

Parameter	True value	$\boldsymbol{\beta} = 0$	Δ ($\boldsymbol{\beta} = 0$)	$\boldsymbol{\beta}_{dip}$	Δ ($\boldsymbol{\beta}_{dip}$)
$\Omega_b h^2$	0.02237	0.02241 ± 0.00022	0.16	0.02240 ± 0.00022	0.12
$\Omega_c h^2$	0.1200	0.1198 ± 0.0025	-0.10	0.1198 ± 0.0026	-0.09
$100\theta_{MC}$	1.04092	1.04097 ± 0.00056	0.08	1.04091 ± 0.00056	-0.02
τ	0.0544	$0.062^{+0.017}_{-0.035}$	0.30	$0.075^{+0.027}_{-0.033}$	0.74
$\ln(10^{10} A_s)$	3.044	$3.059^{+0.034}_{-0.063}$	0.35	$3.086^{+0.051}_{-0.060}$	0.39
n_s	0.9649	0.9670 ± 0.0060	0.31	0.9673 ± 0.0063	0.78
H_0	67.36	67.5 ± 1.1	0.12	67.5 ± 1.1	0.09
Ω_m	0.3153	0.314 ± 0.015	-0.09	0.314 ± 0.016	-0.07
σ_8	0.8111	$0.817^{+0.016}_{-0.022}$	0.31	$0.828^{+0.020}_{-0.023}$	0.82

Table 4.4: Summary of the ΛCDM parameters estimated for the temperature TT likelihood for $\beta = 0$ and $\beta = 1.23 \times 10^{-3}$. Sampled parameters are shown in the upper half of the table and derived parameters in the lower half of the table.

4.4.2 Polarization

In this section, we study the bias using the E-mode power spectrum. As for temperature we use its weighted spectrum: $\ell(\ell+1)C_\ell^{EE}/2\pi$. The multipoles considered here go from $\ell = 2$ up to $\ell = 1996$ (see Figure (4.6)).

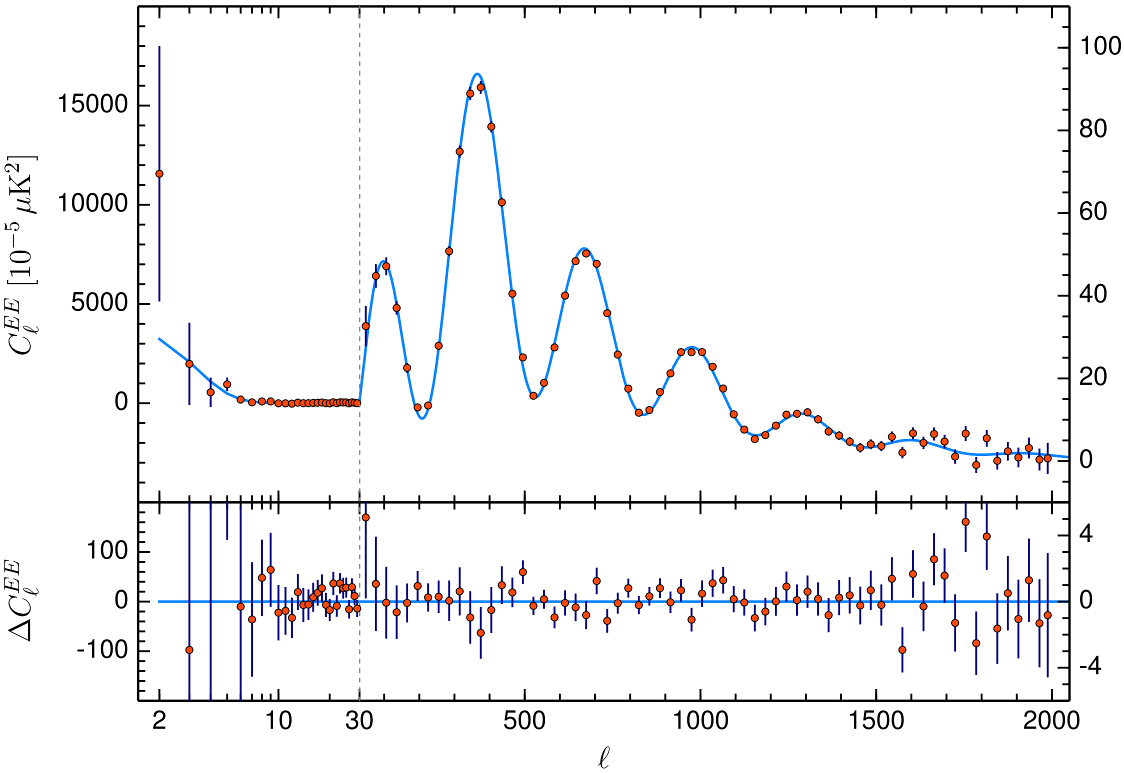

Figure 4.6: *Planck* collaboration best fit E-mode polarization in its un-weighted form (i.e. C_ℓ^{EE}). (Extracted from: [7]).

As in the previous MCMC runs the parameters used for posterior distribution for the base-ΛCDM are the same (i.e. no priors in cosmological parameters, convergence criteria using the Gelman-Rubin test, correlation length of ≈ 20 steps). In this analysis, we use full-sky CMB polarization synthetic maps for the same boosting velocities considered in the temperature only analysis. Figure (4.7) shows the 2-dimensional contours for the ΛCDM parameters.

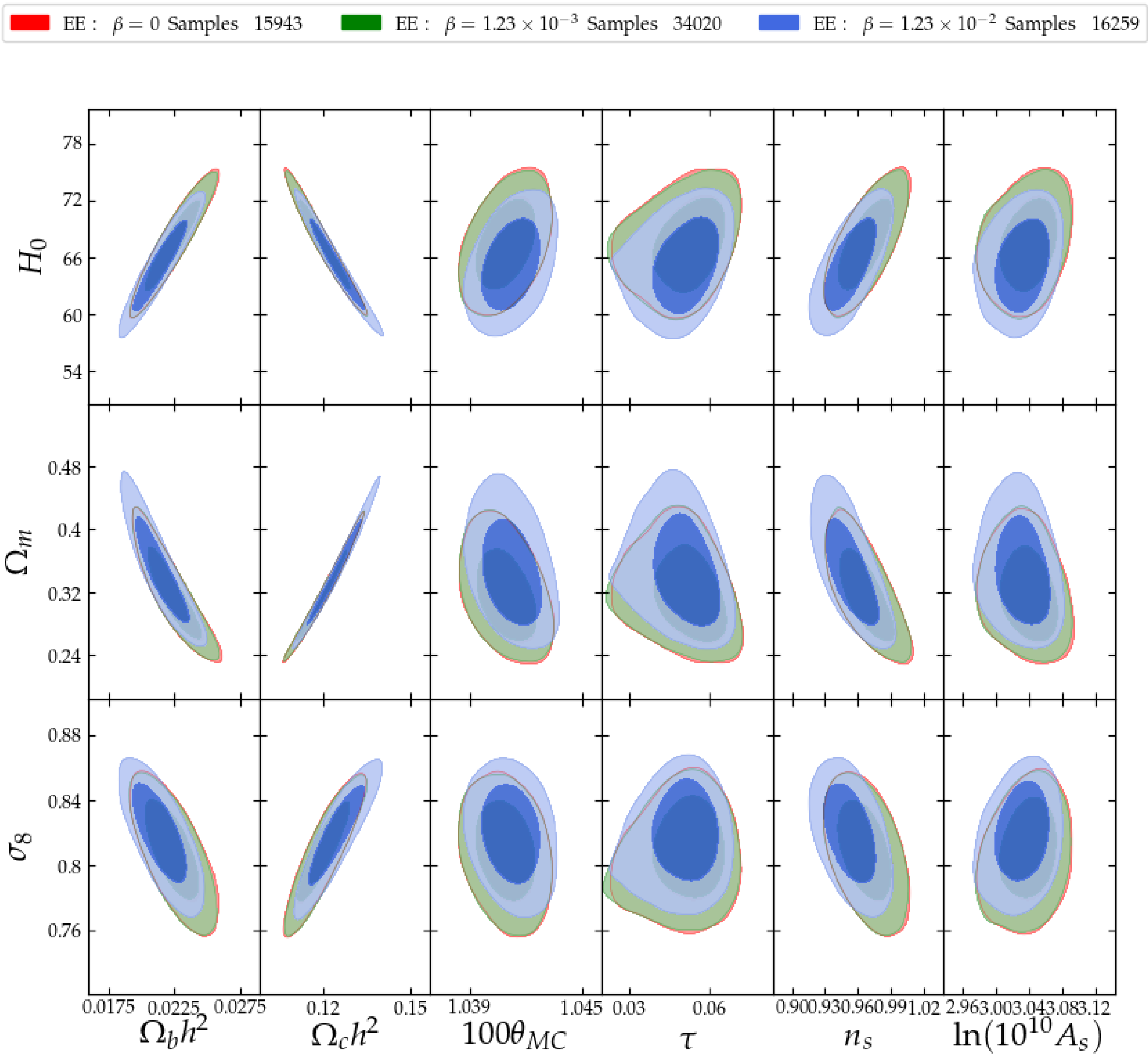

Figure 4.7: Base-ΛCDM parameters at 68% and 95% confidence level from MCMC chains sampled for the likelihood model (4.5) by using the C_ℓ^{EE} power spectrum. Red contours ($\beta = 0$), green ($\beta = 1.23 \times 10^{-3}$, i.e. nominal) and blue ($\beta = 1.23 \times 10^{-2}$, i.e. the extreme case).

Table (4.5) summarizes the results of the fits and also presents the values of the bias Δ for the EE-only case. As in the TT-only case, we see no significant bias in the values of the cosmological parameters introduced by the break of statistical isotropy in the input EE-power spectrum.

Parameter	True value	$\boldsymbol{\beta} = 0$	$\Delta\ (\boldsymbol{\beta} = 0)$	$\boldsymbol{\beta}_{dip}$	$\Delta\ (\boldsymbol{\beta}_{dip})$
$\Omega_b h^2$	0.02237	$0.0225^{+0.0013}_{-0.0014}$	0.06	0.0224 ± 0.0013	0.01
$\Omega_c h^2$	0.1200	0.1201 ± 0.0058	0.01	$0.1203^{+0.0053}_{-0.0060}$	0.06
$100\theta_{MC}$	1.04092	1.0410 ± 0.0010	0.03	1.0409 ± 0.0010	0.03
τ	0.0544	$0.0515^{+0.010}_{-0.0069}$	-0.31	$0.0513^{+0.010}_{-0.0068}$	-0.34
$\ln(10^{10}A_s)$	3.044	$3.039^{+0.025}_{-0.020}$	0.16	$3.038^{+0.025}_{-0.020}$	0.10
n_s	0.9649	0.968 ± 0.016	-0.21	0.966 ± 0.016	-0.26
H_0	67.36	67.5 ± 3.2	0.04	67.3 ± 3.1	-0.01
Ω_m	0.3153	$0.317^{+0.033}_{-0.044}$	0.05	$0.319^{+0.032}_{-0.044}$	0.10
σ_8	0.8111	$0.808^{+0.022}_{-0.019}$	-0.14	$0.809^{+0.021}_{-0.019}$	-0.12

Table 4.5: Summary of the ΛCDM parameters estimated for the EE likelihood from sky maps for non-applied boost velocity $\boldsymbol{\beta} = 0$ and the solar dipole $\boldsymbol{\beta_{dip}}$. Sampled parameters are shown in the upper half of the table in addition to derived parameters in the lower half of the table.

The results obtained from the polarization analysis show a different effect in cosmological parameters in contrast with temperature, obtaining considerably smaller residuals for polarization-only data. Since it is known from chapter (3) that polarization and temperature are differently affected by boosting effects, a cross-correlation between these two synthetic maps represents a consistency check point of the analysis.

4.4.3 Temperature - Polarization

In addition to the temperature- and polarization-only best fit power spectra, *Planck* collaboration provides the cross correlation spectra for the temperature and the electric modes up to multipoles $\ell \leq 1996$, see Figure (4.8). This additional dataset can be used as an independent set for constraining cosmological parameters.

Although these data are not commonly employed separately in cosmological parameters estimation, it is still useful for consistency checks against temperature- and polarization-only cases. Figure (4.9) shows the constraint regions from cross-correlating temperature sky maps with polarization (here only one polarization denoted as E-mode) for the same boosting velocities considered in the temperature-only case.

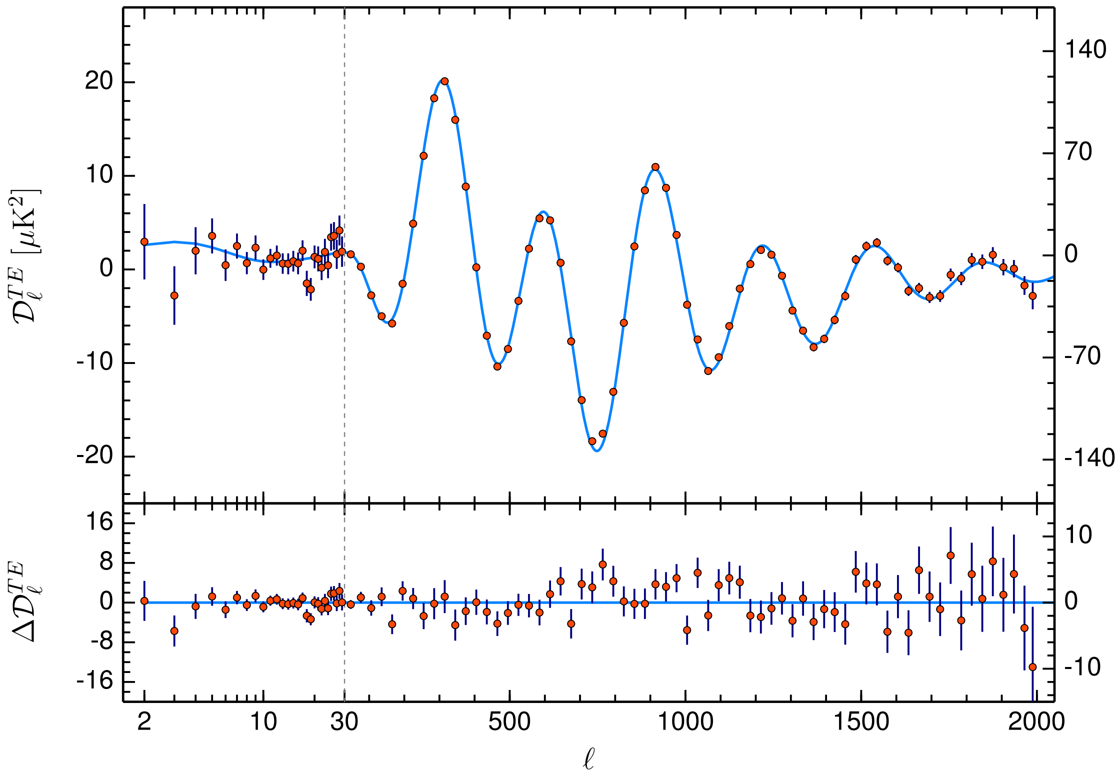

Figure 4.8: *Planck* collaboration best fit power spectrum for the CMB temperature and polarization maps from `Plik TT+TE+EE` likelihood (i.e. $\ell(\ell+1)C_\ell^{TE}/2\pi$). The error bars correspond to $\pm 1\sigma$; these error bars contain the statistical error inherent to the telescope from cross-correlating the polarization with temperature. (Extracted from: [7]).

The most important aspect of the analysis using C_ℓ^{TE} comes from the explicit statistical isotropy breaking that boosting effects induces in this spectrum, where a combination between the Doppler modulation in temperature maps together with boost modulation in polarization (see last chapter) is present in the data.

The specific parameters concerning this MCMC are the same as those considered in the temperature case except for the maximum multipole used in the analysis. As can be seen from figure (4.8), the `TE` multipole range used is $2 \leq \ell \leq 1996$. Table (4.6) quantifies the bias in base-ΛCDM parameters by using multipoles from C_ℓ^{TE}.

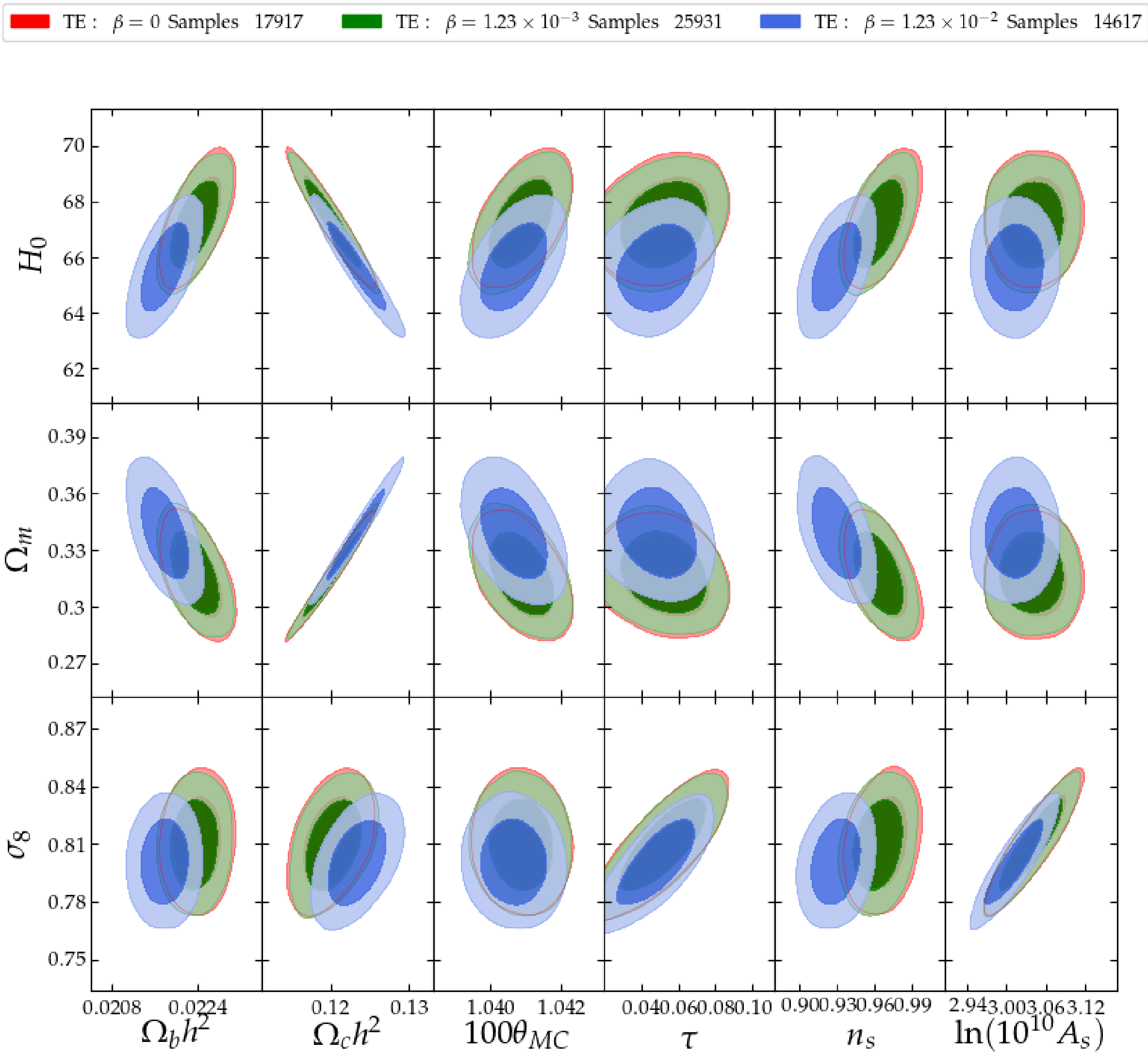

Figure 4.9: Base-ΛCDM parameters at 68% and 95% confidence level from MCMC chains sampled for the likelihood model (4.5) by using only C_ℓ^{TE} power spectrum. Notice the overlapping within the null velocity case and the solar dipole one $\boldsymbol{\beta}_{dip}$.

As in the previous cases (TT and EE), table (4.6) shows a subdominant effect of statistical isotropy breaking by boosting effects and therefore does not introduce significant bias into estimated cosmological parameters.

Parameter	True value	$\boldsymbol{\beta} = 0$	Δ ($\boldsymbol{\beta} = 0$)	$\boldsymbol{\beta}_{dip}$	Δ ($\boldsymbol{\beta}_{dip}$)
$\Omega_b h^2$	0.02237	0.02239 ± 0.00029	0.07	0.02233 ± 0.00029	-0.13
$\Omega_c h^2$	0.1200	0.1200 ± 0.0023	0.02	0.1204 ± 0.0024	0.16
$100\theta_{MC}$	1.04092	1.04090 ± 0.00059	-0.03	1.04088 ± 0.00060	-0.07
τ	0.0544	0.053 ± 0.015	-0.07	0.053 ± 0.014	-0.11
$\ln(10^{10} A_s)$	3.044	3.043 ± 0.032	0.14	3.039 ± 0.031	-0.15
n_s	0.9649	0.967 ± 0.013	-0.04	0.963 ± 0.013	-0.15
H_0	67.36	67.4 ± 1.0	-0.01	67.2 ± 1.0	-0.16
Ω_m	0.3153	0.316 ± 0.014	0.03	0.318 ± 0.015	0.18
σ_8	0.8111	0.811 ± 0.016	-0.01	0.810 ± 0.015	-0.08

Table 4.6: Summary of the ΛCDM parameters estimated for the TE likelihood from sky maps with three multiples of the solar dipole $\boldsymbol{\beta} = 0, \boldsymbol{\beta_{dip}}$. The true value used is the best fit from *Planck* collaboration best fit [70]. Sampled parameters are shown in the upper half of the table in addition to derived parameters in the lower half of the table.

4.4.4 Combined analysis

For improving the constraining power, an additional test using all data information from *Planck* collaboration is performed. Figure (4.10) shows the posteriors by using the likelihood combination TT+TE+EE, with multipoles in the interval $2 \leq \ell \leq 1996$.

We first point out that constraint regions from the full TT+TE+EE analysis in Figure (4.10) clearly differ from the individual data sets analyses. Despite the increase in the constraining power, there is still no statisticaly significant shift for the no-boost and the solar dipole cases. Table (4.7) quantify better this effect by using the residuals for these two cases.

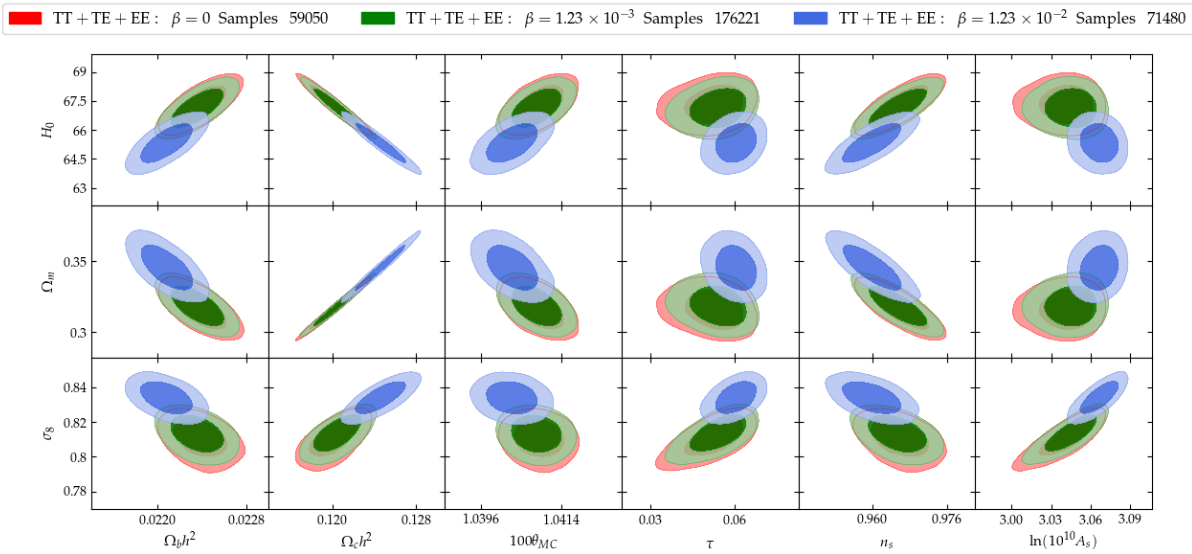

Figure 4.10: 2-Dimensional constrain regions for the base-ΛCDM cosmological parameters, estimated from the likelihood combination `TT+TE+EE`. The CMB data (green contours) compatible with $\boldsymbol{\beta} = \boldsymbol{\beta}_{dip}$ overlaps the no boosting case (red contours).

Parameter	True value	$\boldsymbol{\beta} = 0$	$\Delta\ (\boldsymbol{\beta} = 0)$	$\boldsymbol{\beta}_{dip}$	$\Delta\ (\boldsymbol{\beta}_{dip})$	$10 \times \boldsymbol{\beta}_{dip}$	$\Delta\ (10 \times \boldsymbol{\beta}_{dip})$
$\Omega_b h^2$	0.02237	0.02238 ± 0.00016	0.07	0.02235 ± 0.00015	-0.10	0.02208 ± 0.00015	-1.90
$\Omega_c h^2$	0.1200	0.1202 ± 0.0015	0.11	0.1205 ± 0.0015	0.35	0.1247 ± 0.0015	3.07
$100\theta_{MC}$	1.04092	1.04090 ± 0.00037	-0.04	1.04084 ± 0.00037	-0.22	1.04030 ± 0.00038	-1.62
τ	0.0544	$0.0527^{+0.0078}_{-0.0056}$	-0.24	$0.0536^{+0.0076}_{-0.0053}$	-0.11	$0.0604^{+0.0051}_{-0.0043}$	1.25
$\ln(10^{10}A_s)$	3.044	$3.042^{+0.015}_{-0.011}$	0.27	$3.044^{+0.015}_{-0.011}$	0.13	$3.067^{+0.010}_{-0.0087}$	-1.28
n_s	0.9649	0.9660 ± 0.0040	-0.17	0.9654 ± 0.0041	0.02	0.9597 ± 0.0040	2.39
H_0	67.36	67.31 ± 0.65	-0.08	67.14 ± 0.65	-0.34	65.31 ± 0.65	-3.16
Ω_m	0.3153	0.3162 ± 0.0091	0.10	0.3186 ± 0.0092	0.36	0.346 ± 0.010	3.01
σ_8	0.8111	$0.8108^{+0.0075}_{-0.0066}$	-0.04	0.8130 ± 0.0071	0.27	0.8342 ± 0.0061	3.81

Table 4.7: Summary of the ΛCDM parameters estimated for temperature and polarization spectra by using the combined likelihood `TT+TE+EE`. The spectra are extracted from sky maps with three multiples of the solar dipole β_{dip}: $\boldsymbol{\beta} = 0$, $\boldsymbol{\beta} = \boldsymbol{\beta_{dip}}$, and $\boldsymbol{\beta} = 10 \times \boldsymbol{\beta_{dip}}$. Sampled parameters are shown in the upper half of the table in addition to derived parameters in the lower half of the table.

Figure (4.11) shows also, in addition to the 2-dimensional contour plots, 1-dimensional marginalized distributions in its diagonal for the sampled ΛCDM from the `TT+TE+EE` likelihood combination (H_0, σ_8 and Ω_m are not present because these are derived parameters and to improve the aspect ratio of the plot).

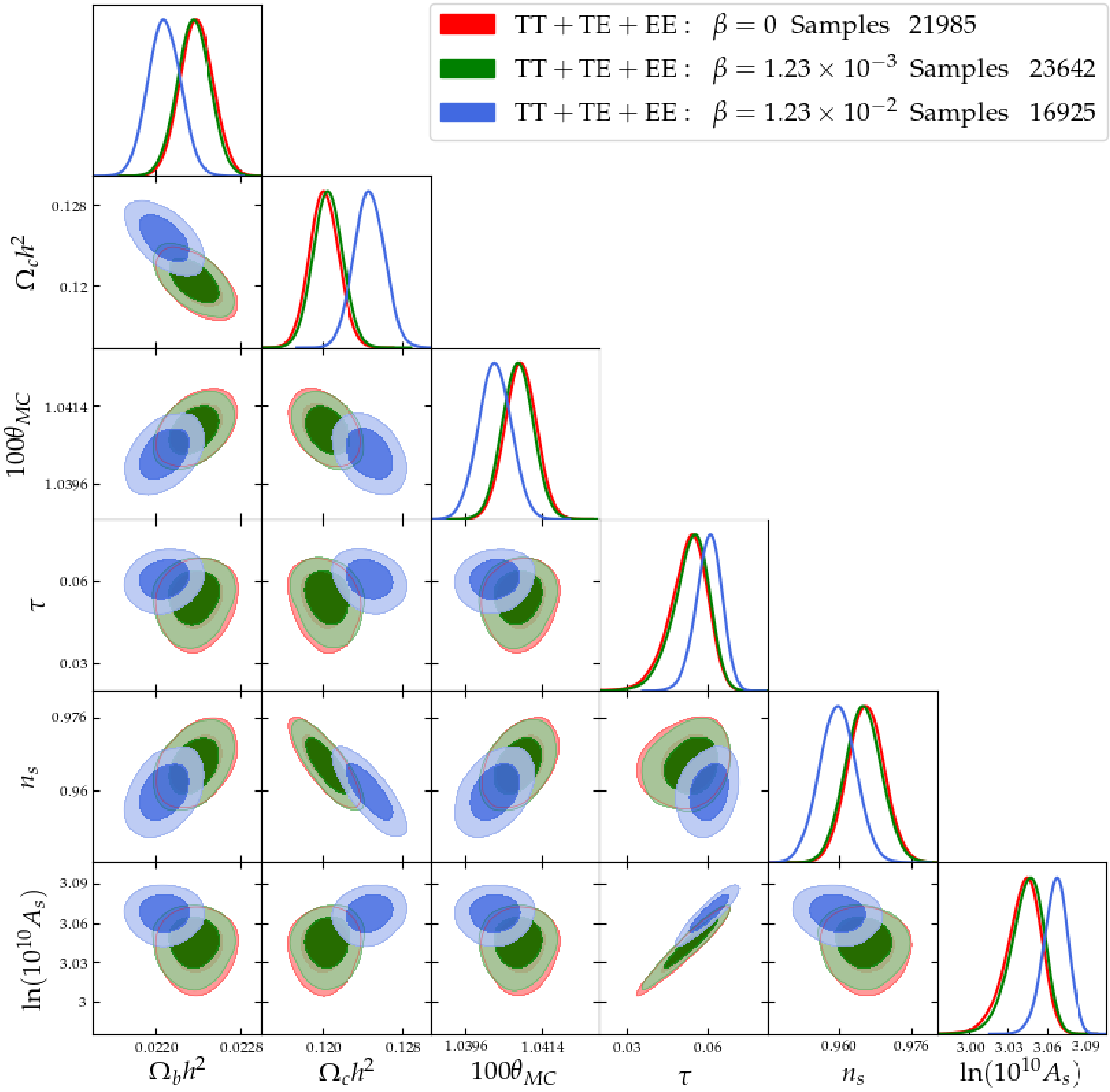

Figure 4.11: Triangle plots extracted from the TT+TE+EE likelihood combination for the base-ΛCDM parameters. The marginal probability distributions are shown in the diagonal part of the plot. The contours contain 68% and 95% confidence level probabilities.

The extreme case of $\beta = 1.23 \times 10^{-2}$ helps us to understand how the bias appear in the cosmological parameters. Table (4.7) shows four parameters (Ω_c, Ω_m, H_0 and σ_8) affected at the 3σ level by the boost. Three of them are derived parameters (Ω_m, H_0 and σ_8). An analysis of the correlation between the fit parameters in figure (4.13) helps us to interpret the origin of the biases on these 3 derived parameters.

The change in the acoustic peaks induced by Doppler modulation (see figure (3.3)) and especially by relativistic aberration (see figure (3.4)) changes the value of Ω_b (at the 2σ level) and Ω_c (at the 3σ level). Due to the strong correlation between Ω_c and Ω_m, this last parameter is shifted at the 3σ level.

In a similar way, the strong correlation between H_0 and Ω_m ends up reducing the Hubble parameter by 3σ. Finally, σ_8 is known to be strongly correlated to Ω_m [75] and such a correlation clearly shows up in figure (4.13) and also explain its almost 4σ bias in table (4.7). For completeness, we also show in figure (4.12) the fit correlations for the nominal case.

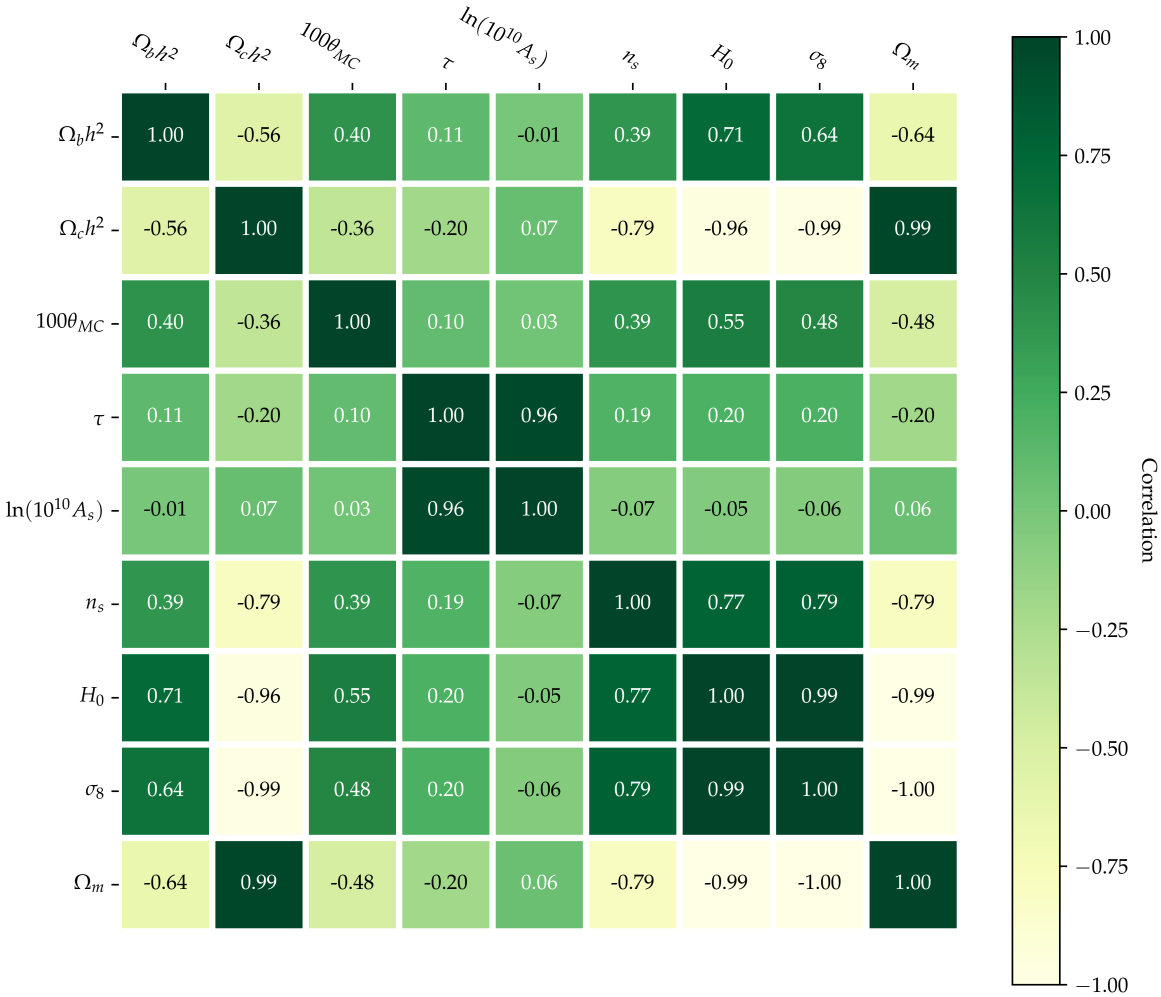

Figure 4.12: Correlation matrix for the base-ΛCDM parameters extracted from the `TT+TE+EE` likelihood combination for the solar dipole case $\boldsymbol{\beta} = \boldsymbol{\beta_{dip}}$.

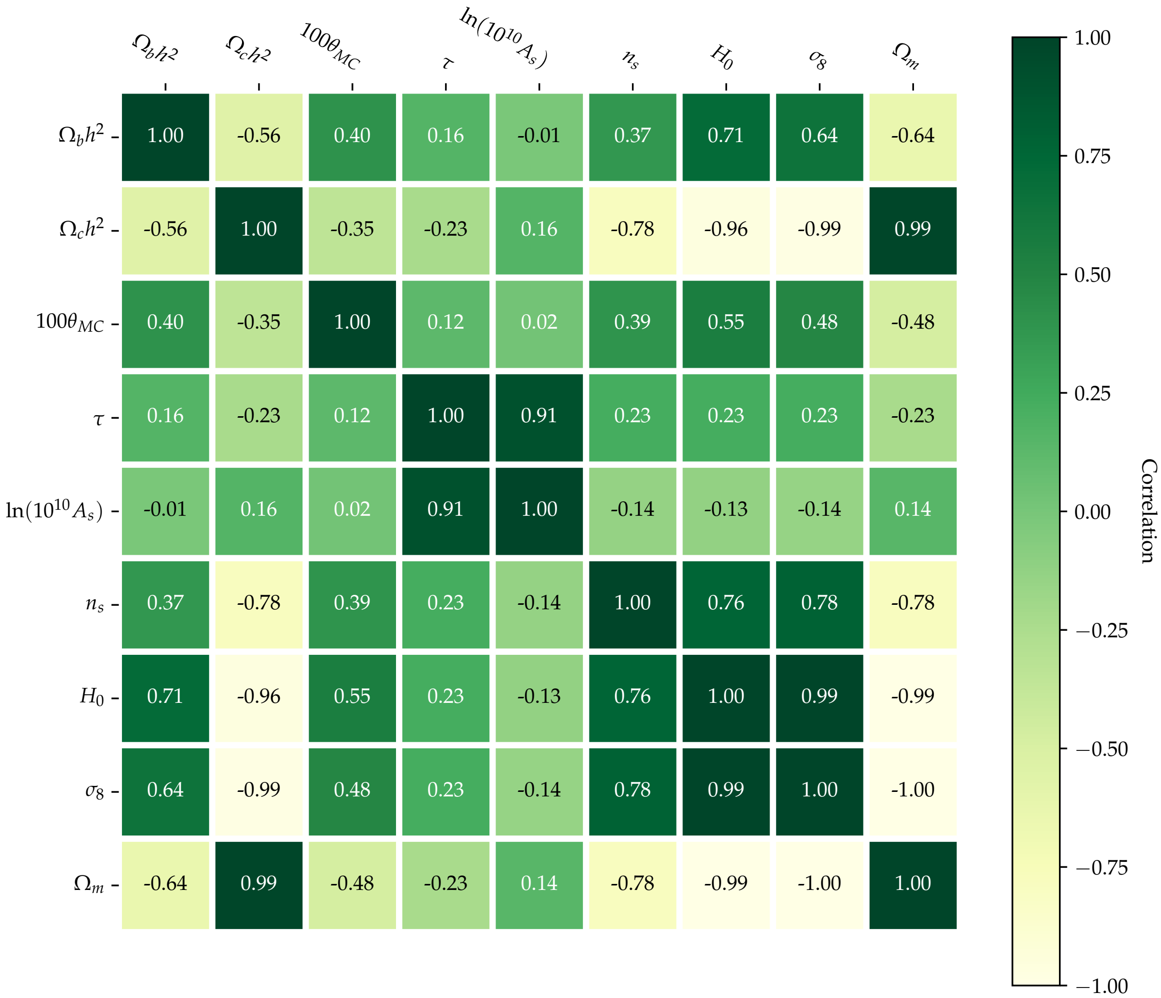

Figure 4.13: Correlation matrix for the base-ΛCDM parameters extracted from the TT+TE+EE likelihood combination for the extreme considered case where $\boldsymbol{\beta} = 10 \times \boldsymbol{\beta_{dip}}$.

As a final check, we have repeated the analysis for $\beta = 1.23 \times 10^{-3}$ using a smaller multipole range ($\ell \geq 30$) where the hypothesis of symmetrical error bars certainly apply for the likelihood of equation (4.5) due to the presence of more degrees of freedom in the probability distribution and the dominance of noise over cosmic variance in this region of the spectrum. As can be seen in table (4.8), the residuals are still fluctuating within the 1σ region and, as already expected, the parameters with the largest values of residuals are τ and n_s. These two parameters depend on information coming from the large scale region of the spectrum ($\ell \leq 30$), where for τ, it is known that large scale polarization anisotropies play an important role for constraining such parameter [7, 34]. On the other hand, the optical depth to the last scattering surface has a strong correlation with the amplitude of scalar perturbations A_s, due to the fact that CMB is sensitive to the combination $A_s e^{-2\tau}$ [7], impacting the A_s parameter.

Parameter	True value	$2 \leq \ell \leq 1996$	$\Delta(2 \leq \ell \leq 1996)$	$30 \leq \ell \leq 1996$	$\Delta(30 \leq \ell \leq 1996)$
$\Omega_b h^2$	0.02237	0.02235 ± 0.00015	-0.10	0.02239 ± 0.00016	0.12
$\Omega_c h^2$	0.1200	0.1205 ± 0.0015	0.35	0.1200 ± 0.0016	0.00
$100\theta_{MC}$	1.04092	1.04084 ± 0.00037	-0.22	1.04090 ± 0.00038	-0.05
τ	0.0544	$0.0536^{+0.0076}_{-0.0053}$	-0.11	$0.076^{+0.025}_{-0.028}$	0.85
$\ln(10^{10}A_s)$	3.044	$3.044^{+0.015}_{-0.011}$	0.26	3.089 ± 0.050	0.38
n_s	0.9649	0.9654 ± 0.0041	0.13	0.9666 ± 0.0045	0.89
H_0	67.36	67.14 ± 0.65	-0.34	67.37 ± 0.72	0.01
Ω_m	0.3153	0.3186 ± 0.0092	0.36	0.3154 ± 0.0099	0.01
σ_8	0.8111	0.8130 ± 0.0071	0.27	$0.830^{+0.019}_{-0.021}$	0.94

Table 4.8: Summary of the ΛCDM parameters sampled for temperature and polarization spectra by using the combined likelihood `TT+TE+EE`. The cosmological parameters are estimated from a boost velocity compatible with solar dipole $\boldsymbol{\beta} = \boldsymbol{\beta_{dip}}$, by using multipole regions between $2 \leq \ell \leq 1996$ and $30 \leq \ell \leq 1996$ for testing the simetrization in error bars at large scales in CMB sky maps. Sampled parameters are shown in the upper half of the table in addition to derived parameters in the lower half of the table.

4.5 Summary

We have shown in this chapter that the systematical uncertainty introduced into cosmological parameters, when their values are estimated using a likelihood based on statistical isotropy, is sub-dominant compared to the statistical one for a satellite like *Planck*. This has been verified in different situations: 3 fits performed using temperature-only (`TT`), polarization-only (`EE`) and temperature-polarization cross-spectrum (`TE`), as well as a combined fit (`TT+EE+TE`). For a boost velocity $\beta = 1.23 \times 10^{-3}$, the typical values of fit residuals Δ defined in equation (4.9) in all four analyses have fluctuated below 1σ (see tables 4.4, 4.5, 4.6 and 4.7).

The resolution of a satellite like *Planck* was incorporated into the likelihood through the error bars of the respective TT, EE and TE spectra measured by these satellite (see figures 4.4, 4.6 and 4.8). A break in the statistical isotropy of the input sky maps from which the power spectra were extracted was introduced by boosting all Stokes parameters (I, Q and U), an operation performed in pixel space. In addition to the nominal scenario ($\beta = 1.23 \times 10^{-3}$), we have also analyzed control samples with $\beta = 1.23 \times 10^{-2}$, where the boost is large enough for its bias to be clearly detectable.

The conclusions drawn are robust, since the inclusion of additional data processing and cleaning like those present in the *Planck* cosmological analysis pipeline (foreground cleaning, marginalization over nuisance parameters, etc) are expected to degrade the resolution σ on the cosmological parameters and, therefore, further decrease the values of Δ. Therefore, we conclude that the breaking of statistical isotropy introduced by boosting effects of order $\beta = 1.23 \times 10^{-3}$ are not significant compared to the current resolution on cosmological parameters achieved by a satellite like *Planck*. This, in turn, allows us to safely fix the parameters of the cosmological model while estimating the boost velocity through modulation and aberration effects introduced in harmonic space. That is the subject of the following chapter.

5 | Reconstructing the peculiar velocity $\boldsymbol{\beta}$

As seen in chapter 3, footprints of the break of CMB statistical isotropy show up with a signal to noise ratio above 3 for $\ell \gtrsim 1000$ when the cross-correlation between neighboring multipoles is analyzed [58]. Measurements of the solar system velocity with respect to the CMB rest frame have been performed since the early 1990's when the *COBE* satellite first made a full sky detection of the dipole induced into CMB temperature, a direct consequence of the Doppler effect. In the last decade, an independent determination of this velocity has been performed by the *Planck* satellite through the aberration effects on the directions of the CMB photons [11], as well as through modulation of the Sunyaev-Zeldovich effect [76]. In this chapter, we extend a maximum likelihood estimator previously employed in the detection of the CMB dipole anomaly [15], by incorporating also aberration effects. We show that such an extended estimator is unbiased and is able to detect both modulation and aberration effects induced by the boost. The resolution of the estimator is determined using full sky synthetic CMB maps.

5.1 A maximum likelihood estimator

We start from equation (3.4) which relates (to first order) the CMB temperature in the two frames of interest in this dissertation. The beginning of this derivation was already performed in section 3.2, but we shall repeat it here by using a slightly different notation to facilitate the comparison with the literature. Written in harmonic space, equation (3.4) takes the form:

$$a_{\ell m} = \int d\hat{\boldsymbol{n}}\Big(T_0 + T_0(\boldsymbol{\beta}\cdot\hat{\boldsymbol{n}}) + \delta T'(\hat{\boldsymbol{n}}) + \delta T'(\hat{\boldsymbol{n}})(\hat{\boldsymbol{n}}\cdot\boldsymbol{\beta}) - \boldsymbol{\nabla}(\boldsymbol{\beta}\cdot\hat{\boldsymbol{n}})\cdot\boldsymbol{\nabla}\delta T'(\hat{\boldsymbol{n}})(\hat{\boldsymbol{n}}\cdot\boldsymbol{\beta})\Big) Y_\ell^{*m}(\boldsymbol{r}), \tag{5.1}$$

where T_0 is the monopole, and $\delta T'(\hat{\boldsymbol{n}})$ are the CMB anisotropies in the comoving frame. The perturbative expansion is separated into five contributions of the form:

$$a_{\ell m}^{\text{Total}} = a_{\ell m}^{\text{Monopole}} + a_{\ell m}^{\text{Dipole}} + a_{\ell m}^{\text{Isotropic}} + a_{\ell m}^{\text{Modulation}} + a_{\ell m}^{\text{Aberration}}, \tag{5.2}$$

For purposes of building a covariance matrix ahead, we shall drop completely the terms identified as "Monopole" and ""Doppler" (of order 10^{-3}), because our final analysis, similar to what is done by *WMAP* and *Planck*, will be performed over maps where the monopole and the dipole induced by Doppler effect over the original monopole have been subtracted. Decomposing the anisotropies $\delta T'(\hat{\boldsymbol{n}})$ into spherical harmonics

$$\delta T'(\hat{\boldsymbol{n}}) = \sum_{\ell=2}^{\ell_{\max}} \sum_{m=-\ell}^{\ell} a_{\ell m}^{\text{Isotropic}} Y_\ell^m(\hat{\boldsymbol{n}}), \tag{5.3}$$

and

$$\hat{\boldsymbol{\beta}} \cdot \hat{\boldsymbol{n}} = \sum_{N=-1}^{1} \beta_{1N} Y_1^N(\hat{\boldsymbol{n}}), \tag{5.4}$$

we have:

$$\begin{aligned} a_{\ell m} = a_{\ell m}^{\text{Isotropic}} &+ \sum_{N=-1}^{1} \beta_{1N} \sum_{\ell' m'} a_{\ell' m'} \int d\hat{\boldsymbol{n}}\; Y_1^N(\hat{\boldsymbol{n}}) Y_{\ell'}^{m'}(\hat{\boldsymbol{n}}) Y_\ell^{m*}(\hat{\boldsymbol{n}}) \\ &- \sum_{N=-1}^{1} \beta_{1N} \sum_{\ell' m'} a_{\ell' m'} \int d\hat{\boldsymbol{n}}\; \boldsymbol{\nabla} Y_1^N(\hat{\boldsymbol{n}}) \cdot \boldsymbol{\nabla} Y_{\ell'}^{m'}(\hat{\boldsymbol{n}}) Y_\ell^{m*}(\hat{\boldsymbol{n}}). \end{aligned} \tag{5.5}$$

Therefore, at first order in β_{1M}, we notice that we can write:

$$\begin{aligned} a_{\ell m} = a_{\ell m}^{\text{Isotropic}} &+ \frac{(-1)^m}{\sqrt{12}} \sum_{N=-1}^{1} (-1)^N \beta_{1N} \sum_{\ell' m'} a_{\ell' m'} \sqrt{(2\ell+1)(2\ell'+1)}\, C_{\ell 0 \ell' 0}^{10} C_{\ell -m \ell' -m'}^{1-N} \\ &- \frac{(-1)^m}{\sqrt{48}} \sum_{N=-1}^{1} (-1)^N \beta_{1N} \sum_{\ell' m'} a_{\ell' m'} [2 + \ell(\ell+1) - \ell'(\ell'+1)] \sqrt{(2\ell+1)(2\ell'+1)}\, C_{\ell 0 \ell' 0}^{10} C_{\ell -m \ell' -m'}^{1-N}, \end{aligned} \tag{5.6}$$

where $C_{\ell -m \ell' -m'}^{1-N}$ and $C_{\ell 0 \ell' 0}^{10}$ are Clebsch-Gordan coefficients. By computing the cross-correlation $\langle a_{\ell_1 m_1} a_{\ell_2 m_2}^* \rangle$, at first order in β_{1N} the covariance matrix is obtained:

$$\begin{aligned} S_{\ell_1 m_1 \ell_2 m_2} = &\; C_{\ell_1} \delta_{\ell_1 \ell_2} \delta_{m_1 m_2} \\ &+ \frac{\Pi_{\ell_1 \ell_2}}{\sqrt{12\pi}} \sum_{N=-1}^{1} (\beta_{1N} C_{\ell_1} (-1)^{\ell_1+\ell_2+1} + \beta_{1N} C_{\ell_2}) C_{\ell_1 0 \ell_2 0}^{10} C_{\ell_1 m_1 \ell_2 m_2}^{1N} \\ &- \frac{\Pi_{\ell_1 \ell_2}}{\sqrt{48\pi}} \sum_{N=-1}^{1} (\beta_{1N} C_{\ell_1} (-1)^{\ell_1+\ell_2+1} + \beta_{1N} C_{\ell_2}) \\ &[2 + \ell_1(\ell_1+1) - \ell_2(\ell_2+1)] C_{\ell_1 0 \ell_2 0}^{10} C_{\ell_1 m_1 \ell_2 m_2}^{1N}, \end{aligned} \tag{5.7}$$

where $\Pi_{\ell\ell'} = \sqrt{(2\ell+1)(2\ell'+1)}$. This expression can be separated into two contributions, a diagonal part setting $\ell_2 = \ell_1$ containing the power spectrum of the anisotropies:

$$S_{\ell_1 m_1 \ell_2 m_2} = C_{\ell_1} \left(1 + \frac{1}{4\pi} \sum_{N=1}^{1} |\beta_{1N}|^2 \right) \delta_{\ell_1 \ell_2} \delta_{m_1 m_2}, \tag{5.8}$$

and an off-diagonal part, containing the first order perturbation in β_{1N}, with $\ell_2 = \ell_1 + 1$:

$$\begin{aligned} S_{\ell m_1 \ell+1 m_2} = &\; (-1)^{m_2} \frac{\Pi_{\ell \ell+1}}{\sqrt{12\pi}} \sum_{N=-1}^{1} \beta_{1N} (C_\ell + C_{\ell+1}) C_{\ell 0 \ell+1 0}^{10} C_{\ell m_1 \ell+1 -m_2}^{1N} \\ &- (-1)^{m_2} \frac{\Pi_{\ell \ell+1}}{\sqrt{48\pi}} \sum_{N=-1}^{1} \beta_{1N} (C_\ell - C_{\ell+1}) [\ell(\ell+1) - (\ell+1)(\ell+2)] C_{\ell 0 \ell+1 0}^{10} C_{\ell m_1 \ell+1 -m_2}^{1N}. \end{aligned} \tag{5.9}$$

From equation (5.7), which is valid for first order in $\boldsymbol{\beta}$, we notice that for $\ell_2 \geq \ell_1+2$ the covariance is identically zero, and there is no mixture for m_1 and m_2 if ℓ_1 and ℓ_2 are equal. However, if $\mathcal{O}(\boldsymbol{\beta}^2)$ corrections are taken into account these correlations are expected to be non-zero. Figure (5.1) shows the structure of this matrix in $m_1 \times m_2$ sub-space where one can see sub-matrices in the form of off-diagonal blocks of dimension $(2\ell+1) \times (2\ell+1)$.

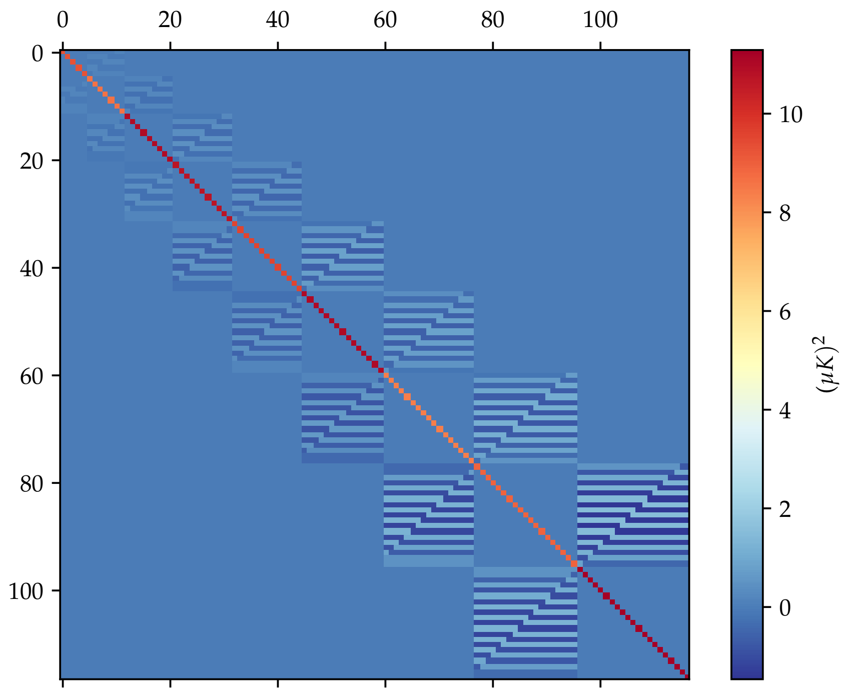

Figure 5.1: Matrix shape for the covariance in equation (5.7) with $\ell_{max} = 10$ with the diagonal and band-shaped matrix contributions, each off-diagonal square corresponds to a given ℓ multipole with a dimension $2\ell + 1$.

As one can see from figure (5.1), the covariance matrix can be divided into a diagonal part $\boldsymbol{D}$ and an off-diagonal matrix $\boldsymbol{O^1}$:

$$S_{\ell_1 m_1 \ell_2 m_2} = \boldsymbol{D}_{\ell_1 m_1 \ell_2 m_2} + \boldsymbol{O^1}_{\ell_1 m_1 \ell_2 m_2}, \tag{5.10}$$

where the superscript (1) denotes the first order contribution of the expansion in β. This splitting in the covariance matrix is performed to match the notation in [15] for the Joint-Bayesian likelihood estimator. In addition, we notice from equation (5.7) that at first order in β this matrix can be further separated into two different contributions containing Doppler modulation and aberrations effects respectively:

$$S_{\ell m_1 \ell+1 m_2} = S^{\rm Mod}_{\ell m_1 \ell+1 m_2} + S^{\rm Aberr}_{\ell m_1 \ell+1 m_2}, \tag{5.11}$$

where the Doppler modulation covariance $S^{\rm Mod}_{l m_1 l+1 m_2}$ is given by:

$$S^{\rm Mod}_{\ell m_1 \ell+1 m_2} = (-1)^{m_2} \frac{\Pi_{\ell\ell+1}}{\sqrt{12\pi}} \sum_{N=-1}^{1} \beta_{1N} (C_\ell + C_{\ell+1}) C^{10}_{\ell 0 \ell+1 0} C^{1N}_{\ell m_1 \ell+1 -m_2}, \tag{5.12}$$

and the aberration covariance $S^{\rm Aberr}_{l m_1 l+1 m_2}$ follows:

$$S^{\rm Aberr}_{\ell m_1 \ell+1 m_2} = -(-1)^{m_2} \frac{\Pi_{\ell\ell+1}}{\sqrt{48\pi}} \sum_{N=-1}^{1} \beta_{1N} (C_\ell - C_{\ell+1}) [\ell(\ell+1) - (\ell+1)(\ell+2)] C^{10}_{\ell 0 \ell+1 0} C^{1N}_{\ell m_1 \ell+1 -m_2}. \tag{5.13}$$

For the construction of a maximum likelihood estimator, we shall work in harmonic space. In that space, the probability to measure a certain CMB sky temperature, represented by a set of harmonic coefficients $\boldsymbol{d}$[1], when the covariance of the primordial signal $\boldsymbol{a}$ is given by $\boldsymbol{S}$ from equation (5.9) and the telescope induces into the measurement a certain amount of noise with covariance $\boldsymbol{N}$, is given by:

$$\mathcal{P}(\boldsymbol{S}, \boldsymbol{a}|\boldsymbol{d}) = \underbrace{\frac{1}{\sqrt{|\boldsymbol{S}|(2\pi)^n}} \exp\left(-\frac{1}{2} \boldsymbol{a}^\dagger \boldsymbol{S}^{-1} \boldsymbol{a}) \right)}_{\text{Primordial fluctuations}} \times \tag{5.14}$$
$$\underbrace{\frac{1}{\sqrt{(2\pi)^n |\boldsymbol{N}|}} \exp\left(-\frac{1}{2} ((\boldsymbol{a}-\boldsymbol{d})^\dagger \boldsymbol{N}^{-1} (\boldsymbol{a}-\boldsymbol{d})) \right)}_{\text{Detector}}.$$

Marginalization over the true primordial signal $\boldsymbol{a}$ allows to combine the primordial covariance matrix $\boldsymbol{S}$ together with $\boldsymbol{N}$ in a compact form:

$$\mathcal{P}(\boldsymbol{S}|\boldsymbol{d}) = \frac{1}{\sqrt{|\boldsymbol{N}+\boldsymbol{S}|(2\pi)^{n/2}}} \exp\left[-\frac{1}{2} \boldsymbol{d}^T (\boldsymbol{S}+\boldsymbol{N})^{-1} \boldsymbol{d} \right]. \tag{5.15}$$

Notice that after this marginalization an effective covariance matrix of the data $\boldsymbol{d}$ that combines the primordial and detector fluctuations appears $\boldsymbol{S}+\boldsymbol{N}$. In order to efficiently evaluate this matrix inversion, a very smart perturbative expansion in β has been derived in [15], by exploiting the diagonal/off-diagonal decomposition of $\boldsymbol{S}$ of equation (5.10). To second order in β, such an expansion lead to [15]:

$$\begin{aligned} - \quad & 2\ln(\mathcal{P}(C_l, \beta_{1N}|\boldsymbol{d})) = n\ln(2\pi) + \ln|\boldsymbol{D}| + \boldsymbol{d}^\dagger \boldsymbol{D}^{-1} \boldsymbol{d} \\ - \quad & \boldsymbol{d}^\dagger \boldsymbol{D}^{-1} \boldsymbol{O}_1 \boldsymbol{D}^{-1} \boldsymbol{d} - \frac{1}{2} \mathrm{Tr}[(\boldsymbol{D}^{-1}\boldsymbol{O}_1)^2] + \boldsymbol{d}^\dagger (\boldsymbol{D}^{-1}\boldsymbol{O}_1)^2 \boldsymbol{D}^{-1} \boldsymbol{d}. \end{aligned} \tag{5.16}$$

[1]The input maps are storaged in an array $\boldsymbol{d}$ with length n.

Here in this analysis, we are interested in testing the accuracy and efficiency of this estimator in synthetic Monte Carlo generated CMB maps with boosting effects. We will not assume any prior information on β_{1N}. Consequently, according to the Bayes theorem, the posterior probability $\mathcal{P}(\boldsymbol{S}|\boldsymbol{d})$ should be proportional to the likelihood $\mathcal{P}(\boldsymbol{d}|\boldsymbol{S})$. Therefore, in the following, we shall use the expressions posterior and likelihood interchangeably. Figure (5.2) shows slices of the likelihood (5.15) obtained from the expansion (5.16) using different covariance matrices: taking into account only modulation effects (see equation 5.12), only aberration effects (see equation 5.13) or the combination of both (see equation 5.11). In this chapter, the cosmological parameters are all fixed, so the likelihood is seen as a function of 3 variables ($n = 3$), corresponding to the 3 components of the boost velocity in harmonic space: $\boldsymbol{\beta}_{10}$, Re($\boldsymbol{\beta}_{10}$) and Im($\boldsymbol{\beta}_{10}$). For figure (5.2), the input CMB sky map was boosted in pixel space using a boost velocity $\beta = 1.23 \times 10^{-3}$ in the direction given by equation (4.8), therefore, it contains both effects: modulation and aberration.

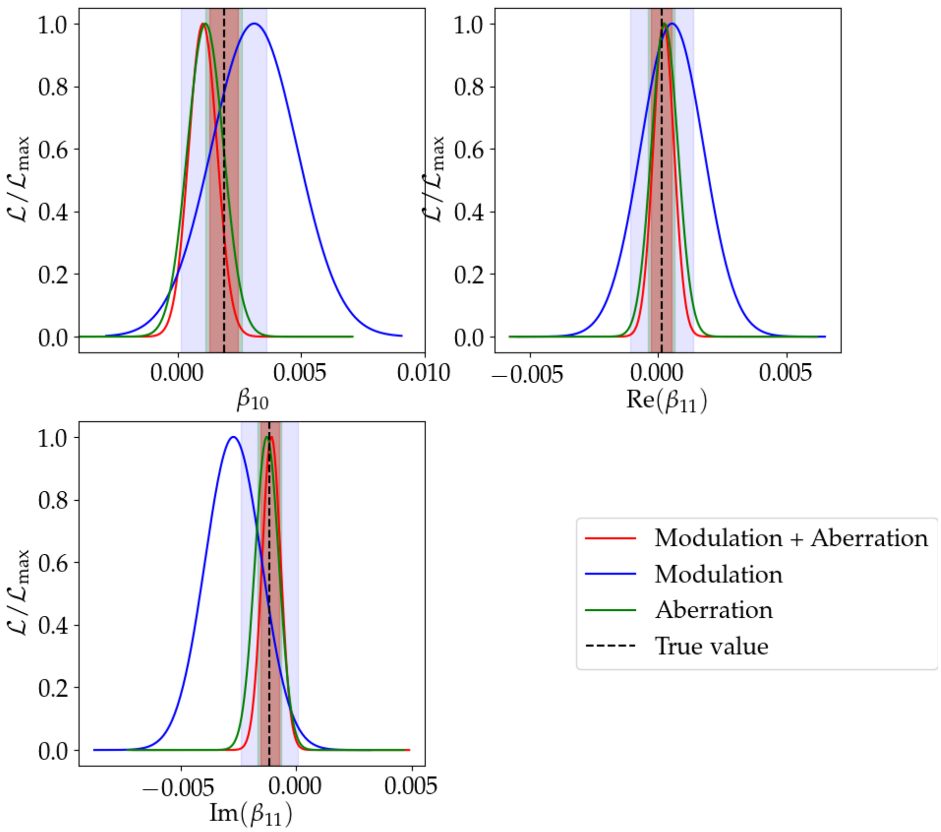

Figure 5.2: Normalized likelihood slices, i.e., the likelihood is conditioned to the values of the two harmonic components of β, while the third value is varied along the x-axis. The CMB input map (with $n_{\mathrm{side}} = 1024$) contains both effects (modulation + aberration), whereas the likelihood is calculated with only modulation effects (blue), only aberration (green) or both effects (red).

The agreement between the true values of β_{1N} and the maximum of the posterior seen in figure (5.2) shows the reliability of the calculated covariance for detecting β_{1M} in the synthetic maps. An additional test to probe for possible systematic effects in the likelihood (5.16) can be seen in figure (5.3), where the full boost case is compared for two input boost velocities different by an order of magnitude: $\beta = 1.23 \times 10^{-3}$ and $\beta = 1.23 \times 10^{-2}$. In both cases, the linear approximation behind equations (5.12) and (5.13) is still valid. The case of $\beta = 1.23 \times 10^{-2}$ is again meant to provide a situation where β_{1N} is sufficiently large to avoid complete overlap with the $\beta = 0$ case.

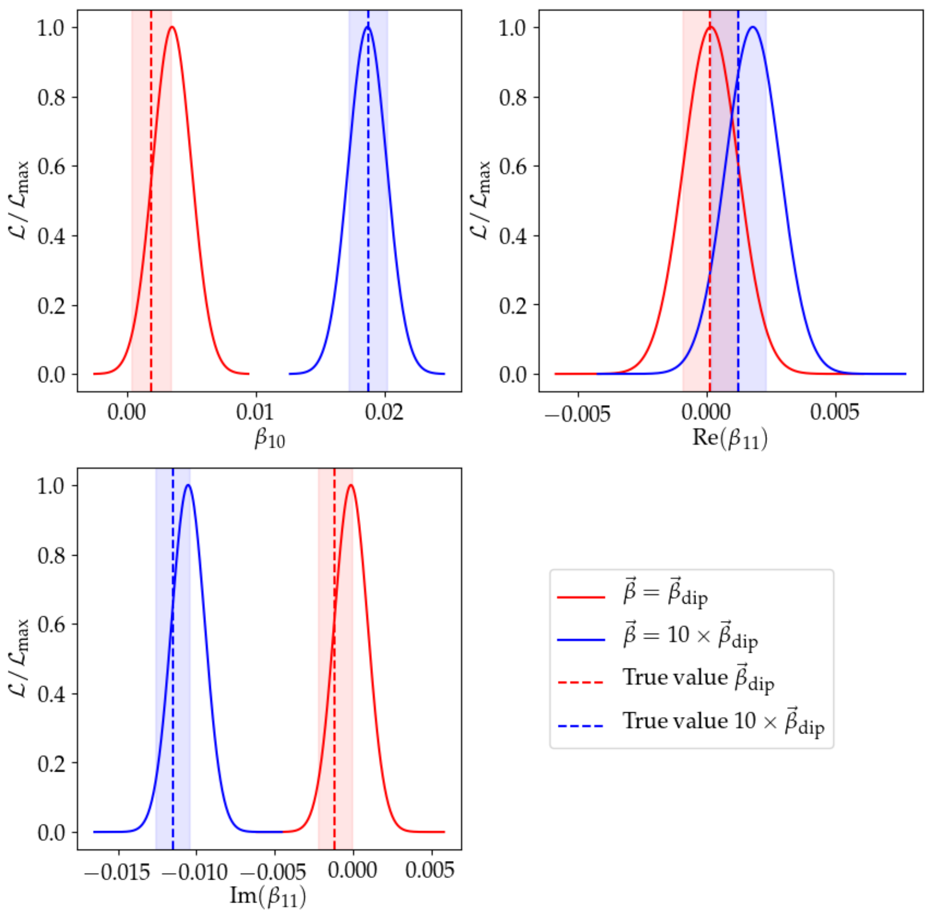

Figure 5.3: Normalized likelihood slices for modulation and aberration effects in full sky CMB map for two different velocities $\boldsymbol{\beta} = 1.23 \times 10^{-2}$ (red) and $\boldsymbol{\beta} = 1.23 \times 10^{-3}$ (blue) at $\ell_{\rm max} = 1024$. Shaded regions show the 1σ confidence interval centered around the fiducial input value (dashed line).

Figure (5.3) shows that the expansion (5.16) combined with the weak lensing approximation for the aberration kernel are still applicable for the case $\beta \sim 10^{-2}$ and $\ell_{\rm max} = 1024$. However, increasing the resolution should allow to test the validity of this approximation. Figure (5.4) shows this test by augmenting the resolution to

$\ell_{\max} = 2048$ for three different boosting velocities: $\boldsymbol{\beta} = \boldsymbol{\beta}_{\text{dip}}, 5 \times \boldsymbol{\beta}_{\text{dip}}, 10 \times \boldsymbol{\beta}_{\text{dip}}$. One can see in this figure the progressive systematic error in β_{1N} coming from ignoring higher order corrections in equation (5.9). Despite the fact that calculating the normalized probability for only one sky realization for $\beta = 1.23 \times 10^{-3}$ is not enough for completely ruling out systematic effects appearing in the likelihood, all the considered additional tests in this section, using independent realizations of full-sky CMB synthetic maps, points towards the same interpretation as the one given in figures (5.3), and (5.4).

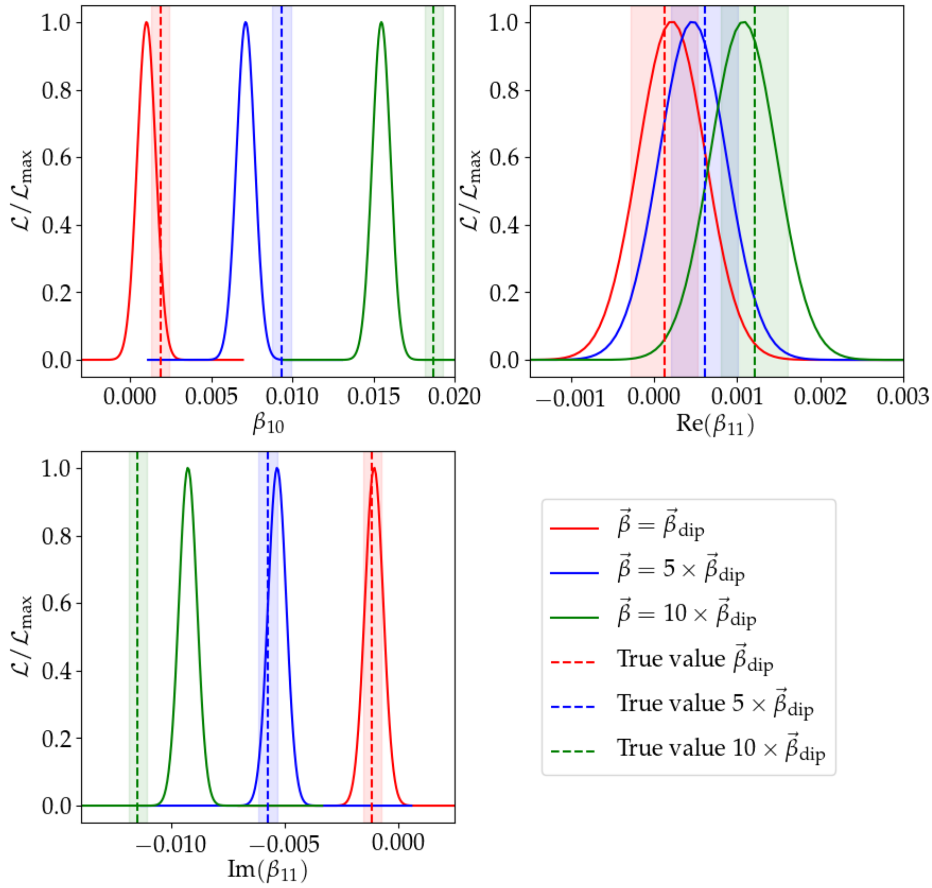

Figure 5.4: Normalized likelihood slices for three different input velocities $\beta = (\boldsymbol{\beta}_{\text{dip}}, 5 \times \boldsymbol{\beta}_{\text{dip}}, 10 \times \boldsymbol{\beta}_{\text{dip}})$ at $\ell_{\max} = 2048$ resolution. Shaded regions show the 1σ confidence interval centered around the fiducial input value (dashed line).

As one can see from figure (5.2), the aberration effect dominates at small scales (large ℓ), so the inclusion of multipoles at large ℓ values should improve the resolution of the likelihood (5.16). Figure (5.5) clearly shows this reduction of the full boost conditioned likelihood width for increasing $\ell_{\max} = 512, 1024, 2048$.

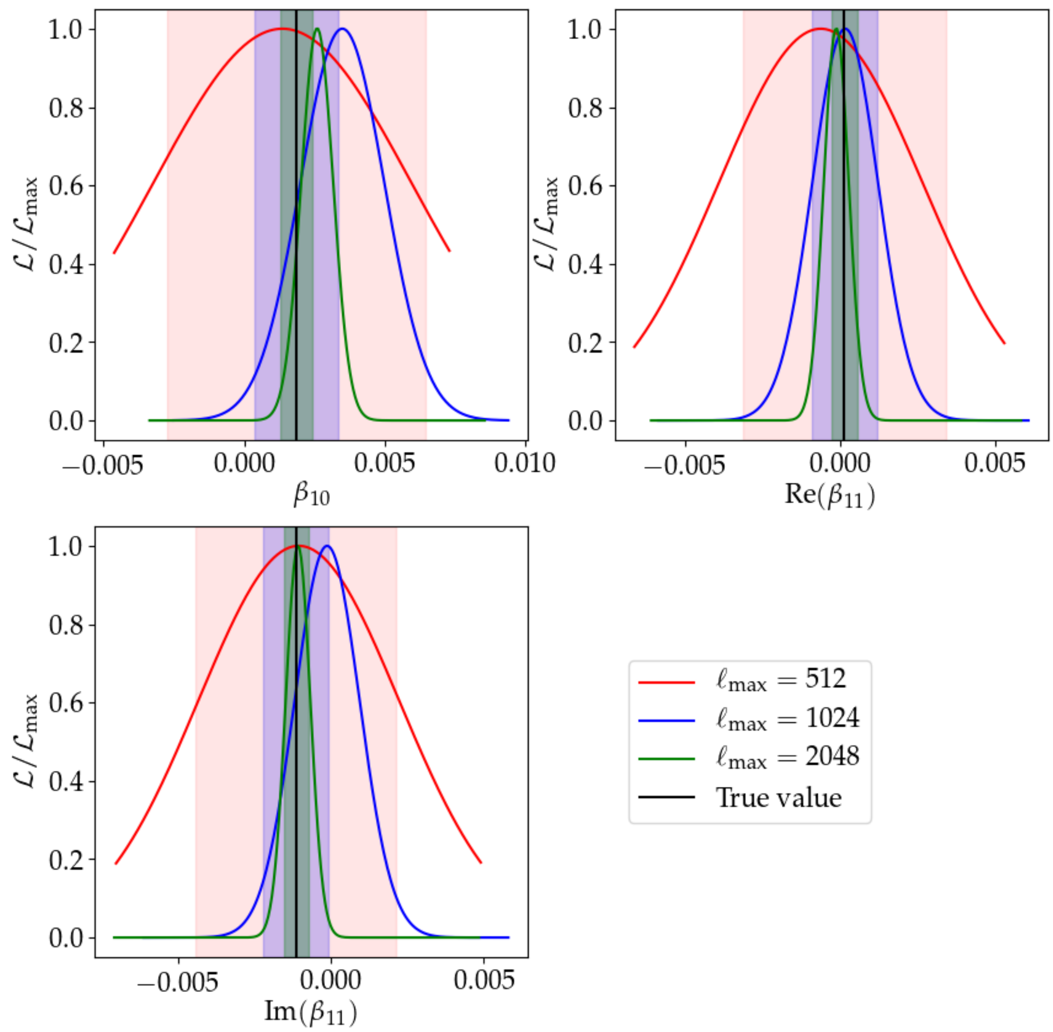

Figure 5.5: Normalized likelihood slices for full boosting likelihood using full sky CMB maps for three different maximum multipole ℓ_{max} used inside $\boldsymbol{S}$. Shaded regions (blue, green and red) show the corresponding 1σ interval for each case centered at the true input value in Monte Carlo simulations (dashed line).

A final plot useful for understanding the statistical power contained in different multipole ranges can be seen in figure (5.6). In this plot, the likelihood has been calculated using non-overlapping multipole ranges $0 \leq \ell \leq 1024$ and $1024 \leq \ell \leq 2048$. As one can see, the resolution of the maximum likelihood estimator presented here is dominated by higher multipoles due, of course, to the combination of the rapid increase in their number $\propto \ell_{\rm max}^2$ and the presence of aberration signal at small scales.

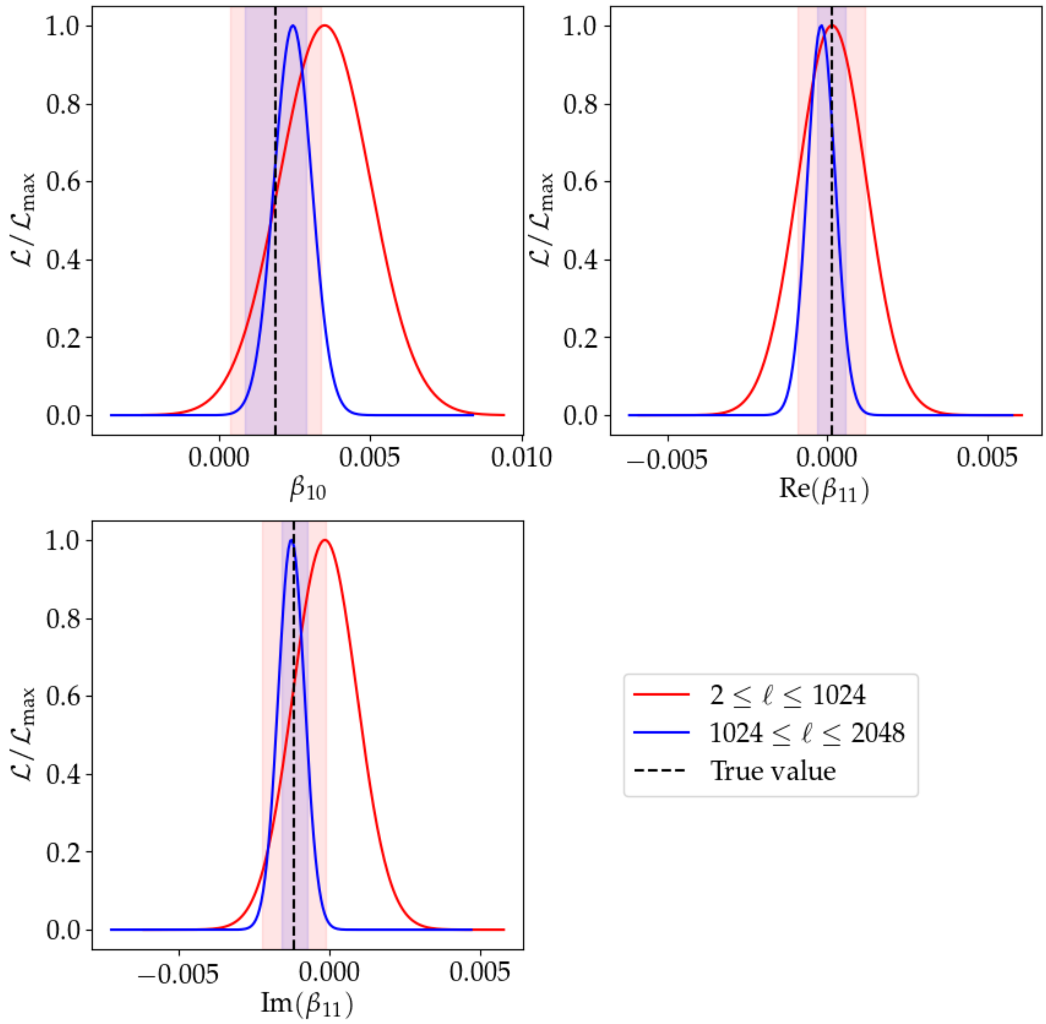

Figure 5.6: Normalized likelihood slices for full boosting likelihood using two disjoint multipolar regions in the interval $2 \leq \ell \leq 1024$ (red) and $1024 < \ell \leq 2048$ (blue). The light regions corresponds to 1σ interval for each case centered at the true input value in Monte Carlo simulations (dashed line).

At this point, likelihood slices show reliability for a further MCMC analysis by using the likelihood proposed in equation (5.16). As it has been shown in the normalized slices, they appear Gaussian distributed in all of the presented cases, this property will be used to build a consistent proposal matrix for the Metropolis-Hasting sampler described in the next section. A further additional test by using isotropic noise, and a discussion of their impact in the likelihood slices, can be found in Appendix E. In that section, the equivalence between auto-correlation and cross-correlation modes in the MCMC is shown.

5.2 MCMC estimations of $\boldsymbol{\beta}$

In this section, we apply MCMC techniques based on the likelihood estimator shown in equation (5.16). A Metropolis-Hastings algorithm [64] has been adopted as sampling method and implemented in a custom made code. MCMC samples obtained with this code were used to constrain the cartesian components of the boost velocity $\boldsymbol{\beta}$ previously used to boost statistically isotropic CMB maps. As mentioned before, the cosmological model was assumed to be known, therefore, the statistically isotropic power spectrum C_ℓ was kept fixed during the sampling.

5.2.1 MCMC estimation of β_{1N} components

We start the MCMC analysis by using full sky CMB synthetic maps with full boosting effects described in chapter 3. The data processing is similar to the one presented in in chapter 4. As it was mentioned before, the starting point of the Metropolis-Hastings algorithm employs a proposal covariance matrix, that for this particular case is assumed to be diagonal:

$$\Sigma = \mathrm{Diag}(\sigma^2_{\beta_{10}}, \sigma^2_{\mathrm{Re}(\beta_{11})}, \sigma^2_{\mathrm{Im}(\beta_{11})}), \tag{5.17}$$

where the matrix elements $\sigma^2_{\beta_{10}}$, $\sigma^2_{\mathrm{Re}(\beta_{11})}$, $\sigma^2_{\mathrm{Im}(\beta_{11})}$ are the corresponding variances from the likelihood slices in figure (5.5) for the $\ell_{\max} = 2048$.

The likelihood to be sampled in this pipeline is given by equation (5.16), with CMB covariance matrix given by (5.11), (5.12) and (5.13). This Joint-Bayesian likelihood is implemented manually in a `C++` code linked against `HEALPix C++` libraries for harmonic decomposition and manipulation of the synthetic CMB sky maps. The employed sampler in this chapter is limited to a three dimensional parameter space containing the harmonic components of $\boldsymbol{\beta}$: β_{10}, $\mathrm{Re}(\beta_{11})$ and $\mathrm{Im}(\beta_{11})$ with fixed power spectrum C_ℓ. Although $\ell = 2048$ is the preferred resolution for CMB sky maps, we also work with a lower resolution for showing properties of the posterior distributions for β_{1N} (i.e. $\ell = 1024$). Figure (5.7) shows a diagrammatic description of the data simulation and analysis, starting from CMB synthetic maps generation, following the likelihood slicing for estimating the proposal covariance matrix, and Markov chains extraction.

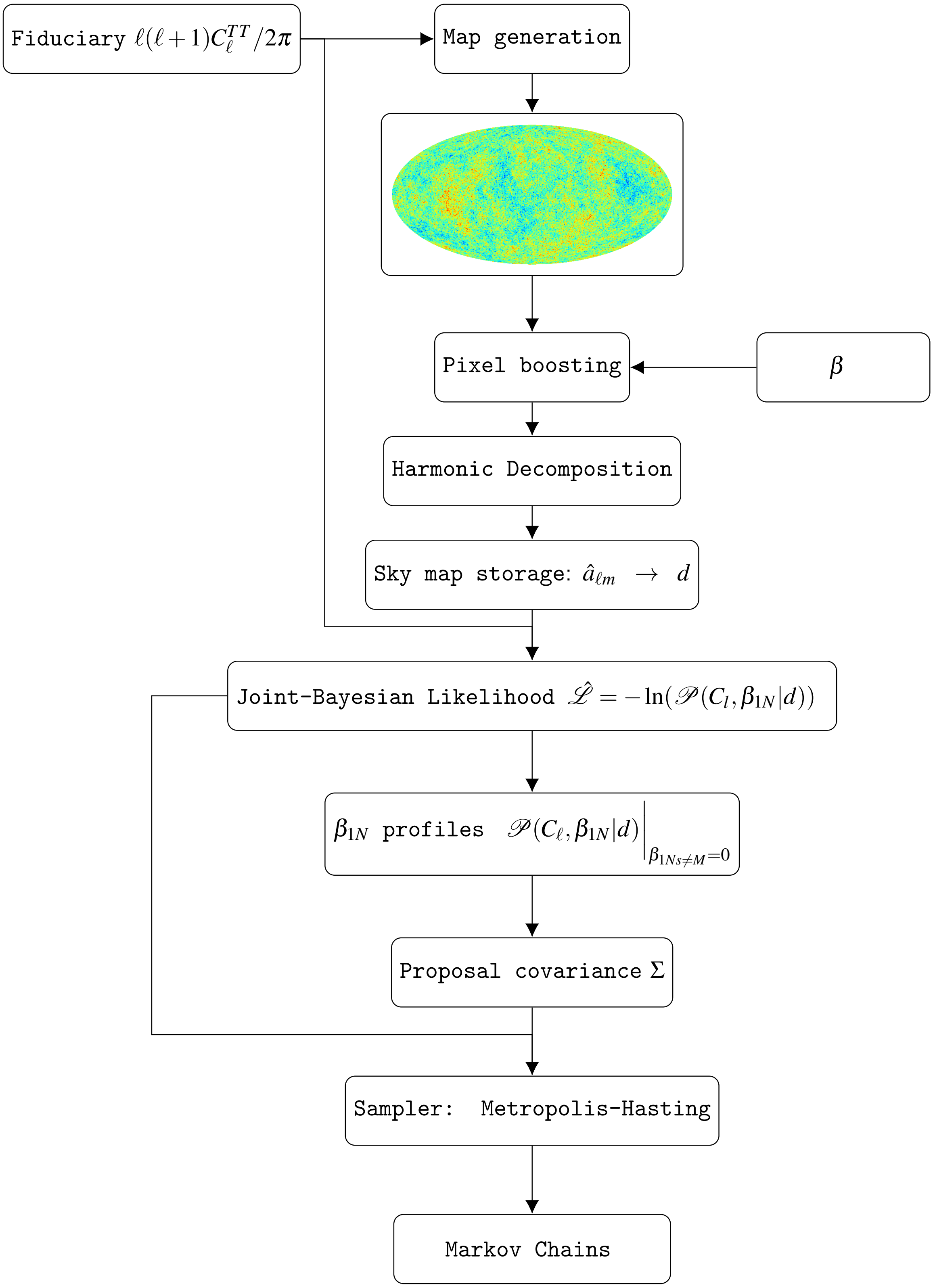

Figure 5.7: Schematic description of the simulation and analysis pipeline employed for an MCMC-based estimation of the boost velocity. Normalized likelihood slices are used to construct the covariance matrix proposal Σ for the MCMC Metropolis-Hasting sampler and obtain the Markov Chains for β_{1N}.

After following a similar sample cleaning and decorrelation on the Markov chains as the one in chapter 4 for cosmological parameters analysis (see Appendix C), posterior distributions are obtained from likelihood (5.16). Figure (5.8) shows the posterior distributions for the harmonic space components of β, depicting the increase in constraining power as one probes smaller angular scales going from $\ell_{max} = 1024$ to $\ell_{max} = 2048$. As discussed before, this can be explained by the fact that, from the statistical point of view, there is significant information contained in the region $1024 \leq \ell \leq 2048$ due to aberration effects in this multipole range.

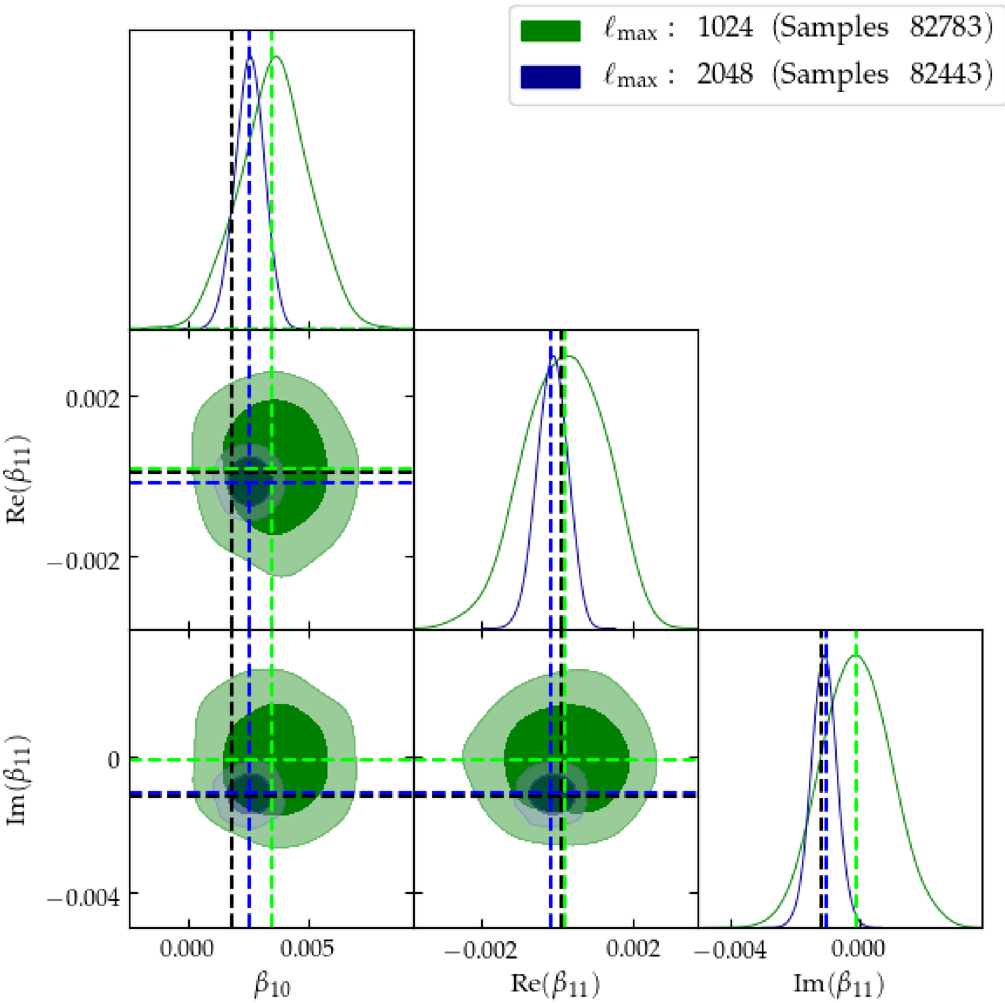

Figure 5.8: Posterior distributions for the harmonic space components of boost velocity $\boldsymbol{\beta}$. Two values of maximum multipoles are shown: $\ell_{max} = 1024$ (green) and $\ell_{max} = 2048$ (blue). The true value is represented by the black dotted line corresponding to $\beta = 1.23 \times 10^{-3}$ in the direction of equation (4.8). An approximation to the maximum likelihood solution is shown in blue and green dotted lines corresponding to the mean of the posterior distribution.

Table (5.1) summarizes the results for these two cases ($\ell_{max} = 1024, 2048$), showing maximum likelihood estimates for the components of $\boldsymbol{\beta}$, as well as residuals, with respect to the true values in the direction given by equation (4.8). The maximum likelihood solution in this table is taken as the mean value of the posterior of figure (5.8). This is an approximation, it is clearly a good one, given the symmetric shape of the posteriors and the small level of correlations between the parameters as can be seen in figure (5.9).

Parameter	True value	$\ell_{max} = 1024$	Δ ($\ell_{max} = 1024$)	$\ell_{max} = 2048$	Δ ($\ell_{max} = 2048$)
$\beta_{10} \times 10^3$	1.85	$3.5^{+1.5}_{-1.7}$	1.06	2.55 ± 0.58	1.20
$\mathrm{Re}(\beta_{11}) \times 10^4$	1.22	$2.1^{+1.1}_{-0.9}$	0.09	-1.6 ± 3.9	-0.71
$\mathrm{Im}(\beta_{11}) \times 10^3$	-1.16	-0.1 ± 1.2	1.03	-1.1 ± 0.4	0.29

Table 5.1: Observed mean values for the boosting harmonic parameters at $\ell_{max} = 1024, 2048$ for the TT Joint-Bayesian likelihood.

The resulting correlation matrix for these paramaters is shown in figure (5.9), where negligible correlation between the parameters is appearing. One can conclude, therefore, that the full posteriors can be approximated by a product of marginalized posteriors. Moreover, using the marginalized posteriors to extract the maximum likelihood values of β_{1N} is also a safe procedure.

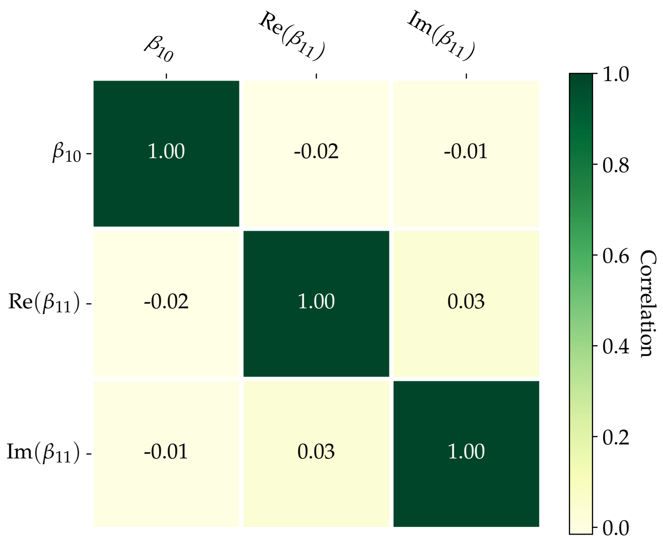

Figure 5.9: Correlation matrix for the boosting parameters in harmonic space β_{1N}. The samples used in this calculation were obtained from the posterior distribution sampled with a covariance matrix including $\ell_{\max} = 2048$ multipoles.

5.3 Derived angular resolution

In this section we obtain the angular resolution of our maximum likelihood estimator by looking at the posterior distributions of the opening angle:

$$\eta = \cos^{-1}\left(\frac{\hat{\boldsymbol{\beta}} \cdot \boldsymbol{\beta}_{\mathbf{true}}}{|\hat{\boldsymbol{\beta}}||\hat{\boldsymbol{\beta}}_{\mathbf{true}}|}\right). \tag{5.18}$$

In addition to solid angle effects due to the definition of the random variables η, we assume that η is affected by Gaussian fluctuations. Therefore, our model for the PDF of η is given by:

$$\mathcal{P}(\eta) = N \sin(\eta) \exp(-\eta^2/2\sigma^2), \tag{5.19}$$

where N is a normalization constant, σ is the standard deviation of the Gaussian fluctuation on η, therefore, σ is what we shall compare with previous estimates in the literature. Figure (5.10) shows the posterior distribution of η for the MCMC samples shown in figure (5.8). The best fit curves to each maximum multipole case are also shown.

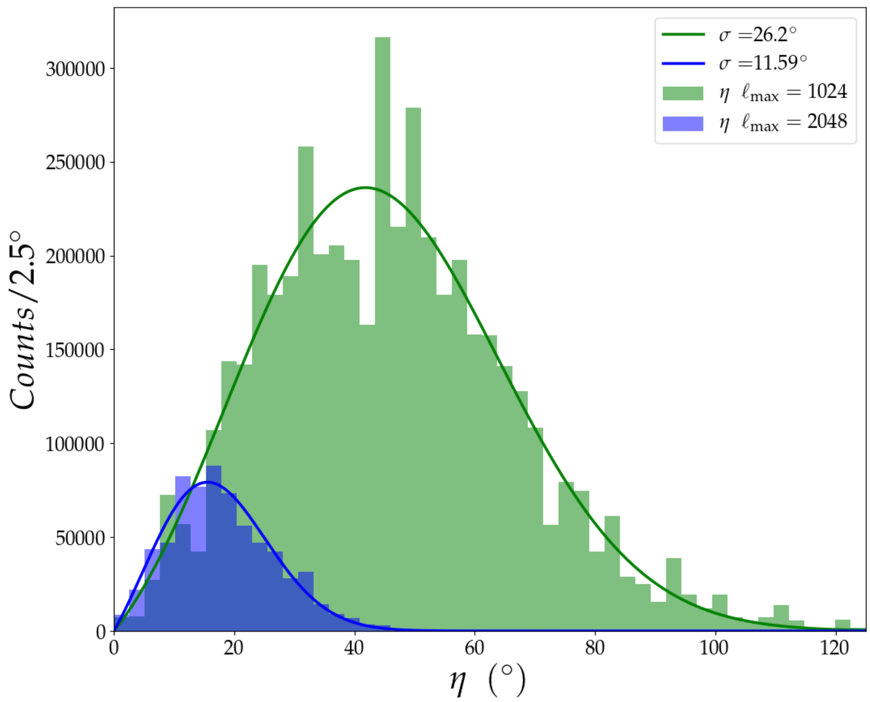

Figure 5.10: Posterior distributions for the opening angle η, given by equation (5.18), compared to the best fit curves of the model, given by equation (5.19). Two cases are shown: $\ell_{\max} = 1024$ (green) and $\ell_{\max} = 2048$ (blue).

From the histogram in figure (5.10), the η distribution allows to constrain solid angle regions in the sky. By using the variance σ in equation (5.19) all sampled vectors

$\boldsymbol{\beta}$ within 1σ correspond to 68% uncertainity in the estimated most likely direction $\boldsymbol{\beta}_{\max}$ defining a 1σ confidence circle in the sky. As it is shown in figure (5.10), this variance depends on the resolution of the CMB maps from where the MCMC samples were extracted.

As a final step for the presented MCMC analysis, we compare the obtained results for $\ell_{\max} = 2048$ with the *Planck* collaboration analysis in [11]. For the *Planck* telescope it is reported a confidence circle at 68% of $14°$ and $26°$ for the 2σ case. Figure (5.11) shows these two measurements and their confidence circles centered in the corresponding maximum likelihood estimated values.

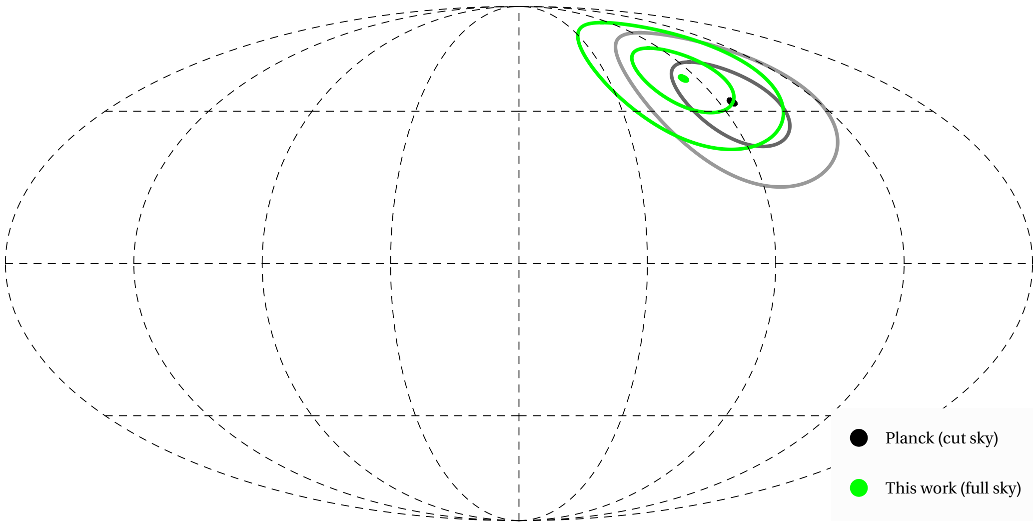

Figure 5.11: 1σ and 2σ C.L. regions around their corresponding best fit directions for this work (green) and for *Planck* (black) [11]. The system of reference is adapted to be centered at $(L, B) = (360°, 0°)$ in galactic coordinates.

As final result, table (5.2) shows the set of real space components of $\boldsymbol{\beta}$ at $\ell_{\max} = 2048$ in galactic coordinates extracted from the MCMC chains in figure (5.8) compared to that reported by the *Planck* collaboration in [11].

Parameter	This work (full sky)	*Planck* (cut sky) [11]
v_{dip}	433 ± 84 km s^{-1}	$384 \pm 78 \pm 115$ km s^{-1}
η (1σ)	$11.5° \pm 0.5°$	$14°$
η (2σ)	$23.0° \pm 1.0°$	$26°$

Table 5.2: Summary of the obtained results for the $\ell_{max} = 2048$ Joint-Bayesian likelihood estimator. Both the magnitude and 1σ uncertainty for $\boldsymbol{\beta}$ as well as the 1σ and 2σ confidence regions for the opening angle η are shown.

It is worth mentioning a few technical details involved in the extraction of MCMC chains based on the likelihood (5.16). The matrix multiplications appearing in this equation were optimized to take advantage of the fact that the matrices are sparse. Nevertheless, they still contain typically a total of $\sim 10^6$ elements for $\ell_{max} = 2048$. On the other hand, for the Gellman-Rubin criterion adopted here ($1 - R \lesssim 0.01$), about 8×10^4 samples are required before achieving convergence. This implies that a full chain for statistical analyses takes about 8 days running in a parallelized environment with 8 cores and 48 Gb of RAM memory. Therefore, we have been unable to generate a sufficiently large ensemble of skies required to properly assess potentially small systematic effects. However, for the few independent skies generated in this chapter, we have not observed any indication of bias in the estimator and we hope that in the limit of a large number of sky realizations, the parameters shown in table (5.1) converge to their true values.

Since the analysis was performed in full sky mode, therefore there are no artifacts introduced by a mask; The sky maps used as input to the MCMC code were free from foregrounds, containing only the cosmic signal, therefore residual galactic contamination is not an issue. Candidates that could contribute to the systematic uncertainty were the expansion on $\boldsymbol{\beta}$ shown in equation (5.16) and the weak lensing approximation to the aberration covariance matrix implicit in equation (5.13). However, we have shown in this chapter, using synthetic sky maps fully boosted in pixel space (i.e. no approximation), that in the multipole range $2 \leq \ell \leq 2048$, these are perfectly good approximations for $\beta \sim 10^{-3}$.

5.4 Summary

We have presented in this chapter an MCMC estimation via a Joint-Bayesian likelihood estimator of the solar system velocity with respect to the CMB rest frame using the break of statistical isotropy at first order in the boost velocity introduced by the change of frame. The implemented likelihood method was adapted from the cosmic hemispherical asymmetry (CHA) study elaborated in [15], where we have included, in addition to the modulation term, a corresponding contribution associated to relativistic aberration. This formalism was applied for reconstructing the boost velocity $\boldsymbol{\beta}$ and comparing it to the *Planck* collaboration results in [11].

Within the weak lensing approximation, the covariance matrices for Doppler modulation (see equation (5.12)) and aberration (see equation (5.13)) show that modulation effects are negligible at small scales ($\ell > 1000$), an angular region dominated by small deflections in the photon directions due to aberration. This had already been previously discussed in chapter 3 (see figure 3.7). On the other hand, the aberration effects completely dominate the likelihood for high resolution experiments as figure (5.2) shows, an effect also predicted in the cross-correlation function calculated in figure (3.7). In all of the situations considered in section 5.1 (i.e. higher multipoles, different input velocities) the likelihood successfully estimated the harmonic components of $\boldsymbol{\beta}$ showing consistency in less than 1σ with respect to the input value in simulations.

From the MCMC analysis, conclusions are drawn from the posterior distributions in harmonic space, where an agreement is shown in less than 1σ with respect to the true boost velocity $\boldsymbol{\beta}$ value for the highest resolution case with $\ell_{\rm max} = 2048$. Another interesting result, is the little correlation between the parameters (see figure (5.9)) that allows to conclude that the posterior can be approximated by a product of the marginalized individual posteriors. However, this might not work when mask effects are added.

Once the accuracy of the method has been addressed, by showing that our Joint-Bayesian estimator is unbiased, we have made a final comparison of the resolution achieved by this estimator with a previous result in the literature, that is, the Planck aberration dominated measurement of $\boldsymbol{\beta}$ using quadratic estimators [11]. The estimator of this dissertation is competitive in terms of resolution, leading to a statistical uncertainty just 7% higher than the one from the *Planck* Collaboration (84 km s^{-1} for $2 \leq \ell \leq 2048$ versus 78 km s^{-1} for $500 \leq \ell \leq 2000$).

6 | Conclusions

In this work, we have presented the effects induced by peculiar motion of the solar system with respect to the CMB reference frame. Firstly by studying its impact in the underlying cosmological parameters, then estimating the boost velocity itself using standard MCMC techniques. The problem is presented in three different levels of complexity starting from Monte Carlo generated synthetic sky maps, from where Doppler modulation and aberration signals in the cross-correlation function $\langle a_{\ell m} a^*_{\ell+1 m}\rangle$ were retrieved, in agreement with previously described effects in the literature [12, 13, 58]. Then, the impact of neglecting local kinematic effects when estimating cosmological parameters has been quantified and shown to be negligible compared to the current resolution provided by satellites like *Planck*. Finally, we extended and tested the likelihood estimator presented in [15] by adding the aberration effects.

In chapter 3, using full sky CMB synthetic maps, we have shown that the boosting signal appears in all the power spectra (i.e. C_ℓ^{TT}, C_ℓ^{TE} and C_ℓ^{EE}) in addition to inducing correlations in the $\langle a_{\ell m} a^*_{\ell+1 m}\rangle$ cross-correlation function. All the signal extractions were compatible with previous results reported in the literature that support the weak lensing approximation for modeling aberration effects in the anisotropies [13, 14, 58] (see figure (3.7)). In addition, it was observed by the good agreement between the extracted cross-correlation functions from full-sky simulated CMB maps fully boosted in pixel space (see figure (3.7)), that the approximation is sufficiently good to model this effect. This figure was produced after cosmic variance reduction, showing a good agreement between the exact cross-correlation extracted from the pixelized maps and the corresponding weak lensing-based theoretical curve [13].

We have tested the reliability of cosmological parameters extracted in the presence of uncorrected local kinematic effects. The question of whether these parameters may be affected by boosting effects was addressed by using the 2018 CMB temperature and polarization power spectrum error bars from *Planck* collaboration. MCMC chains were constructed from different sets of likelihoods using temperature and polarization power spectra (see figure (4.2)). Markov chains based on these likelihoods were fed with sky maps where the primordial statistically isotropic CMB Stokes parameters I, Q and U were transformed into a moving frame with velocity consistent with that of our solar system. The cosmological parameters extracted from the posterior distributions were then compared to those extracted from statistically isotropic maps as well as to the ones obtained by the *Planck* collaboration, showing an agreement within 1σ in all the cases. The likelihoods allowed us to conclude that there is no significant change in the base-ΛCDM parameters for a boost velocity $\beta = 1.23 \times 10^{-3}$ in the direction given by equation (4.8) and three different data sets: intensity-only `TT` (see table 4.4), polarization-only `EE` (see table 4.5) and temperature-polarization `TE` (4.6) spectra. The same conclusion is also drawn in the highest constraining case of a combined `TT+EE+TE` likelihood (see figure 4.11 and table 4.8).

In the Bayesian estimation of $\boldsymbol{\beta}$, we have employed the weak lensing approximation for the aberration effects, together with a very useful expansion in β of the likelihood (see equation (5.16)). Except for the pixelized input sky maps, all the subsequent analysis steps were performed in harmonic space. At the level of map generation, all boost effects were introduced without any approximation and are only limited by the computer's double precision. The analysis presented here differ from that used by the *Planck* collaboration in a few aspects: the estimator used and the lack of real data complications like partial sky coverage, residual foregrounds and not fully understood large scale anomalies. Regarding the estimator, we have extended the one presented in [15] for studying the CHA, and that perfectly describes the Doppler modulation contribution (see equation (5.12)). The extension was performed by adding an extra term dealing with relativistic aberration (see equation (5.13)). The range of applicability of the weak lensing approximation has been studied by considering different boost velocity magnitudes and angular resolutions in harmonic space (i.e. different $\ell_{\rm max}$). The study showed the break of the approximation when one probes regions where $\beta\ell_{\rm max} \geq 1$ (see figure (5.4)).

We have also highlighted intrinsic properties of the estimator in order to validate the technique for measuring $\boldsymbol{\beta}$, i.e variance reduction by including higher multipoles (see figure (5.5)), the role played in the likelihood by Doppler modulation and aberration effects (see figure (5.2)), and the dominance (from the statistical point of view) of the small scales over the large ones (see figure (5.6)). The estimator successfully recovered the input velocity in full sky CMB maps, with a resolution compatible to the *Planck* estimator. The final accuracy and resolution of our Joint-Bayesian estimator can be seen in table (5.2) and sky map of figure (5.11).

It is worth mentioning that we have also extended the Joint-Bayesian estimator presented in this dissertation to also include information on polarization. More precisely, the boosting effects on all three cosmologically relevant Stokes parameters I, Q and U have been calculated. These effects have been used for cosmological studies in chapter 4, but still need to be fully validated when incorporated in the covariance matrices of chapter 5. Such a validation is an ongoing work, but will certainly improve the final resolution on $\boldsymbol{\beta}$. The use of polarized anisotropies is motivated by recent works using this kind of data in [55] where an independent measurement of $\boldsymbol{\beta}$, using EE modes polarization, is presented.

Although we have presented the Doppler modulation and aberration detection in full-sky synthetic CMB maps, the work is perfectly extendable to a more general situation where an extended data processing pipeline is considered. For example, we notice that all presented results were robust and consistent in a full sky coverage regime; however, it is known that in order to work with real CMB sky maps, a masking procedure over the galactic plane is needed. Even though these effects are not considered here, they represent an important source of systematic effects in the obtained posterior distributions for $\boldsymbol{\beta}$ [11]. These sources of systematic uncertainty must be studied and taken into account inside the estimator before treating real CMB sky maps.

We mention at least two ways to deal with partial sky coverage effects in our estimator: 1. the use of marginalization over the signal in the masked region like that implemented in [15] through the combination of MCMC techniques and Hamiltonian Monte Carlo methods (HMC) [77–79] or 2. the incorporation of the additional mask mixing on top of that induced by the boost as presented in [80]. The first option above is the one currently under implementation by us.

A | Healpix polarization conventions

A.1 Polarization conventions

As it is shown in [81], polarization field is a second rank symmetric trace-free tensor, that can be written in the following way:

$$P_{ij} = {}_2\mathcal{A}(\hat{\boldsymbol{n}})\boldsymbol{m}_i^*\boldsymbol{m}_j^* + {}_{-2}\mathcal{A}(\hat{\boldsymbol{n}})\boldsymbol{m}_i\boldsymbol{m}_j, \tag{A.1}$$

where the quantity ${}_{\pm 2}\mathcal{A}(\hat{\boldsymbol{n}})$ as:

$${}_{\pm 2}\mathcal{A}(\hat{\boldsymbol{n}}) = Q(\hat{\boldsymbol{n}}) \pm iU(\hat{\boldsymbol{n}}). \tag{A.2}$$

In order to specify the basis in which the tensor is written, the two linear-independent vectors: $\boldsymbol{m}$ and $\boldsymbol{m}_i^*$ are written explicitly in a coordinate basis form (later on specifying the coordinate system itself i.e. spherical coordinates (within the Healpix conventions)):

$$\boldsymbol{m} = \frac{1}{\sqrt{2}}(\hat{\boldsymbol{e}}_{\boldsymbol{1}} + i\hat{\boldsymbol{e}}_{\boldsymbol{2}}) = \frac{1}{\sqrt{2}}(\hat{\boldsymbol{e}}_{\boldsymbol{\theta}} + i\hat{\boldsymbol{e}}_{\boldsymbol{\phi}}), \tag{A.3}$$

$$\boldsymbol{m}^* = \frac{1}{\sqrt{2}}(\hat{\boldsymbol{e}}_{\boldsymbol{1}} - i\hat{\boldsymbol{e}}_{\boldsymbol{2}}) = \frac{1}{\sqrt{2}}(\hat{\boldsymbol{e}}_{\boldsymbol{\theta}} - i\hat{\boldsymbol{e}}_{\boldsymbol{\phi}}), \tag{A.4}$$

by setting the basis: $\hat{\boldsymbol{e}}_{\boldsymbol{1}} = \hat{\boldsymbol{e}}_{\boldsymbol{\theta}}$, $\hat{\boldsymbol{e}}_{\boldsymbol{1}} = \hat{\boldsymbol{e}}_{\boldsymbol{\phi}}$, as is specified in [81], under a local, right-handed rotation of the basis $\hat{\boldsymbol{e}}_{\boldsymbol{1}}$, $\hat{\boldsymbol{e}}_{\boldsymbol{2}}$ by an angle ψ, complex stokes parameters ${}_{\pm 2}\mathcal{A}(\hat{\boldsymbol{n}})$, by convention we can specify the quantity ${}_{\pm 2}\mathcal{A}(\hat{\boldsymbol{n}})$ in the basis [43]:

$${}_{\pm 2}\mathcal{A}(\hat{\boldsymbol{n}}) = \sum_{l=0}^{\infty}\sum_{m=-\ell}^{\ell} a_{\pm 2,\ell m}\ {}_{\pm 2}Y_\ell^m(\hat{\boldsymbol{n}}), \tag{A.5}$$

which allows to write the definitions of $Q(\hat{\boldsymbol{n}})$ and $U(\hat{\boldsymbol{n}})$:

$$(Q(\hat{\boldsymbol{n}}) + iU(\hat{\boldsymbol{n}})) = \sum_{l=0}^{\infty}\sum_{m=-\ell}^{\ell} a_{2,\ell m}\ {}_2Y_\ell^m(\boldsymbol{n}), \tag{A.6}$$

$$(Q(\hat{\boldsymbol{n}}) - iU(\hat{\boldsymbol{n}})) = \sum_{l=0}^{\infty}\sum_{m=-\ell}^{\ell} a_{-2,\ell m}\ {}_{-2}Y_\ell^m(\boldsymbol{n}), \tag{A.7}$$

from where we obtain the following definitions:

$$a_{\ell m}^E = -(a_{2,\ell m} + a_{-2,\ell m})/2 \quad , \quad a_{\ell m}^B = -(a_{2,\ell m} - a_{-2,\ell m})/2i. \tag{A.8}$$

These coefficients are used to compute the polarization power spectra C_ℓ^{EE} and C_ℓ^{TE} used in this work. We adopt the `HEALPix` convention in polarization for all the calculations concerning polarization spectra.

B | The black body spectrum under a Lorentz boost

The intensity measured for the CMB is given by:

$$I'(\nu', \hat{\boldsymbol{n}}) = \frac{2h\nu'^3}{c^2}\Big(\exp(h\nu'/k_B T(\hat{\boldsymbol{n}})) - 1\Big)^{-1}, \tag{B.1}$$

the measured photon frequencies are Doppler shifted by an amount:

$$\nu' = \nu\gamma(1 - \boldsymbol{\beta} \cdot \hat{\boldsymbol{n}}). \tag{B.2}$$

in the moving frame the intensity is given by:

$$I'(\nu', \hat{\boldsymbol{n}}) = \frac{2h(\nu\gamma(1 - \boldsymbol{\beta} \cdot \hat{\boldsymbol{n}}))^3}{c^2}\Big(\exp[h(\nu\gamma(1 - \boldsymbol{\beta} \cdot \hat{\boldsymbol{n}}))/k_B T(\hat{\boldsymbol{n}})] - 1\Big)^{-1}, \tag{B.3}$$

with the appearance of the frequency-depended modulation, as it is shown in [14]. Using the properties of the Poincare sphere for Stokes parameters, the same property can be mapped from the intensity to the polarization parameters:

$$I^2 = Q^2 + U^2. \tag{B.4}$$

The last equation is rotational invariant, which means, that we can fix $U = 0$, and get the same properties for Intensity but for parameter Q, and then rotate, and fix U, performing these, the law of transformations under a Lorentz transformation behaves as:

$$\tilde{I}'(\nu', \hat{\boldsymbol{n}}) = \tilde{I}(\nu, \hat{\boldsymbol{n}})\left(\frac{\nu'}{\nu}\right)^3, \tag{B.5}$$

$$\tilde{Q}'(\nu', \hat{\boldsymbol{n}}) = \tilde{Q}(\nu, \hat{\boldsymbol{n}})\left(\frac{\nu'}{\nu}\right)^3, \tag{B.6}$$

$$\tilde{U}'(\nu', \hat{\boldsymbol{n}}) = \tilde{U}(\nu, \hat{\boldsymbol{n}})\left(\frac{\nu'}{\nu}\right)^3, \tag{B.7}$$

where the tick quantities refers to the Stokes parameters per unit of solid angle, measured in the moving frame, in agreement with [14]. The vector $\hat{\boldsymbol{n}}$ is the same used in chapter 3.

C | MCMC chains

In this appendix we show the details behind the employed MCMC chains for cosmological parameters analysis and the joint-Bayesian likelihood estimator for $\boldsymbol{\beta}$. We employed the statistical python package `GetDist` [73] for plotting, testing and checking statistical consistency in all the MCMC chains obtained in this work. Convergence test are based in the Gelman-Rubin test for showing whether the chain has reached its asymptotic probability distribution [64].

C.1 MCMC samplers

For the cosmological parameters analysis we were interested in sampling base-ΛCDM parameters. In the chains we sampled 6 of the 9 paremeters used by *Planck* collaboration in [70]. We employed the sampling code `CosmoMC` [82] for this part of the analysis due its performance in multi-core and multi-node environments and its adaptability in using *Planck* likelihood products. Table (C.1) shows the configuration details used in the sampler for all the chains considered in this work.

Parameter	Value	Description
Boltzmann Equation Integrator	`CAMB`	Solver for Boltzmann differential equations [38].
CPUs	16	Number of CPUs used bythe MPI multiprocessor framework.
Sampling method	Draggin method	Default method used for sampling slow parameters [82].
Chains step	4×10^6	Total number of steps in the chain.
Priors	Flat	No prior information used in the chains.

Table C.1: Configuration details used in `CosmoMC` sampler.

In addition to cosmological parameters we have implemented a custom-made sampler based on the Metropolis-Hastings algorithm [64] to sample the posterior distributions in the estimation of the velocity vector $\boldsymbol{\beta}$. This code was implemented in `C++` to sample boosting parameter space by employing the likelihood method of chapter 5. Table (C.2) presents the software configuration used for this specific likelihood presented in chapter 5.

Parameter	Value	Description
Synthetic map decomposition	`HEALPix`	libraries for harmonic decompostion.
Fiducial model generator	`CAMB`	Fiducial power spectrum in the likelihood.
Priors	Flat	No prior information used in the chains

Table C.2: Configuration details used in the Metropolis-Hastings sampler.

C.2 Auto-correlation

As it is expected from MCMC methods, samples are in principle correlated with their neighbors. In order to obtain truly independent samples the lag factor (also known as autocorrelation time) of the chain is estimated by calculating correlations between the samples along the chain by using the following equation:

$$A(l) = \frac{1}{N-l}\sum_{t=1}^{N-l}(X_t - \bar{X})(X_{t+l} - \bar{X}), \tag{C.1}$$

where $\bar{X}$ is the sample average, X_t is the sample at a given step t, N is the total number of samples in the chain, and l is the lag factor.

C.2.1 Combined analysis: TT+TE+EE likelihood

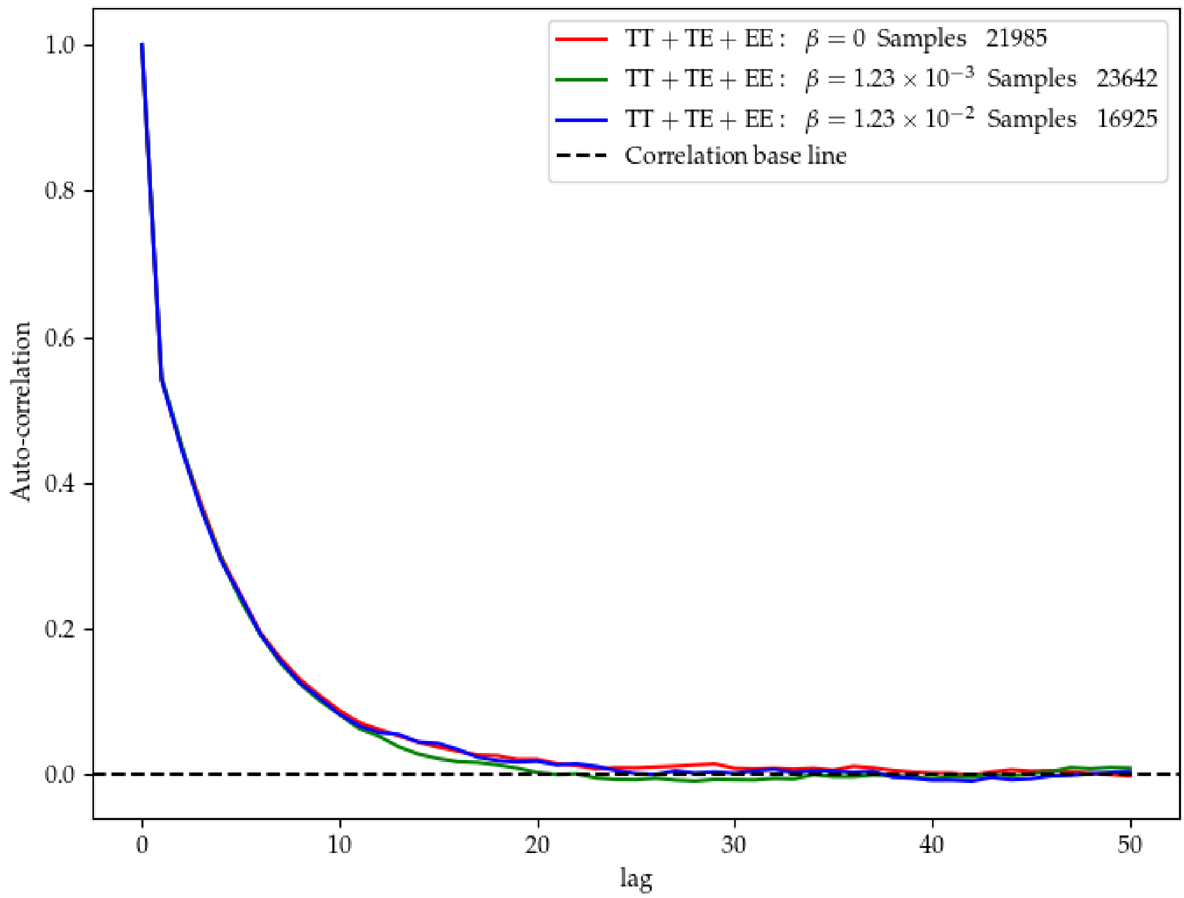

Figure C.1: Auto-correlation for the combined likelihood TT+TE+EE as a function of the lag for each considered boosting velocity $\boldsymbol{\beta} = (0, \boldsymbol{\beta}_{\rm dip}, 10 \times \boldsymbol{\beta}_{\rm dip})$.

C.2.2 Temperature: `TT` likelihood

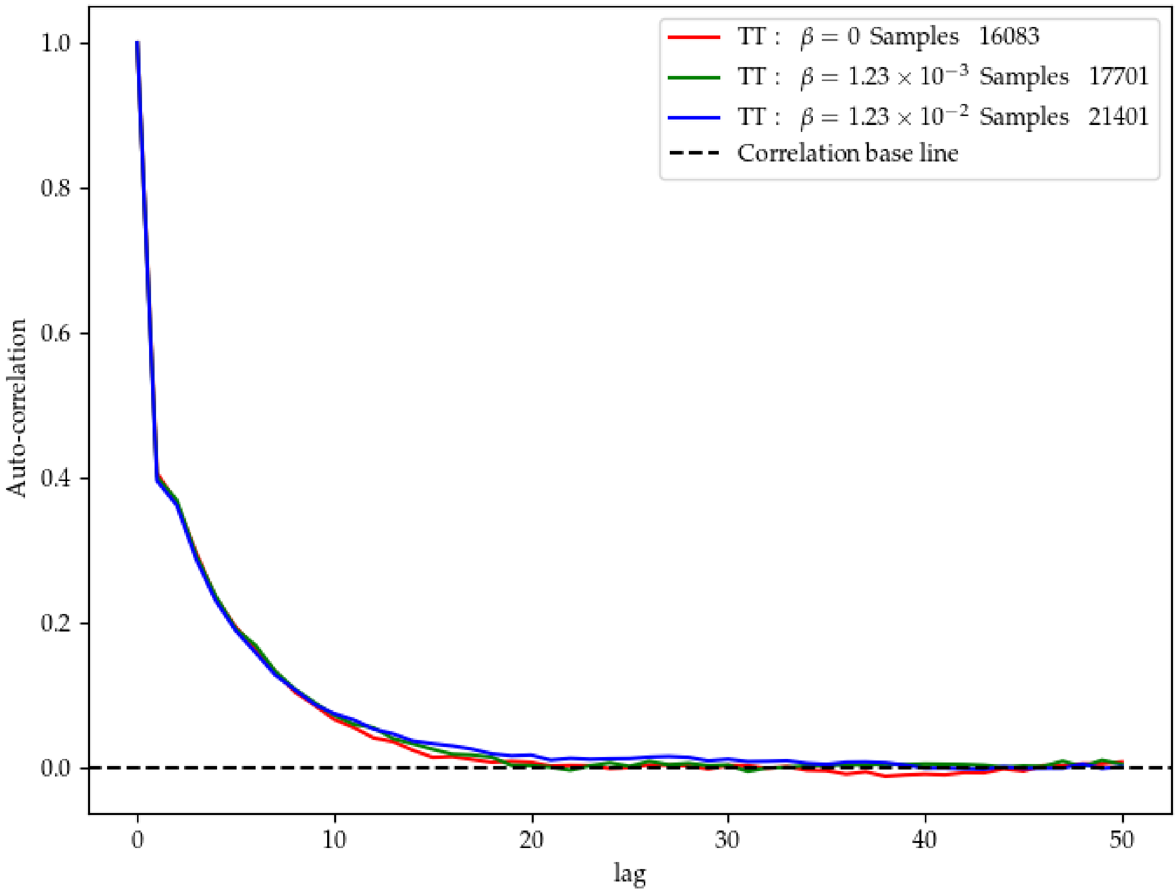

Figure C.2: Auto-correlation for the temperature likelihood as a function of the lag for each considered boosting velocity $\boldsymbol{\beta} = (0, \boldsymbol{\beta}_{\rm dip}, 10 \times \boldsymbol{\beta}_{\rm dip})$.

C.2.3 Polarization: `EE` likelihood

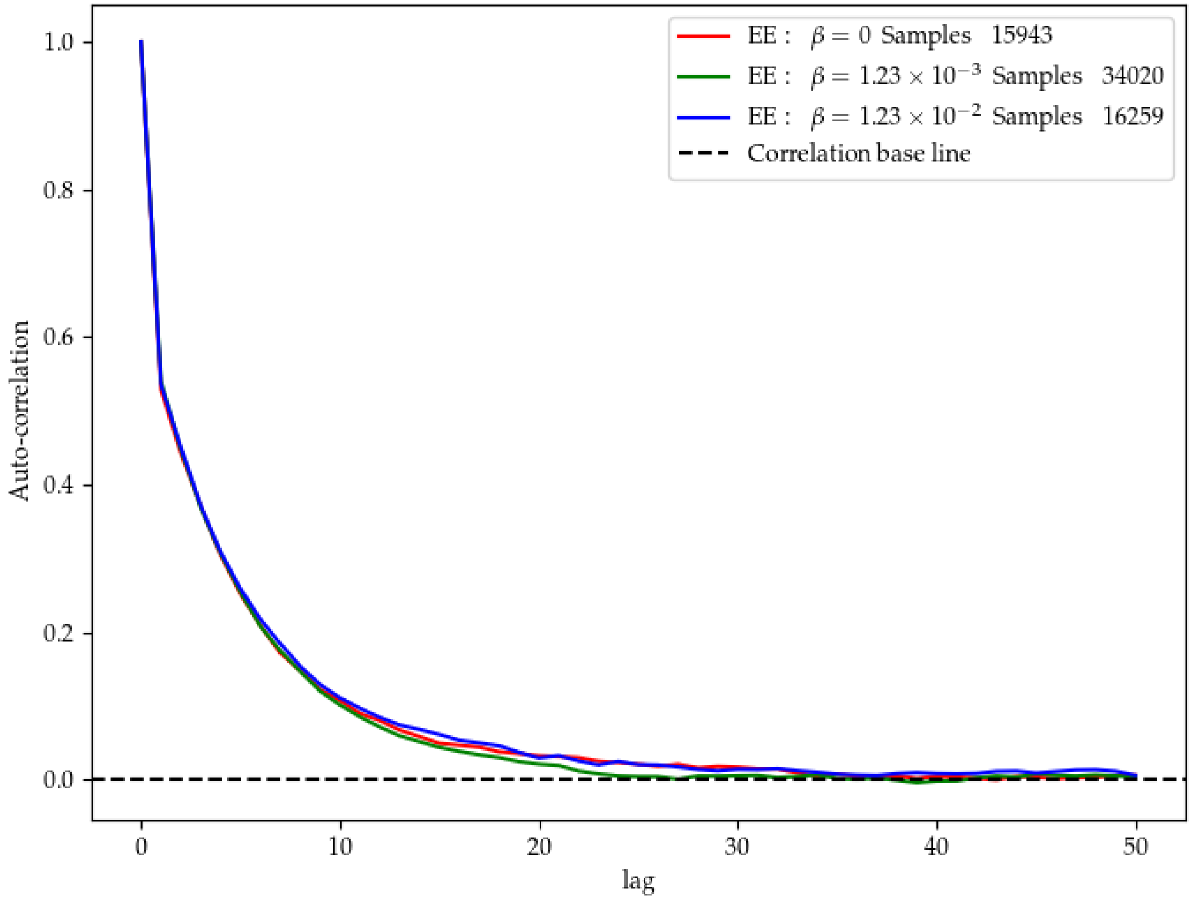

Figure C.3: Auto-correlation for the polarization likelihood as a function of the lag for each considered boosting velocity $\boldsymbol{\beta} = (0, \boldsymbol{\beta}_{\rm dip}, 10 \times \boldsymbol{\beta}_{\rm dip})$.

C.2.4 Temperature-Polarization: `TE` likelihood

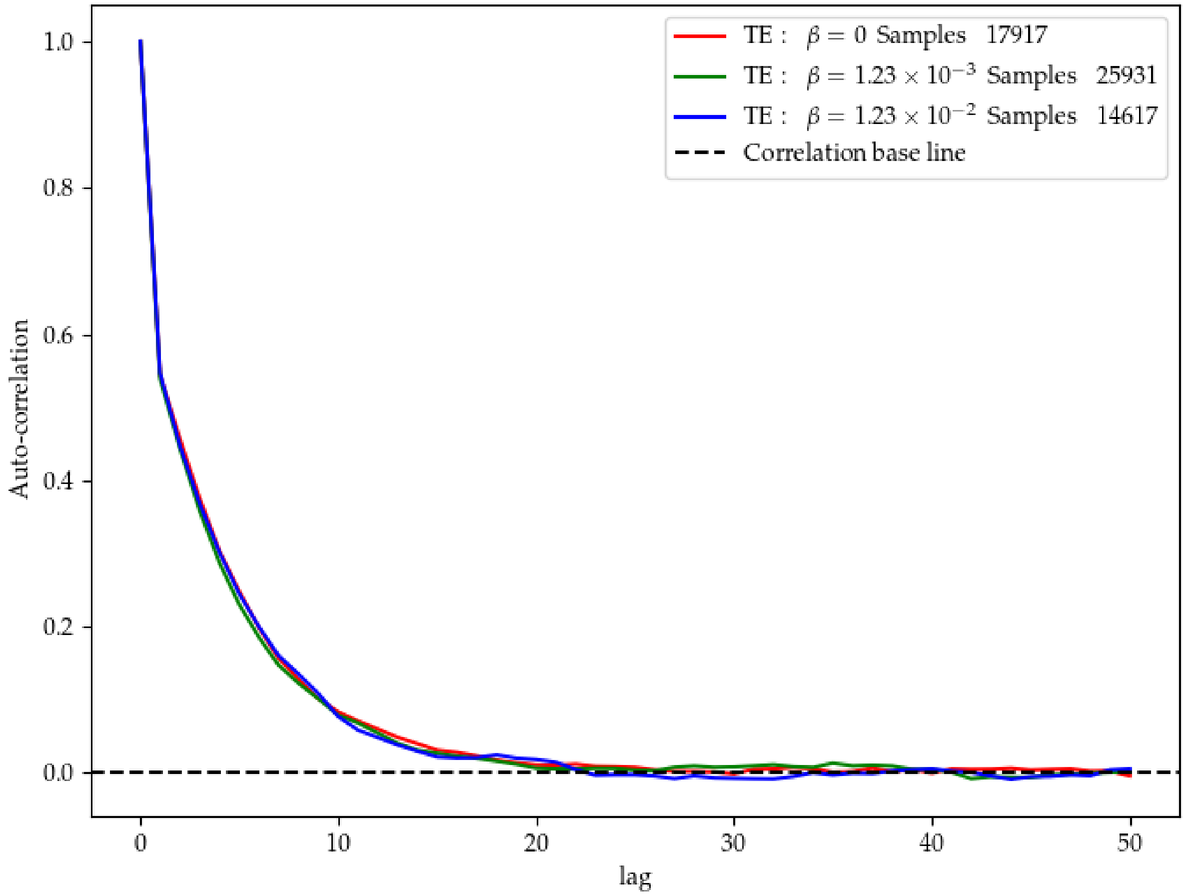

Figure C.4: Auto-correlation for the temperature-polarization likelihood as a function of the lag for each considered boosting velocity $\boldsymbol{\beta} = (0, \boldsymbol{\beta}_{\rm dip}, 10 \times \boldsymbol{\beta}_{\rm dip})$.

C.2.5 Boosting likelihood estimator

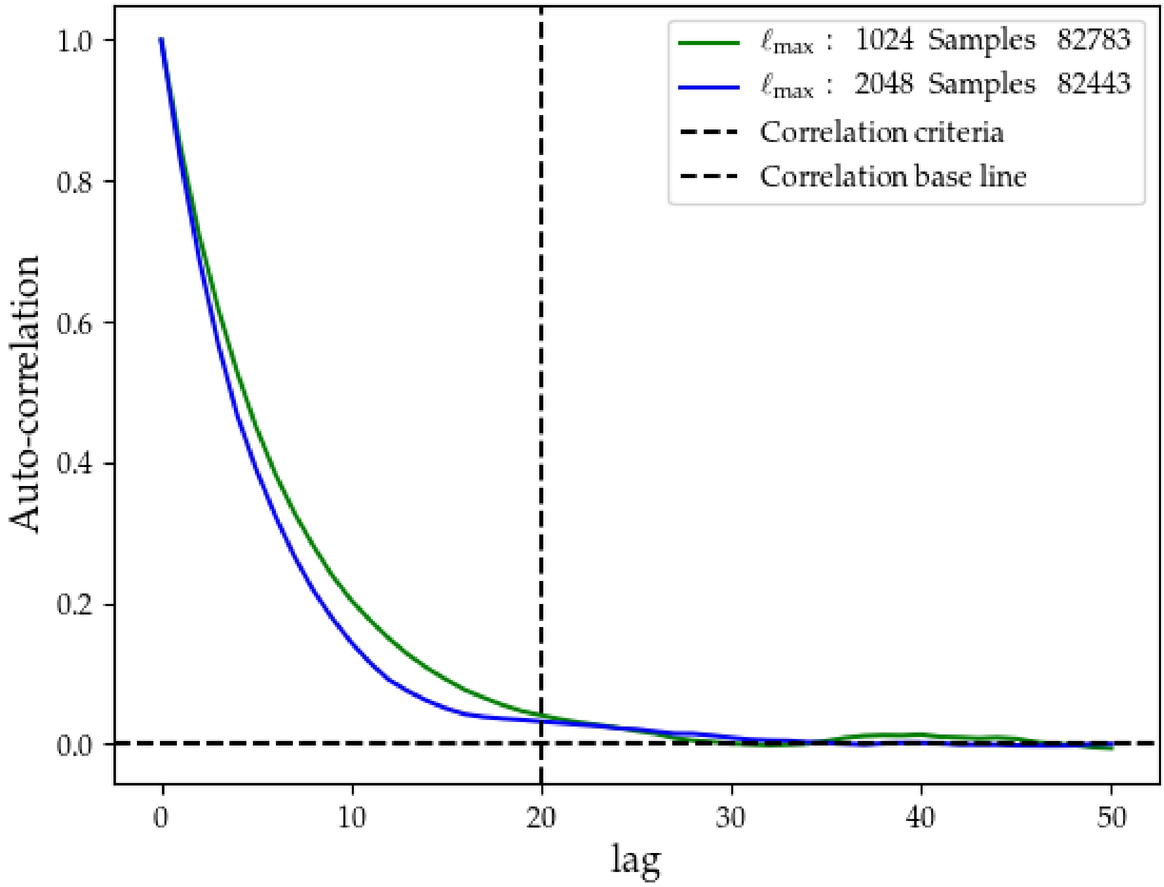

Figure C.5: Auto-correlation for the Joint-Bayesian likelihood estimator as a function of the lag for each multipole value used $\ell = (1024, 2048)$ in the likelihood.

C.3 Chains convergence

For convergence test we employed the so-called Gelman-Rubin test [74] in our MCMC chains for testing if the proposal distribution is reaching the asymptotic state. We use a convergence criteria of 1% deviation from the correlation factor R from 1. In the following we present convergence of the chains for each MCMC case presented in both chapters 4 and 5, showing that all the presented posterior distributions are truly asymptotic states of their respective chain.

C.3.1 Combined analysis: TT+TE+EE likelihood

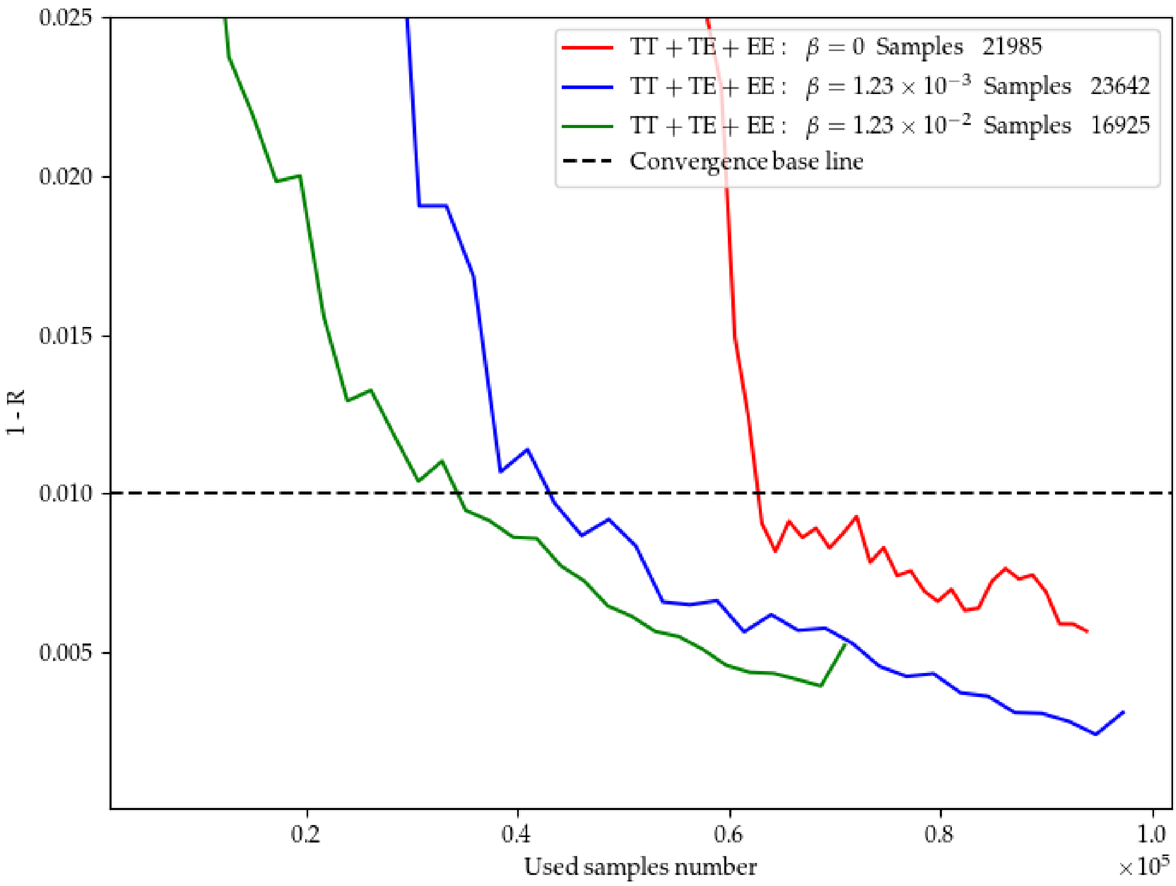

Figure C.6: Gelman-Rubin test for the combined TT+TE+EE likelihood for cosmological parameters estimation as a function of the number of total samples in the chain for each considered boosting velocity $\boldsymbol{\beta} = (0, \boldsymbol{\beta}_{\rm dip}, 10 \times \boldsymbol{\beta}_{\rm dip})$.

C.3.2 Temperature: `TT` likelihood

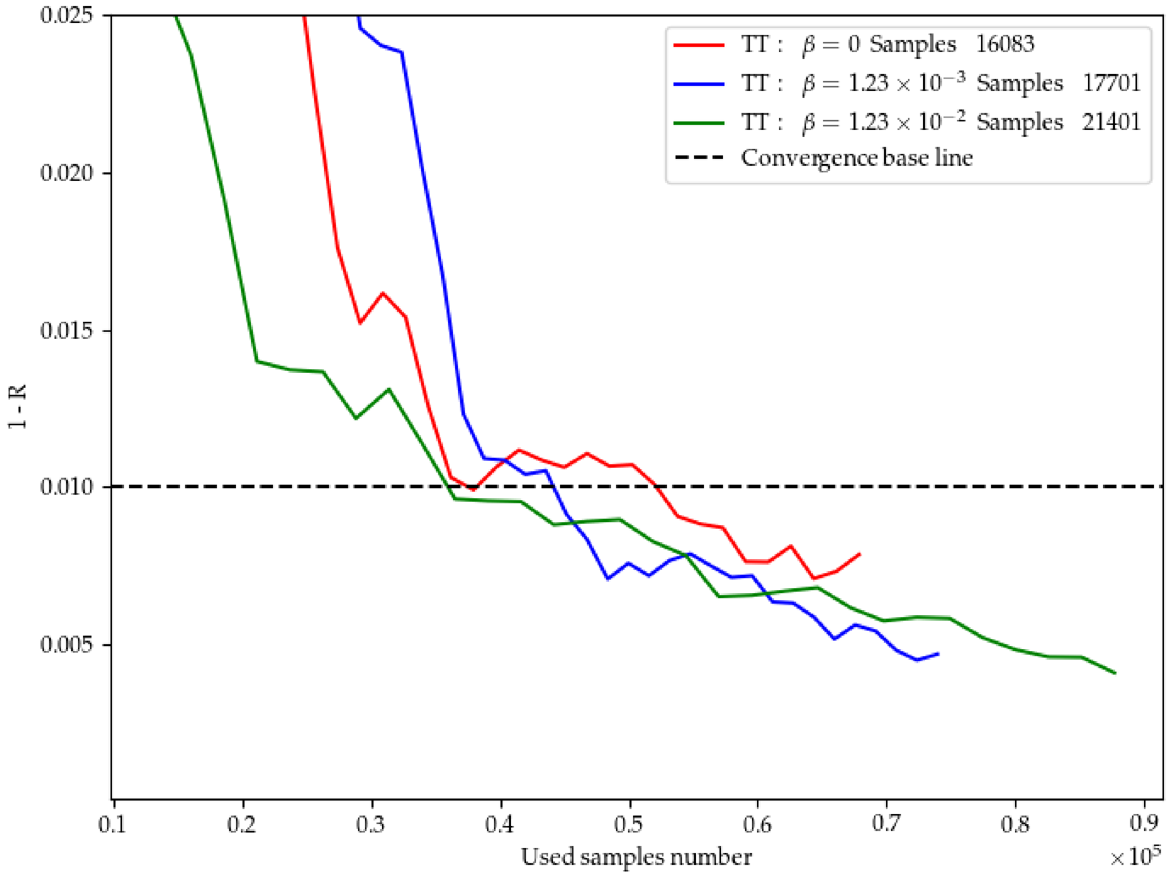

Figure C.7: Gelman-Rubin test for the temperature-only likelihood for cosmological parameters estimation as a function of the number of total samples in the chain for each considered boosting velocity $\boldsymbol{\beta} = (0, \boldsymbol{\beta}_{\rm dip}, 10 \times \boldsymbol{\beta}_{\rm dip})$.

C.3.3 Polarization: EE likelihood

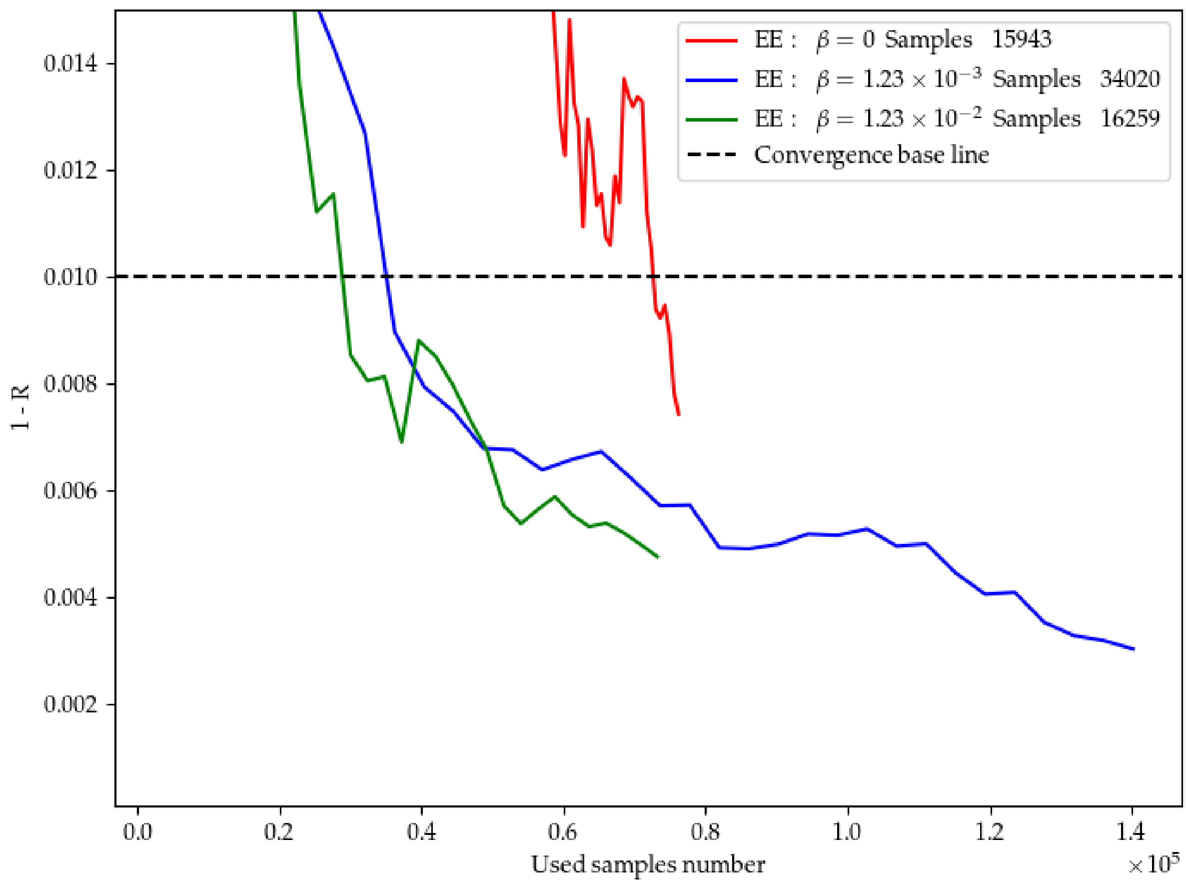

Figure C.8: Gelman-Rubin test for the polarization-only likelihood for cosmological parameters estimation as a function of the number of total samples in the chain for each considered boosting velocity $\boldsymbol{\beta} = (0, \boldsymbol{\beta}_{\rm dip}, 10 \times \boldsymbol{\beta}_{\rm dip})$.

C.3.4 Temperature-Polarization: TE likelihood

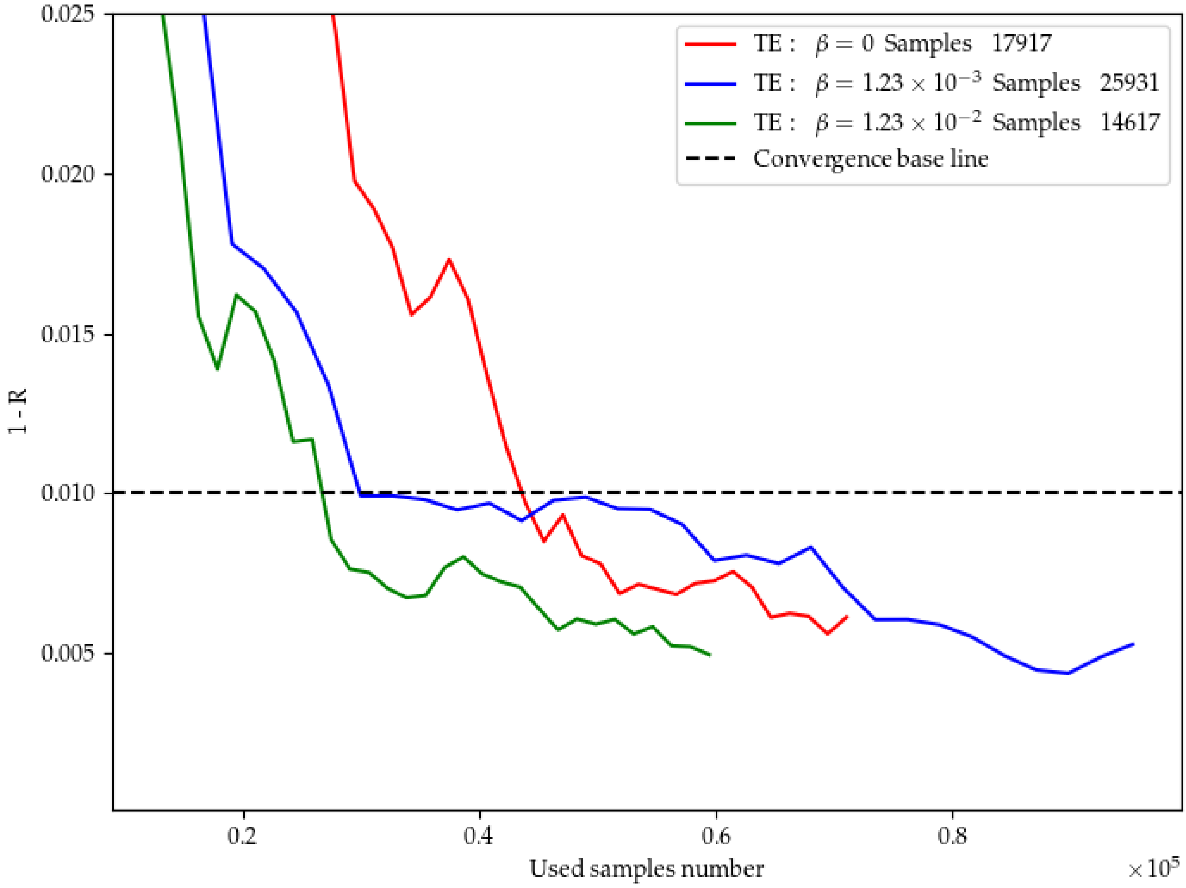

Figure C.9: Gelman-Rubin test for the temperature-polarization likelihood for cosmological parameters estimation as a function of the number of total samples in the chain for each considered boosting velocity $\boldsymbol{\beta} = (0, \boldsymbol{\beta}_{\rm dip}, 10 \times \boldsymbol{\beta}_{\rm dip})$.

C.3.5 Boosting likelihood estimation

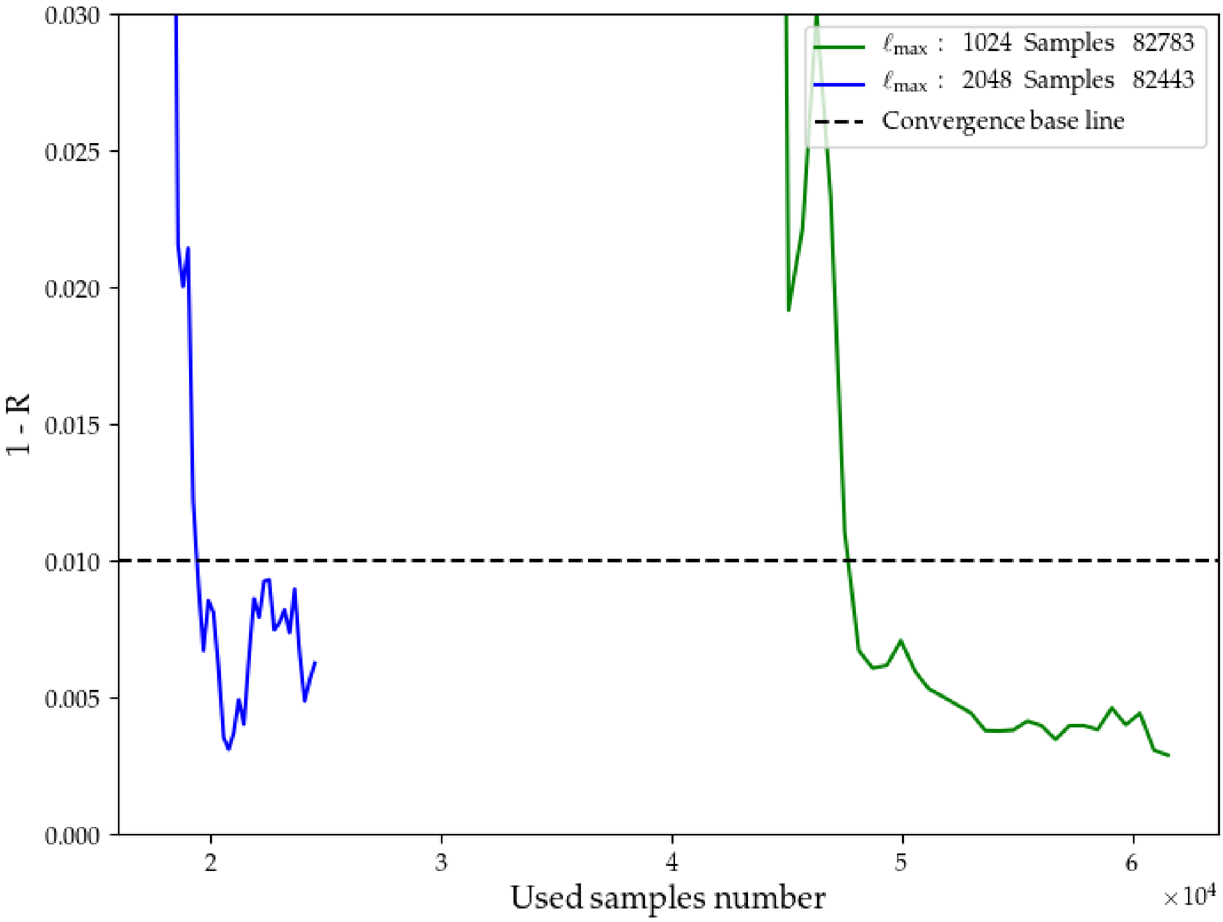

Figure C.10: Gelman-Rubin test for the Joint-Bayesian likelihood estimator showing convergence for chains with multipolar ranges of $2 \leq \ell \leq 1024$ (green) and $2 \leq \ell \leq 2048$ (blue).

D | Derivation of the cross-correlation function

The CMB measured temperature in the sky transforms under a general Lorentz transformation as:

$$T(\hat{\boldsymbol{n}}) = \frac{T'(\hat{\boldsymbol{n}}')}{\gamma(1-\boldsymbol{\beta}\cdot\hat{\boldsymbol{n}})}, \tag{D.1}$$

for $\beta << 1$ this expression can be Taylor expanded reducing into the following expression:

$$T(\hat{\boldsymbol{n}}) = T'(\hat{\boldsymbol{n}}')(1+\boldsymbol{\beta}\cdot\hat{\boldsymbol{n}}). \tag{D.2}$$

Since we are interested in the anisotropies, the monopolar contribution can be separated from the cosmological fluctuations in the temperature:

$$T'(\hat{\boldsymbol{n}}') - T_0 = \delta T'(\hat{\boldsymbol{n}}'), \tag{D.3}$$

where the vector $\hat{\boldsymbol{n}}'$ is a unit vector in the CMB rest frame, connected with the $\hat{\boldsymbol{n}}$, by a Lorentz transformation, and describing the aberration effect due to the relative motion of the solar system:

$$\hat{\boldsymbol{n}} = \frac{\hat{\boldsymbol{n}}' + [(\gamma-1)\hat{\boldsymbol{n}}'\cdot\boldsymbol{\beta}\boldsymbol{c} + \gamma|\boldsymbol{\beta}|]\hat{\boldsymbol{\beta}}}{\gamma(1+\hat{\boldsymbol{n}}'\cdot\boldsymbol{\beta})}, \tag{D.4}$$

where $\boldsymbol{c}$ is the speed of light. For $\beta << 1$, we can write:

$$\hat{\boldsymbol{n}}' = \hat{\boldsymbol{n}} + \boldsymbol{\nabla}\phi = \hat{\boldsymbol{n}} - \boldsymbol{\nabla}(\hat{\boldsymbol{n}}\cdot\boldsymbol{\beta}), \tag{D.5}$$

where ϕ is introduced as discussed in chapter 3 for the weak lensing approximation. By applying this equation inside (D.2) we can calculate the spherical harmonic coefficients for the same equation. The expression for such coefficients is given by:

$$a_{\ell m}^{\text{Total}} = \int d\hat{\boldsymbol{n}}\Big(T_0 + T_0(\boldsymbol{\beta}\cdot\hat{\boldsymbol{n}}) + \delta T'(\hat{\boldsymbol{n}}) + \delta T'(\hat{\boldsymbol{n}})(\hat{\boldsymbol{n}}\cdot\boldsymbol{\beta}) - \boldsymbol{\nabla}(\hat{\boldsymbol{n}}\cdot\boldsymbol{\beta})\cdot\boldsymbol{\nabla}\delta T'(\hat{\boldsymbol{n}})\Big)Y_\ell^{*m}(\hat{\boldsymbol{n}}). \tag{D.6}$$

The last expression can be separated into its different contributing parts:

$$a_{\ell m}^{\text{Monopole}} = \int d\hat{\boldsymbol{n}}\; T_0\; Y_\ell^{*m}(\hat{\boldsymbol{n}}), \tag{D.7}$$

$$a_{\ell m}^{\text{Dipole}} = \int d\hat{\boldsymbol{n}}\; T_0(\hat{\boldsymbol{n}}\cdot\boldsymbol{\beta})Y_\ell^{*m}(\hat{\boldsymbol{n}}), \tag{D.8}$$

$$a_{\ell m}^{\text{Doppler}} = \int d\hat{\boldsymbol{n}}\; \delta T'(\hat{\boldsymbol{n}})(\hat{\boldsymbol{n}}\cdot\boldsymbol{\beta})Y_\ell^{*m}(\hat{\boldsymbol{n}}), \tag{D.9}$$

$$a_{\ell m}^{\text{Aberration}} = -\int d\hat{\boldsymbol{n}}\; \boldsymbol{\nabla}(\hat{\boldsymbol{n}}\cdot\boldsymbol{\beta})\cdot\boldsymbol{\nabla}\delta T'(\hat{\boldsymbol{n}})Y_\ell^{*m}(\hat{\boldsymbol{n}}), \tag{D.10}$$

$$a_{\ell m}^{\text{Anisotropies}} = \int d\hat{\boldsymbol{n}}\, \delta T'(\hat{\boldsymbol{n}})\, Y_\ell^{*m}(\hat{\boldsymbol{n}}). \tag{D.11}$$

These coefficients will we be calculated separately. By starting with the aberration coefficient we take equation (D.10) by specifying $\delta T'(\hat{\boldsymbol{n}})$ (the anisotropies):

$$\delta T'(\hat{\boldsymbol{n}}) = \sum_{p=0}^{\infty} \sum_{q=-p}^{p} a_{pq}^{\text{Isotropic}} Y_p^q(\hat{\boldsymbol{n}}), \tag{D.12}$$

the equation for the aberration (D.10) is written in terms of the comoving CMB anisotropies with harmonic coefficients given by $a_{\ell m}$:

$$a_{\ell m}^{\text{Aberration}} = -\int d\hat{\boldsymbol{n}} \boldsymbol{\nabla}(\hat{\boldsymbol{n}} \cdot \boldsymbol{\beta}) \cdot \boldsymbol{\nabla}\Big[\sum_{p=0}^{\infty} \sum_{q=-p}^{p} a_{pq}^{\text{Isotropic}} Y_p^q(\hat{\boldsymbol{n}})\Big] Y_\ell^{*m}(\hat{\boldsymbol{n}}). \tag{D.13}$$

In addition, we need to specify a basis for the combination $\hat{\boldsymbol{n}} \cdot \boldsymbol{\beta}$, for a velocity applied in the $\hat{\boldsymbol{z}}$ direction, the most natural choice according within the weak lensing approximation is given by:

$$\hat{\boldsymbol{n}} \cdot \boldsymbol{\beta} = \beta \cos(\mu) = \beta\sqrt{\frac{4\pi}{3}} Y_1^0(\mu, \nu). \tag{D.14}$$

It is important to point out that for a general applied velocity effect in the CMB maps, it is possible to rotate the basis from where equation (D.14) is written [83]. By rotating the frame, the spherical harmonics are written in the new basis as follows:

$$Y_\ell^m(\mu, \nu) = \sum_{s=-\ell}^{\ell} D_{ms}^{*(\ell)} Y_\ell^s(\theta, \phi), \tag{D.15}$$

where the matrices $D_{ms}^{*(\ell)}$ are the Wigner D-matrices, which are functions of the Eulerian angles of the velocity vector, the matrices are defined as follows:

$$D_{ms}^{(\ell)}(\phi, \theta, \gamma) = e^{-im\gamma} d_{ms}^{(\ell)}(\theta) e^{-is\phi}, \tag{D.16}$$

where ϕ, θ and γ are the Euler angles, by using the new basis in equation (D.15), we can write the harmonic coefficients $a_{\ell m}^{\text{Aberration}}$ as a function of the velocity vector $\boldsymbol{\beta}$:

$$a_{\ell m}^{\text{Aberration}} = -\int d\hat{\boldsymbol{n}} \boldsymbol{\nabla}\Big(\beta\sqrt{\frac{4\pi}{3}} \sum_{s=-1}^{1} D_{0s}^{*(1)} Y_1^s(\hat{\boldsymbol{n}})\Big) \cdot \boldsymbol{\nabla}\Big[\sum_{p=0}^{\infty} \sum_{q=-p}^{p} a_{pq}^{\text{Isotropic}} Y_p^q\Big] Y_\ell^{*m}(\hat{\boldsymbol{n}}), \tag{D.17}$$

setting the basis in equation (D.15) the aberration spherical harmonic coefficient is given by:

$$
\begin{aligned}
a_{\ell m}^{\text{Aberration}} = -(-1)^m \beta \sqrt{\frac{4\pi}{3}} \sum_{s=-1}^{1} \sum_{p=0}^{\infty} \sum_{q=-p}^{p} D_{0s}^{*(1)} [2 + p(p+1) - \ell(\ell+1)] \; \times \\
\sqrt{\frac{3(2\ell+1)(2p+1)}{16\pi}} \begin{pmatrix} \ell & 1 & p \\ -m & s & q \end{pmatrix} \begin{pmatrix} \ell & 1 & p \\ 0 & 0 & 0 \end{pmatrix} a_{pq}^{\text{Isotropic}},
\end{aligned} \tag{D.18}
$$

where the following identity has been used [81]:

$$
\int d\hat{\boldsymbol{n}}\; Y_\ell^{*m}(\hat{\boldsymbol{n}})\; \boldsymbol{\nabla} Y_1^s(\hat{\boldsymbol{n}}) \cdot \boldsymbol{\nabla} Y_p^q(\hat{\boldsymbol{n}}) = (-1)^m \begin{pmatrix} \ell & 1 & p \\ -m & s & q \end{pmatrix} F^0_{\ell,1,p}, \tag{D.19}
$$

the function $F^0_{\ell,1,p}$, where its most general form is discussed in [81], has the form :

$$
F^{\pm s}_{\ell,L,p} = [L(L+1)+p(p+1)-\ell(\ell+1)] \sqrt{\frac{(2L+1)(2\ell+1)(2p+1)}{16\pi}} \begin{pmatrix} \ell & L & p \\ \pm s & 0 & \mp s \end{pmatrix}. \tag{D.20}
$$

On the other hand, Doppler modulation effect in equation (D.9), by using the same conventions for the aberration, can be written as follows:

$$
a_{\ell m}^{\text{Doppler}} = \int d\hat{\boldsymbol{n}} \Big[\delta T'(\hat{\boldsymbol{n}}) \beta \sqrt{\frac{4\pi}{3}} \sum_{s=-1}^{1} D_{0s}^{*(1)} Y_1^s(\hat{\boldsymbol{n}}) \Big] Y_\ell^{*m}(\hat{\boldsymbol{n}}), \tag{D.21}
$$

reducing into:

$$
\begin{aligned}
a_{\ell m}^{\text{Doppler}} =& \beta \sqrt{\frac{4\pi}{3}} \sum_{s=-1}^{1} \sum_{p=0}^{\infty} \sum_{q=-p}^{p} a_{pq}^{\text{Isotropic}} D_{0s}^{*(1)} (-1)^m \; \times \\
& \sqrt{\frac{3(2p+1)(2\ell+1)}{4\pi}} \begin{pmatrix} p & 1 & \ell \\ 0 & 0 & 0 \end{pmatrix} \begin{pmatrix} p & 1 & \ell \\ q & s & -m \end{pmatrix},
\end{aligned} \tag{D.22}
$$

by using the Gaunt integral with the phase conventions described in [83,84]:

$$
\begin{aligned}
\int d\hat{\boldsymbol{n}} Y_p^q(\hat{\boldsymbol{n}}) Y_1^s(\hat{\boldsymbol{n}}) Y_\ell^{*m}(\hat{\boldsymbol{n}}) =& (-1)^m \sqrt{\frac{3(2p+1)(2\ell+1)}{4\pi}} \; \times \\
& \begin{pmatrix} p & 1 & \ell \\ 0 & 0 & 0 \end{pmatrix} \begin{pmatrix} p & 1 & \ell \\ q & s & -m \end{pmatrix}.
\end{aligned} \tag{D.23}
$$

By collecting terms in equations (D.7) - (D.11), we have the expressions for the relativistic modified spherical harmonics coefficients:

$$
\begin{aligned}
a_{\ell m}^{\text{Aberration}} = -(-1)^m \beta \sqrt{\frac{4\pi}{3}} \sum_{s=-1}^{1} \sum_{p=0}^{\infty} \sum_{q=-p}^{p} D_{0s}^{*(1)} [2 + p(p+1) - \ell(\ell+1)] \; \times \\
\sqrt{\frac{3(2\ell+1)(2p+1)}{16\pi}} \begin{pmatrix} \ell & 1 & p \\ -m & s & q \end{pmatrix} \begin{pmatrix} \ell & 1 & p \\ 0 & 0 & 0 \end{pmatrix} a_{pq}^{\text{Isotropic}},
\end{aligned} \tag{D.24}
$$

$$\begin{aligned} a_{\ell m}^{\text{Doppler}} =&\beta\sqrt{\frac{4\pi}{3}}\sum_{s=-1}^{1}\sum_{p=0}^{\infty}\sum_{q=-p}^{p} D_{0s}^{*(1)}(-1)^m\sqrt{\frac{3(2p+1)(2\ell+1)}{4\pi}} \\ &\begin{pmatrix} p & 1 & \ell \\ 0 & 0 & 0 \end{pmatrix}\begin{pmatrix} p & 1 & \ell \\ q & s & -m \end{pmatrix} a_{pq}^{\text{Isotropic}}, \end{aligned} \tag{D.25}$$

$$a_{1s}^{\text{Dipole}} = T_0\beta\sqrt{\frac{4\pi}{3}}\sum_{s=-1}^{1} D_{0s}^{*(1)}, \tag{D.26}$$

by evaluating the 3j symbols in equations (D.24), (D.25) following the convention in [13] and introducing the short-hand notation:

$$H(\ell,m) = \sqrt{\frac{(\ell-m)(\ell+m)}{4\ell^2-1}}, \tag{D.27}$$

$$J(\ell,m) = \sqrt{\frac{(\ell-m-1)(\ell-m)}{8\ell^2-2}}, \tag{D.28}$$

$$K(\ell,m) = \sqrt{\frac{(\ell+m+1)(\ell+m+2)}{8\ell(\ell+2)+6}}. \tag{D.29}$$

Notice that the calculated coefficients $a_{\ell m}$ for Doppler modulation and aberration will reduce into:

$$\begin{aligned} a_{\ell m}^{\text{Aberration}} = \beta\Bigg[&\frac{\sin(\theta)}{\sqrt{2}}e^{-i\phi}(\ell-1)J(\ell,m)a_{\ell-1m+1}^{\text{Isotropic}} + \cos(\theta)(\ell-1)H(\ell,m)a_{\ell-1m}^{\text{Isotropic}} \\ &-\frac{\sin(\theta)}{\sqrt{2}}e^{i\phi}(\ell-1)J(\ell,-m)a_{\ell-1m-1}^{\text{Isotropic}} + \frac{\sin(\theta)}{\sqrt{2}}e^{-i\phi}(\ell+2)K(\ell,m)a_{\ell+1m+1}^{\text{Isotropic}} \\ &-\cos(\theta)(\ell+2)H(\ell+1,m)a_{\ell+1m}^{\text{Isotropic}} - \frac{\sin(\theta)}{\sqrt{2}}e^{i\phi}(\ell+2)K(\ell,-m)a_{\ell+1m-1}^{\text{Isotropic}}\Bigg], \end{aligned} \tag{D.30}$$

$$\begin{aligned} a_{\ell m}^{\text{Doppler}} = \beta\Bigg[&\frac{\sin(\theta)}{\sqrt{2}}e^{-i\phi}J(\ell,m)a_{\ell-1m+1}^{\text{Isotropic}} + \cos(\theta)H(\ell,m)a_{\ell-1m}^{\text{Isotropic}} \\ &-\frac{\sin(\theta)}{\sqrt{2}}e^{i\phi}J(\ell,-m)a_{\ell-1m-1}^{\text{Isotropic}} - \frac{\sin(\theta)}{\sqrt{2}}e^{-i\phi}K(\ell,m)a_{\ell+1m+1}^{\text{Isotropic}} \\ &+\cos(\theta)H(\ell+1,m)a_{\ell+1m}^{\text{Isotropic}} + \frac{\sin(\theta)}{\sqrt{2}}e^{i\phi}K(\ell,-m)a_{\ell+1m-1}^{\text{Isotropic}}\Bigg], \end{aligned} \tag{D.31}$$

$$a_{1s}^{\text{Dipole}} = T_0\beta\sqrt{\frac{4\pi}{3}}\left(\frac{\sin(\theta)}{\sqrt{2}}e^{-i\phi} + \cos(\theta) - \frac{\sin(\theta)}{\sqrt{2}}e^{i\phi}\right), \tag{D.32}$$

by using these expressions we calculate the non-vanishing contributions to the $\langle a^{*total}_{\ell m} a^{total}_{\ell+1 m}\rangle$ correlator:

$$\langle a^{*\text{Total}}_{\ell m} a^{\text{Total}}_{\ell+1 m}\rangle = \beta\Big[a^{*\text{Isotropic}}_{\ell m}\Big((\ell+1)d^{\text{Total}}_{\ell m+1} + (\ell+1)e^{\text{Total}}_{\ell m} + (\ell+1)f^{\text{Total}}_{\ell m-1}\Big)$$
$$+a^{\text{Isotropic}}_{\ell+1 m}\Big((-(\ell+2)+1)g^{*\text{Total}}_{\ell+1 m+1} + (-(\ell+2)+1)h^{*\text{Total}}_{\ell+1 m} + (-(\ell+2)+1)i^{*\text{Total}}_{\ell+1 m-1}\Big)\Big], \tag{D.33}$$

with the set of coefficients d, e, f, g, h and i defined as follows:

$$\begin{aligned}
d^{\text{Total}}_{\ell-1 m+1} &= \frac{\sin(\theta)}{\sqrt{2}}e^{-i\phi}J(\ell,m)a^{\text{Isotropic}}_{\ell-1 m+1}, \quad e^{\text{Total}}_{\ell-1 m} = \cos(\theta)H(\ell,m)a^{\text{Isotropic}}_{\ell-1 m},\\
f^{\text{Total}}_{\ell-1 m-1} &= -\frac{\sin(\theta)}{\sqrt{2}}e^{i\phi}J(\ell,-m)a^{\text{Isotropic}}_{\ell-1 m-1}, \quad g^{\text{Total}}_{\ell+1 m+1} = -\frac{\sin(\theta)}{\sqrt{2}}e^{-i\phi}K(\ell,m)a^{\text{Isotropic}}_{\ell+1 m+1}\\
h^{\text{Total}}_{\ell+1 m} &= \cos(\theta)H(\ell+1,m)a^{\text{Isotropic}}_{\ell+1 m}, \quad i^{\text{Total}}_{\ell+1 m-1} = \frac{\sin(\theta)}{\sqrt{2}}e^{i\phi}K(\ell,-m)a^{\text{Isotropic}}_{\ell+1 m-1}.
\end{aligned} \tag{D.34}$$

By requiring statistical isotropy in the comoving basis (i.e. the cross-correlation function for the CMB anisotropies is diagonal $\langle a^{*\text{Isotropic}}_{\ell m} a^{\text{Isotropic}}_{\ell' m'}\rangle = \delta_{m\, m'}\delta_{\ell\ell'}C^{TT}_{\ell}$), we have:

$$\begin{aligned}
\langle a^{*\text{Total}}_{\ell m} a^{\text{Total}}_{\ell+1 m}\rangle = \langle\beta\Big[&a^{*\text{Isotropic}}_{\ell m}\Big((\ell+1)(\cos(\theta)H(\ell+1,m)a^{\text{Isotropic}}_{\ell m})\Big)\\
&+a^{\text{Isotropic}}_{\ell+1 m}\Big((-(\ell+2)+1)(\cos(\theta)H(\ell+1,m)a^{\text{Isotropic}}_{\ell+1 m})\Big)\Big]\rangle,
\end{aligned} \tag{D.35}$$

and the cross-correlation function used in chapter 3 is recovered:

$$\begin{aligned}
\langle a^{*\text{Total}}_{\ell m} a^{\text{Total}}_{\ell+1 m}\rangle = \cos(\theta)\beta\Big[&(\ell+1)H(\ell+1,m)C^{TT}_{\ell}\\
&+(1-(\ell+2))H(\ell+1,m)C^{TT}_{\ell+1}\Big],
\end{aligned} \tag{D.36}$$

where θ is the azimuth angle, taking as a special case an applied boost in $\hat{z}$ direction we recover:

$$\begin{aligned}
\langle a^{*\text{Total}}_{\ell m} a^{\text{Total}}_{\ell+1 m}\rangle = \beta_z\Bigg[&\underbrace{\ell H(\ell+1,m)C^{TT}_{\ell} - (\ell+2)H(\ell+1,m)C^{TT}_{\ell+1}}_{\text{Relativistic aberration}}\\
&+\underbrace{\Big(H(\ell+1,m)C^{TT}_{\ell} + H(\ell+1,m)C^{TT}_{\ell+1}\Big)}_{\text{Doppler modulation}}\Bigg].
\end{aligned} \tag{D.37}$$

E | Noise impact over the boost likelihood

In this appendix we show the equivalence between the noiseless auto-correlation and the noisy cross-correlation modes for the MCMC presented in chapter 5. However, the likelihood employed for determine $\boldsymbol{\beta}$ allows to take into account the impact of noise in CMB maps. As example, figure (E.1) shows the impact in the temperature power spectrum by including isotropic noise with a RMS of 64 μK pixel^{-1}.

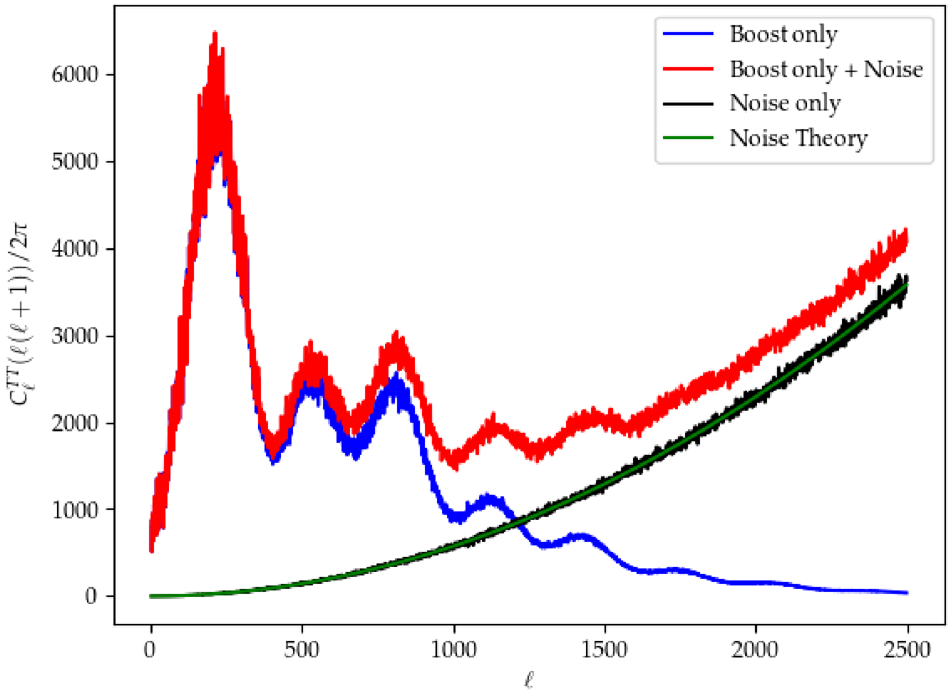

Figure E.1: Impact of noise in the temeperature power spectrum of the CMB. Boosted CMB temperature power spectrum before including a random gaussian noise (blue), after including the noise noise with a RMS of 64 μK pixel^{-1} (red), theoretical power for the introduced noise (green) and extracted spectrum for a noise-only map template (black).

In chapter 5, the posteriors have been estimated using as input for the likelihood noiseless pixelized maps. In real data, these maps contain a certain amount of noise, usually not even uniform across the sky. It is common, however, to overcome the problem of modeling the noise contained in the input maps by working on cross-correlation mode between maps measured at different frequencies and, therefore, containing independent noise realizations. In that situation, the average cross-correlation noise is zero and, in practice, results obtained in noiseless auto-correlation mode should be equivalent to those obtained in noisy cross-correlation mode. Figure (E.1) proves this point by showing the behavior of the likelihood around its maximum in the harmonic parameter space $\{\beta_{1N}\}$. The widths of the curves associated to these two modes are consistent. A third case is shown to better understand the effect of noise, the one labeled as "64 μK auto-correlation mode". The effect of the noise is, of course, increase the width of the likelihood, that is, degrade the resolution in β_{1N}.

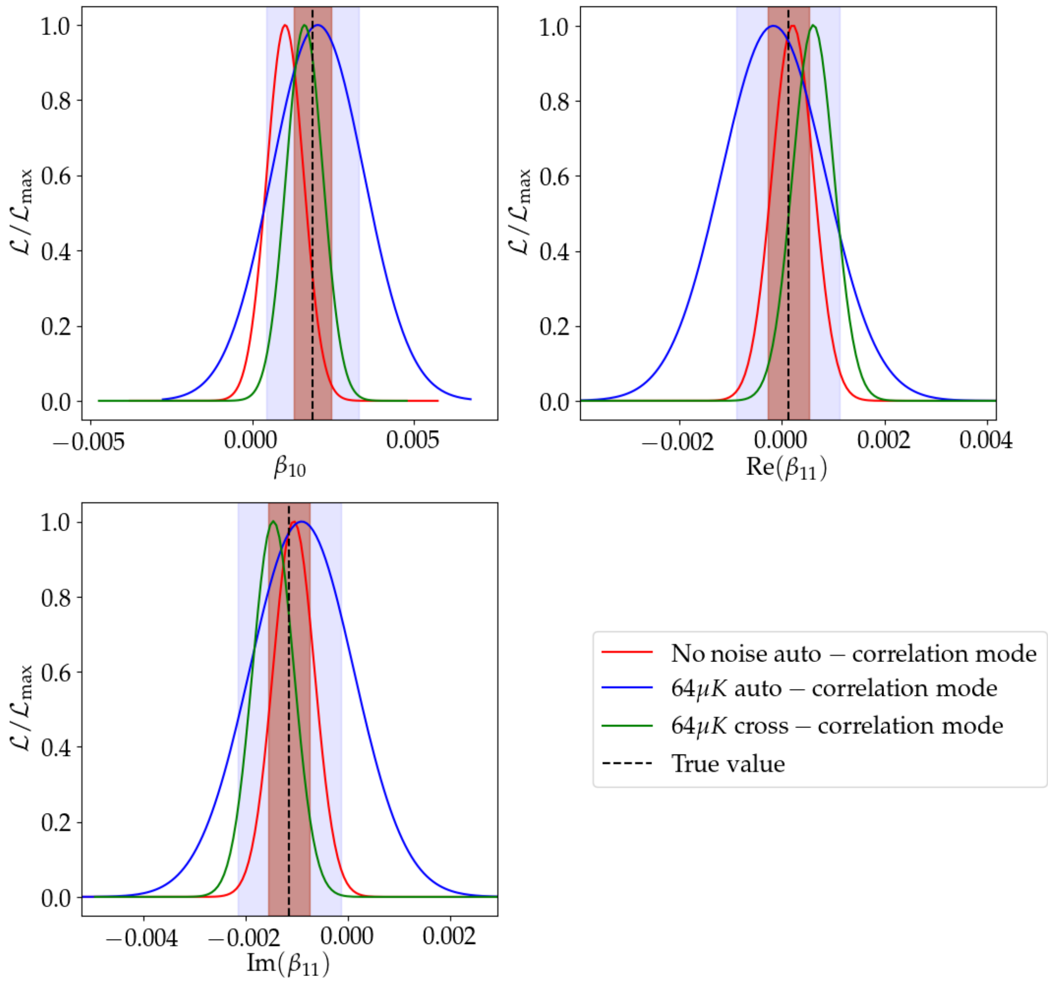

Figure E.2: Normalized likelihood slices for three different modes of correlating CMB maps in the Metropolis-Hastings algorithm used in chapter 5. No noise applied (Red), by applying $64\mu K$ per pixel in the MCMC with auto-correlation mode (blue), and the same slices by using the cross-correlation mode (Green) against the true fiducial value used in simulations (dashed lines). Notice that all the likelihood slices peaks within 1σ region in β_{1N} parameters.

F | Harmonic to real space transformation rules

Following [15], the dipolar direction of the boosting velocity $\boldsymbol{\beta}$ can be expressed in terms of the harmonic components of β_{1N}:

$$\boldsymbol{\beta} \cdot \hat{\boldsymbol{n}} = \sum_{N=-1}^{1} \beta_{1N} Y_N^1(\hat{\boldsymbol{n}}), \tag{F.1}$$

where the $\hat{\boldsymbol{n}}$ is the line of sight direction of the observer, and $\boldsymbol{\beta}$ is the boosting vector velocity connecting observer reference frame and CMB frame.

$$\beta = \sqrt{\frac{3}{4\pi}} \sqrt{\beta_{10}^2 + 2\mathrm{Re}(\beta_{11}^2) + 2\mathrm{Im}(\beta_{11})^2}, \tag{F.2}$$

$$b = \frac{\pi}{2} - \cos^{-1}\left[\frac{\beta_{10}}{\beta}\sqrt{\frac{3}{4\pi}}\right], \tag{F.3}$$

$$l = -\tan^{-1}\left[\frac{\mathrm{Im}(\beta_{11})}{\mathrm{Re}(\beta_{11})}\right], \tag{F.4}$$

where β, l and b are the module of the boosting velocity vector $\boldsymbol{\beta}$, b is the colatitude, and l is the longitude in galactic coordinates. where the relation $\beta^*_{1-1} = \beta_{11}$ has been used.

Bibliography

[1] A. A. Penzias and R. W. Wilson, *A Measurement of excess antenna temperature at 4080-Mc/s*, *Astrophys. J.* **142** (1965) 419.

[2] P. J. E. Peebles, D. N. Schramm, E. L. Turner and R. G. Kron, *The Case for the hot big bang cosmology*, *Nature* **352** (1991) 769.

[3] J. A. Peacock, S. Cole, P. Norberg, C. M. Baugh, J. Bland-Hawthorn, T. Bridges et al., *A measurement of the cosmological mass density from clustering in the 2df galaxy redshift survey*, *Nature* **410** (2001) 169–173.

[4] S. Dodelson, *Modern cosmology*. Academic Press, San Diego, CA, 2003.

[5] D. J. Fixsen, *The temperature of the cosmic microwave background*, *The Astrophysical Journal* **707** (2009) 916–920.

[6] W. T. Hu, *Wandering in the Background: A CMB Explorer*, other thesis, 8, 1995.

[7] PLANCK collaboration, *Planck 2015 results. XIII. Cosmological parameters*, *Astron. Astrophys.* **594** (2016) A13 [1502.01589].

[8] G. F. Smoot et al., *First results of the COBE satellite measurement of the anisotropy of the cosmic microwave background radiation*, in *2nd Rencontre de Blois on Physical Cosmology: 25th Anniversary of the Cosmic Background Radiation Discovery*, pp. 105–120, 5, 1991.

[9] C. H. Lineweaver, L. Tenorio, G. F. Smoot, P. Keegstra, A. J. Banday and P. Lubin, *The dipole observed in the COBE DMR four-year data*, *Astrophys. J.* **470** (1996) 38 [astro-ph/9601151].

[10] PLANCK collaboration, *The Scientific programme of Planck*, astro-ph/0604069.

[11] PLANCK collaboration, *Planck 2013 results. XXVII. Doppler boosting of the CMB: Eppur si muove*, *Astron. Astrophys.* **571** (2014) A27 [1303.5087].

[12] PLANCK collaboration, *Planck 2015 results. XVI. Isotropy and statistics of the CMB*, *Astron. Astrophys.* **594** (2016) A16 [1506.07135].

[13] L. Amendola, R. Catena, I. Masina, A. Notari, M. Quartin and C. Quercellini, *Measuring our peculiar velocity on the CMB with high-multipole off-diagonal correlations*, *JCAP* **07** (2011) 027 [1008.1183].

[14] A. Challinor and F. van Leeuwen, *Peculiar velocity effects in high resolution microwave background experiments*, *Phys. Rev.* **D65** (2002) 103001 [astro-ph/0112457].

[15] S. Shaikh, S. Mukherjee, S. Das, B. D. Wandelt and T. Souradeep, *Joint Bayesian Analysis of Large Angular Scale CMB Temperature Anomalies*, *JCAP* **08** (2019) 007 [1902.10155].

[16] S. M. Carroll, *Lecture notes on general relativity*, gr-qc/9712019.

[17] J. McDonald, *Baryon-to-Dark Matter Ratio from Random Angular Fields*, *JCAP* **01** (2013) 025 [1211.4472].

[18] S. W. Allen, A. E. Evrard and A. B. Mantz, *Cosmological parameters from observations of galaxy clusters*, *Annual Review of Astronomy and Astrophysics* **49** (2011) 409–470.

[19] S. Faber and R. Jackson, *Velocity dispersions and mass to light ratios for elliptical galaxies*, *Astrophys. J.* **204** (1976) 668.

[20] W. J. Percival et al., *The shape of the SDSS DR5 galaxy power spectrum*, *Astrophys. J.* **657** (2007) 645 [astro-ph/0608636].

[21] D. Clowe, A. Gonzalez and M. Markevitch, *Weak lensing mass reconstruction of the interacting cluster 1E0657-558: Direct evidence for the existence of dark matter*, *Astrophys. J.* **604** (2004) 596 [astro-ph/0312273].

[22] X.-P. Wu, T. Chiueh, L.-Z. Fang and Y.-J. Xue, *A comparison of different cluster mass estimates: consistency or discrepancy?*, *Monthly Notices of the Royal Astronomical Society* **301** (1998) 861–871.

[23] G. Hinshaw, J. L. Weiland, R. S. Hill, N. Odegard, D. Larson, C. L. Bennett et al., *Five-year wilkinson microwave anisotropy probe observations: Data processing, sky maps, and basic results*, *The Astrophysical Journal Supplement Series* **180** (2009) 225.

[24] P. A. R. Ade, N. Aghanim, M. Arnaud, M. Ashdown, J. Aumont, C. Baccigalupi et al., *Planck2015 results*, *Astronomy & Astrophysics* **594** (2016) A13.

[25] Supernova Cosmology Project collaboration, *Measurements of Ω and Λ from 42 high redshift supernovae*, *Astrophys. J.* **517** (1999) 565 [astro-ph/9812133].

[26] Particle Data Group collaboration, *Review of Particle Physics*, *Phys. Rev.* **D98** (2018) 030001.

[27] D. Baumann, *Lecture notes in Cosmology: Part III Mathematical Tripos*, November, 2014.

[28] V. Mukhanov, *Physical Foundations of Cosmology*. Cambridge Univ. Press, Cambridge, 2005, 10.1017/CBO9780511790553.

[29] R. Durrer, *The Cosmic Microwave Background*. Cambridge University Press, Cambridge, 2008, 10.1017/CBO9780511817205.

[30] G. Smoot, C. Bennett, A. Kogut, J. Aymon, C. Backus, G. de Amici et al., *First results of the cobe satellite measurement of the anisotropy of the cosmic microwave background radiation*, *Advances in Space Research* **11** (1991) 193.

[31] A. Kogut et al., *Dipole anisotropy in the COBE DMR first year sky maps*, *Astrophys. J.* **419** (1993) 1 [astro-ph/9312056].

[32] D. Larson et al., *Seven-Year Wilkinson Microwave Anisotropy Probe (WMAP) Observations: Power Spectra and WMAP-Derived Parameters*, *Astrophys. J. Suppl.* **192** (2011) 16 [1001.4635].

[33] PLANCK collaboration, *Planck 2015 results. XI. CMB power spectra, likelihoods, and robustness of parameters*, *Astron. Astrophys.* **594** (2016) A11 [1507.02704].

[34] PLANCK collaboration, *Planck 2015 results. XI. CMB power spectra, likelihoods, and robustness of parameters*, *Astron. Astrophys.* **594** (2016) A11 [1507.02704].

[35] SDSS collaboration, *Detection of the Baryon Acoustic Peak in the Large-Scale Correlation Function of SDSS Luminous Red Galaxies*, *Astrophys. J.* **633** (2005) 560 [astro-ph/0501171].

[36] DES collaboration, *First Cosmology Results using Type Ia Supernovae from the Dark Energy Survey: Constraints on Cosmological Parameters*, *Astrophys. J. Lett.* **872** (2019) L30 [1811.02374].

[37] D. Blas, J. Lesgourgues and T. Tram, *The Cosmic Linear Anisotropy Solving System (CLASS) II: Approximation schemes*, *JCAP* **07** (2011) 034 [1104.2933].

[38] A. Lewis, A. Challinor and A. Lasenby, *Efficient computation of CMB anisotropies in closed FRW models*, *apj* **538** (2000) 473 [astro-ph/9911177].

[39] D. Baumann, *Lecture notes in Advanced Cosmology*, November, 2014.

[40] J. Kovac, E. Leitch, C. Pryke, J. Carlstrom, N. Halverson and W. Holzapfel, *Detection of polarization in the cosmic microwave background using DASI*, *Nature* **420** (2002) 772 [astro-ph/0209478].

[41] C. W. O'Dell, B. G. Keating, A. de Oliveira-Costa, M. Tegmark and P. T. Timbie, *CMB polarization at large angular scales: Data analysis of the POLAR experiment*, *Phys. Rev. D* **68** (2003) 042002 [astro-ph/0212425].

[42] A. Kogut, *Wmap polarization results*, *New Astron. Rev.* **47** (2003) 977 [astro-ph/0306048].

[43] M. Zaldarriaga and U. Seljak, *An all sky analysis of polarization in the microwave background*, *Phys. Rev.* **D55** (1997) 1830 [astro-ph/9609170].

[44] M. Britton, *Radio astronomical polarimetry and the Lorentz group*, *Astrophys. J.* **532** (2000) 1240 [astro-ph/9911101].

[45] W. Hu, *CMB temperature and polarization anisotropy fundamentals*, *Annals Phys.* **303** (2003) 203 [astro-ph/0210696].

[46] T. Dray, *The relationship between monopole harmonics and spin-weighted spherical harmonics*, *Journal of Mathematical Physics* **26** (1985) 1030 [https://doi.org/10.1063/1.526533].

[47] J. Kapteyn, *First Attempt at a Theory of the Arrangement and Motion of the Sidereal System*, *Astrophys. J.* **55** (1922) 302.

[48] F. D. Kahn and L. Woltjer, *Intergalactic Matter and the Galaxy.*, *apj* **130** (1959) 705.

[49] D. Lynden-Bell, S. M. Faber, D. Burstein, R. L. Davies, A. Dressler, R. J. Terlevich et al., *Spectroscopy and photometry of elliptical galaxies. V - Galaxy streaming toward the new supergalactic center*, *Astrophys. J.* **326** (1988) 19.

[50] R. Mohayaee, M. Rameez and S. Sarkar, *The impact of peculiar velocities on supernova cosmology*, 2003.10420.

[51] N. W. Boggess et al., *The COBE mission - Its design and performance two years after launch*, *Astrophys. J.* **397** (1992) 420.

[52] PLANCK collaboration, *Planck 2015 results VII. High Frequency Instrument data processing: Time-ordered information and beams*, *Astron. Astrophys.* **594** (2016) A7 [1502.01586].

[53] PLANCK collaboration, *Planck 2015 results. VIII. High Frequency Instrument data processing: Calibration and maps*, *Astron. Astrophys.* **594** (2016) A8 [1502.01587].

[54] W. M. Folkner, P. Charlot, M. H. Finger, J. G. Williams, O. J. Sovers, X. Newhall et al., *Determination of the extragalactic-planetary frame tie from joint analysis of radio interferometric and lunar laser ranging measurements.*, *Astronomy and Astrophysics* **287** (1994) 279.

[55] P. d. S. Ferreira and M. Quartin, *First constraints on the intrinsic CMB dipole and our velocity with Doppler and aberration*, 2011.08385.

[56] M. Quartin and A. Notari, *Improving Planck calibration by including frequency-dependent relativistic corrections*, *JCAP* **09** (2015) 050 [1504.04897].

[57] PLANCK collaboration, *Planck 2013 results. XVII. Gravitational lensing by large-scale structure*, *Astron. Astrophys.* **571** (2014) A17 [1303.5077].

[58] S. Yasini and E. Pierpaoli, *Footprints of Doppler and aberration effects in cosmic microwave background experiments: statistical and cosmological implications*, *Mon. Not. Roy. Astron. Soc.* **493** (2020) 1708 [1910.04315].

[59] W. Hu, *Weak lensing of the CMB: A harmonic approach*, Phys. Rev. D **62** (2000) 043007 [astro-ph/0001303].

[60] D. Jeong, J. Chluba, L. Dai, M. Kamionkowski and X. Wang, *The effect of aberration on partial-sky measurements of the cosmic microwave background temperature power spectrum*, Phys. Rev. D **89** (2014) 023003 [1309.2285].

[61] B. Walsh, *Markov chain monte carlo and gibbs sampling*, *Lecture Notes for EEB 581, version 26, April* (2004) .

[62] N. V. Kampen, *Stochastic processes in physics and chemistry*. North Holland, 2007.

[63] A. Tolver, *An introduction to markov chains*, February, 2016.

[64] N. Metropolis, A. Rosenbluth, M. Rosenbluth, A. Teller and E. Teller, *Equation of state calculations by fast computing machines*, J. Chem. Phys. **21** (1953) 1087.

[65] W. Hastings, *Monte Carlo Sampling Methods Using Markov Chains and Their Applications*, Biometrika **57** (1970) 97.

[66] A. Lewis, *Efficient sampling of fast and slow cosmological parameters*, *prd* **87** (2013) 103529 [1304.4473].

[67] Planck collaboration, *Planck 2018 results. V. CMB power spectra and likelihoods*, Astron. Astrophys. **641** (2020) A5 [1907.12875].

[68] Planck collaboration, *Planck 2015 results. X. Diffuse component separation: Foreground maps*, Astron. Astrophys. **594** (2016) A10 [1502.01588].

[69] Planck collaboration, *Planck 2015 results. I. Overview of products and scientific results*, Astron. Astrophys. **594** (2016) A1 [1502.01582].

[70] Planck collaboration, *Planck 2018 results. VI. Cosmological parameters*, Astron. Astrophys. **641** (2020) A6 [1807.06209].

[71] F. Beutler, C. Blake, M. Colless, D. H. Jones, L. Staveley-Smith, L. Campbell et al., *The 6df galaxy survey: baryon acoustic oscillations and the local hubble constant*, Monthly Notices of the Royal Astronomical Society **416** (2011) 3017–3032.

[72] A. J. Ross, L. Samushia, C. Howlett, W. J. Percival, A. Burden and M. Manera, *The clustering of the sdss dr7 main galaxy sample – i. a 4 per cent distance measure at* $z = 0.15$, Monthly Notices of the Royal Astronomical Society **449** (2015) 835–847.

[73] A. Lewis, *GetDist: a Python package for analysing Monte Carlo samples*, 1910.13970.

[74] A. Gelman and D. B. Rubin, *Inference from Iterative Simulation Using Multiple Sequences*, Statist. Sci. **7** (1992) 457.

[75] DES collaboration, *Dark Energy Survey Year 1 Results: Cosmological Constraints from Cluster Abundances, Weak Lensing, and Galaxy Correlations*, 2010.01138.

[76] PLANCK collaboration, *Planck intermediate results. LVI. Detection of the CMB dipole through modulation of the thermal Sunyaev-Zeldovich effect: Eppur si muove II*, 2003.12646.

[77] S. Duane, A. Kennedy, B. Pendleton and D. Roweth, *Hybrid Monte Carlo*, *Phys. Lett. B* **195** (1987) 216.

[78] A. Hajian, *Efficient Cosmological Parameter Estimation with Hamiltonian Monte Carlo*, *Phys. Rev. D* **75** (2007) 083525 [astro-ph/0608679].

[79] S. Das, B. D. Wandelt and T. Souradeep, *Bayesian inference on the sphere beyond statistical isotropy*, *JCAP* **10** (2015) 050 [1509.07137].

[80] P. K. Aluri, N. Pant, A. Rotti and T. Souradeep, *Novel approach to reconstructing signals of isotropy violation from a masked CMB sky*, *Phys. Rev. D* **92** (2015) 083015 [1506.00550].

[81] T. Okamoto and W. Hu, *CMB lensing reconstruction on the full sky*, *Phys. Rev.* **D67** (2003) 083002 [astro-ph/0301031].

[82] A. Lewis and S. Bridle, *Cosmological parameters from CMB and other data: A Monte Carlo approach*, *prd* **66** (2002) 103511 [astro-ph/0205436].

[83] A. Edmonds, *Angular Momentum in Quantum Mechanics*, Investigations in Physics Series. Princeton University Press, 1996.

[84] D. A. Varshalovich, A. N. Moskalev and V. K. Khersonskii, *Quantum Theory of Angular Momentum*. World Scientific, Singapore, 1988.